LIGHTNING RETURN-STROKE CURRENT WAVEFORMS ALOFT, FROM MEASURED FIELD CHANGE, CURRENT, AND CHANNEL GEOMETRY

J.C. Willett
P.O. Box 41, Garrett Park, MD 20896

D.M. Le Vine
Code 614.6, NASA/GSFC, Greenbelt, MD 20771

V.P. Idone
Dept. of Earth and Atmospheric Sciences, Univ. at Albany, SUNY, 1400 Washington Ave., Albany, NY 12222

Submitted to *Journal of Geophysical Research, Atmospheres*
October 5, 2006

Abstract

Three-dimensional reconstructions of six rocket-triggered lightning channels are derived from stereo photographs. These reconstructed channels are used to infer the behavior of the current in return strokes above the ground from current waveforms measured at the channel base and electric-field-change waveforms measured at a range of 5.2 km for 24 return strokes in these channels. Streak photographs of 14 of the same strokes are analyzed to determine the rise times, propagation speeds, and amplitudes of relative light intensity for comparison with the electrical inferences. Results include the following: 1) The fine structure of the field-change waveforms that were radiated by these subsequent return strokes can be explained, in large part, by channel geometry. 2) The average 10 - 90% rise time of the stroke current increased by about a factor of seven in our sample, from an observed 0.31 ± 0.17 μs at the surface to an inferred 2.2 ± 0.5 μs at 1 km path length above the surface. 3) The three-dimensional propagation speed of the current front averaged $1.80 \pm 0.24 \times 10^8$ m/s over channel lengths typically greater than 1 km. 4) Assuming that the measured current was entirely due to the return stroke forced an unreasonably large and abrupt reduction in inferred current amplitude over the first few tens of meters above the surface, especially in cases when the leader was bright relative to its stroke. Therefore, a significant fraction of the current at the surface was probably due to the leader, at least in such cases. 5) Peak return-stroke currents decreased by approximately $37 \pm 12\%$ from 100 m to 1 km of path length above the surface. Because of uncertainty about how to partition the measured current between leader and return stroke, we are unable to infer the variation of current amplitude near the ground.

Introduction

The return strokes in cloud-to-ground lightning flashes are the most powerful known lightning processes in terms of both local energy dissipation and electromagnetic radiation [*e.g.*; Guo and Krider, 1982; Willett *et al.*, 1990]. Although the threat that they pose to objects on the ground has now been reasonably well quantified, the peak electric currents, current rise times, and electromagnetic-field intensities above the surface are not known. These quantities have practical importance to the hardening of aircraft and missiles, which can trigger lightning discharges in flight [Mazur *et al.*, 1984; Christian *et al.*, 1989], since the flashes so triggered are likely to contain return strokes if initiated close enough to the ground. "In testing to determine the immunity of a system to a direct lightning strike... the flash current is generally that observed at the base of a severe flash to ground even though aircraft and space vehicles in flight will likely encounter the smaller currents associated either with the upper portion of return strokes or with various in-cloud currents from either ground or cloud discharges" [Uman, 1988].

In addition to this engineering application, information about the evolution of speed, shape, and amplitude of the upward-propagating current waveform is needed to test, and to guide the further development of, physical models of the return stroke [*e.g.*, Strawe, 1979; Mattos and Christopoulos, 1990]. Such models give predictions of these quantities that (except for propagation speed) have yet to be compared to observations above the surface.

Direct measurements of the current waveforms in both natural and rocket-triggered return strokes exist, but only at the channel base [Berger *et al.*, 1975; Eriksson, 1978; Garbagnati and Lo Pipero, 1982; Leteinturier *et al.*, 1990, 1991; Fisher *et al.*, 1993; Depasse, 1994, Crawford, 1998; Uman *et al.*, 2000; Schoene *et al.*, 2003]. Time-resolved photographic and photo-electric measurements that show the evolution of luminosity along the visible channel on microsecond temporal, and several-meter spatial, scales are also available [Schonland *et al.*, 1935; Idone and Orville, 1982; Jordan and Uman, 1983; Idone *et al.*, 1984; Mach and Rust, 1989; Jordan *et al.*, 1997; Wang *et al.*, 1999]. These optical measurements imply that the propagation speed and the peak amplitude of return-stroke current waveforms both decrease with increasing height above the surface, while the current rise time increases with height.

Unfortunately, the relation between optical emission per unit channel length and instantaneous current is not well known under the conditions found in lightning return strokes.

Colvin *et al.* [1987] found an approximately linear relation between instantaneous current and channel brightness in oscillatory laboratory discharges having current periods of about 2 ms. These discharges were intended to simulate "nuclear lightning," however, so their time scales of were slow enough that pressure equilibrium was well established within the current-carrying channels. Murphy *et al.* [1986, Figure 13] made similar measurements on a laboratory discharge ringing with about 30 μs period and having a current rise rate of approximately 10 kA/μs. (Note that this current derivative is roughly one order of magnitude smaller than those typically measured at the channel base in rocket-triggered return strokes [Leteinturier *et al.*, 1990, 1991; Schoene *et al.*, 2003] but might be comparable to those occurring in lightning channels a few hundred meters above the ground.) Murphy *et al.* [1986] concluded, "This discharge rings on a timescale too short for pressure equilibrium to be established with the surrounding atmosphere, thus its brightness is not a simple function of the discharge current." Gomes and Cooray [1998] measured the optical emissions from the entire length of laboratory sparks in 250 mm and 500 mm gaps. They found that, for a current rise time of 1.1 μs, the optical rise time remained near 1.2 μs over a range of peak currents from 0.6 to 3.5 kA; that optical and current rise times were nearly proportional over a range of 0.3 to 15 μs (peak current varied with rise time); and that peak optical emission was approximately linearly related to peak current, although with a large zero intercept that eliminated any proportionality between these two parameters.

In measurements on rocket-triggered lightning, Idone and Orville [1985] reported approximate proportionality between peak current measured at the ground and peak relative luminosity about 50 m above ground for 20 strokes in one flash and 17 strokes in another. Wang *et al.* [2005] found proportionality between instantaneous current and instantaneous relative intensity in the lowest 3.6 m of channel during the rapidly rising portion only of four triggered strokes. Nevertheless, the contradictory nature of the laboratory results to date makes it premature to deduce current behavior directly from optical-luminosity measurements.

(Note further that rocket-triggered lightning differs from natural cloud-to-ground lightning in that the former has no analog to the natural first return stroke [*e.g.*, Uman, 1987, Section 12.5]. Le Vine *et al.* [1989] have argued the similarity between rocket-triggered and natural subsequent strokes, based on wide-band recordings of their radiation fields, but the current waveforms in natural first strokes are expected to be different for various reasons [see

review and discussion by Willett *et al.*, 1995]. Thus, the results in this paper may not apply to natural first return strokes.)

There are numerous, semi-empirical, "engineering" models of return-stroke currents in the literature [*e.g.*, Bruce and Golde, 1941; Uman and McLain, 1970; Lin *et al.*, 1980; Hubert, 1985; Heidler, 1985; Diendorfer and Uman, 1990]. These and other model variations have been reviewed and extended by Nucci *et al.* [1990], Thottappillil and Uman [1993], and Rakov and Uman [1998]. Many of these models have been tested against observed channel-base-current and remote electromagnetic-field waveforms [Lin *et al.*, 1980; Thottappillil and Uman, 1993; Rakov and Uman, 1998], but only assuming a straight, vertical lightning channel and a "realistic" profile of propagation speed. Le Vine and Willett [1995] have presented evidence, however, that the channel morphology plays an important role in determining the structure of the radiation-field waveform, even for subsequent return strokes.

Master *et al.* [1981] computed the electromagnetic fields to be expected aloft from a nearby return stroke, based on a modification of the model of Lin *et al.* [1980], but they could find no measurements with which to compare their results. More recently, Reazer *et al.* [1987], Mazur *et al.* [1990], and Mazur and Moreau [1992] have presented *in-situ* observations of a few events in direct lightning strikes to aircraft that they believe to have been return strokes, but the evidence for this claim is problematic. Reazer *et al.* [1987] found peak currents of 1-4 kA and rise times around 2 μs in these events, in agreement with the general expectation that return stroke peak currents should be smaller, and current rise times should be longer, aloft than at the ground. Mazur *et al.* [1990] and Mazur and Moreau [1992] did not report peak currents or rise times, but the latter authors state, "...return stroke currents at flight altitudes are much smaller in amplitude than those measured on the ground, and are usually smaller than current pulses of dart leaders and recoil streamers. This observation strongly indicates the need for reexamining the threat to aircraft from return strokes."

Data and Approach

The present paper exploits an existing set of channel-base-current recordings, stereo still photographs, streak photographs, and remote electric-field waveforms of rocket-triggered

lightning return strokes to deduce quantitative features of their current waveforms above the ground. This uniquely comprehensive data set was obtained during the summer of 1987 at the NASA Kennedy Space Center in Florida and has been described in detail by Willett *et al.* [1989]. A novel feature of these data is the stereo pairs of still photographs, which have enabled piecewise-linear reconstruction of the actual three-dimensional geometry of six cloud-to-ground channels, as outlined previously by Willett and Le Vine [1995]. (See Appendix A for further details.) The reconstructed channels are believed accurate to a few tens of meters or better. They are smooth and approximately straight over the lowest few hundred meters, where the lightning followed the triggering wires, and tortuous above. Both current and electric-field-change waveforms were recorded during a total of 24 return strokes in these channels, and stroke-propagation speeds were also measured from the streak photographs for 14 of these strokes in five channels.

It has been shown theoretically [Hill, 1969; Le Vine and Meneghini, 1978; Le Vine and Kao, 1988; Cooray and Orville, 1990; Vecchi *et al.*, 1994] that kinks and bends in a lightning channel should produce signatures in the return-stroke radiation field. For example, if an unchanging current waveform were to propagate at constant speed -- the "transmission-line model" (TLM) of Uman and McLain [1970] -- up such a tortuous channel, each successive kink would radiate a facsimile of the current waveform with an amplitude, polarity, and time delay determined by the geometry of that kink relative to the observer [*e.g.*, Le Vine and Willett, 1992]. Thus, it is tempting to conclude that knowledge of the channel geometry would permit deconvolution of the radiated field to yield the spatial evolution of the current waveform along the channel.

Mathematically, this inverse problem cannot be solved, of course, since the return-stroke current is, in general, a function of both time and path length along the lightning channel, whereas the field waveform observed at a single location is a function of time alone. Even if the current were constrained to reduce its dimensionality from two to one, the solution might not be unique. Here the inverse problem is avoided by solving the forward problem with various assumptions about the current distribution and comparing the results to observation. Preliminary results of this approach have been presented by Willett *et al.* [1989] and by Willett and Le Vine [1996, 2002, 2003].

Calculation of the Field Change

Le Vine and Meneghini [1983, Eq. 26] derived the following equation in vector notation (which has been repeated as Le Vine and Willett [1992, Eq. 1]) for the total electric field due to a TLM current waveform, $I_{TLM}([t - t_a] - \hat{\boldsymbol{l}} \cdot [\boldsymbol{r}' - \boldsymbol{r}_a']/v)$, propagating on an arbitrarily located, arbitrarily oriented, short, linear channel segment in free space. Here v is the propagation speed of the current waveform, $\hat{\boldsymbol{l}}$ is a unit vector in the direction of propagation along the channel segment (also taken to be the positive direction for current flow), and t_a is the *retarded* time that the onset of the waveform, $I_{TLM}(0)$, arrives at the origin of the channel segment, $\boldsymbol{r}_a'$. (This "retarded" time is delayed by the interval, $|\boldsymbol{r}_a' - \boldsymbol{r}|/c$, that is required for information to propagate at the speed of light, c, from the origin of the segment to the observer's location, $\boldsymbol{r}$.)

$$\mathbf{E}(\mathbf{r}, t) = -\frac{\mu_0}{4\pi}\int_{segment}[I_{TLM}]\left\{\hat{\mathbf{l}} - \left(\hat{\mathbf{l}}\cdot\nabla R\right)\nabla R\right\}\frac{ds'}{R}$$
$$-\frac{\mu_0 c}{4\pi}\int_{segment}[I_{TLM}]\left\{\hat{\mathbf{l}} - 3\left(\hat{\mathbf{l}}\cdot\nabla R\right)\nabla R\right\}\frac{ds'}{R^2} \qquad (1)$$
$$-\frac{\mu_0 c^2}{4\pi}\int_{segment}\left\{\int_{-\infty}^{t}[I_{TLM}]\left\{\hat{\mathbf{l}} - 3\left(\hat{\mathbf{l}}\cdot\nabla R\right)\nabla R\right\}dt'\right\}\frac{ds'}{R^3}$$

The integrals in (1) are line integrals that are evaluated along the channel segment. The integrations are to be done in the "primed" coordinate system, where ds' denotes a differential length along the segment, and ∇R is effectively a unit vector pointing from the source point, $\boldsymbol{r}'$, to the observer along the separation distance, $R \equiv |\boldsymbol{r} - \boldsymbol{r}'|$. The square brackets in the integrands in Equation 1 only, ([*function*]), denote the retarded value of the argument of the enclosed function, and the dot above the brackets denotes a derivative with respect to the single argument of that function.

Starting from the first term in (1), Le Vine and Willett [1992, Eq. B3] derived a simple formula for the electric radiation (*i.e.*, "far") field, measured at the surface of an infinite, horizontal, conducting plane, due to a current-carrying channel segment above that plane:

$$\mathbf{E_{rad}}(\mathbf{r}, t) = \frac{\mu_0 v}{2\pi R_0} \frac{\sin(\theta)\left(\hat{\boldsymbol{\theta}} \cdot \hat{\mathbf{l}}\right)\hat{\mathbf{z}}}{\left[1 - \frac{v}{c}\left(\hat{\mathbf{l}} \cdot \nabla R_0\right)\right]} \left[I_{TLM}(t - t_a) - I_{TLM}(t - t_b)\right] \qquad (2)$$

In this formula we have assumed a spherical coordinate system, (R_0, θ, φ), that is centered on the channel segment but has its symmetry axis, $\hat{\boldsymbol{z}}$, oriented vertically -- perpendicular to the conducting plane. (Thus the zenith angle, θ, is greater than 90° for sources above the plane.) R_0 is the distance from the center of the segment aloft to the observer on the ground plane, μ_0 is the magnetic permeability of free space, t_b is the *retarded* time that the onset of the current waveform arrives at the termination of the channel segment, $\boldsymbol{r_b}'$, and $I_{TLM}(argument)$ is the functional form of the current at the center of that segment.

The "induction" and "static" components of the complete electric field due to the same channel segment can be readily computed from the second and third terms of (1), respectively. They and are given in the same notation as (2) by Equations 3 and 4:

$$\mathbf{E_{ind}}(\mathbf{r}, t) = \frac{\mu_0 c \left| \mathbf{r_b}' - \mathbf{r_a}' \right| \hat{\mathbf{z}}}{2\pi R_0^2} \left[\sin(\theta)\left(\hat{\boldsymbol{\theta}} \cdot \hat{\mathbf{l}}\right) + 2\cos(\theta)\left(\hat{\mathbf{l}} \cdot \nabla R_0\right)\right] \cdot I_{TLM}\left(t - \frac{t_a + t_b}{2}\right) \qquad (3)$$

$$\mathbf{E_{stat}}(\mathbf{r}, t) = \frac{\mu_0 c^2 \left| \mathbf{r_b}' - \mathbf{r_a}' \right| \hat{\mathbf{z}}}{2\pi R_0^3} \left[\sin(\theta)\left(\hat{\boldsymbol{\theta}} \cdot \hat{\mathbf{l}}\right) + 2\cos(\theta)\left(\hat{\mathbf{l}} \cdot \nabla R_0\right)\right] \cdot \int_{-\infty}^{t} I_{TLM}\left(t' - \frac{t_a + t_b}{2}\right) dt' \qquad (4)$$

(We have used the average retarded arrival time on the segment in question in order to minimize systematic errors in Equations 3 and 4.)

As with (1), Equations 2 - 4 require the current to obey the TLM, but only within each segment. Thus, any desired current distribution can be approximated by dividing the entire lightning channel into short, linear segments and varying the current waveform and propagation speed appropriately between successive segments. These three equations are used here to calculate the total field change that would be produced at the location of the electric-field-change

sensor by various assumed current distributions over all of the segments that make up each piecewise-linear, reconstructed channel. Further details on this procedure are given in Appendix B.

Formal Assumptions about the R/S Current Distribution

As indicated above, we expect both the propagation speed and the peak amplitude of return-stroke current waveforms to decrease with increasing height above the surface, while the current rise time should increase with height. Thus we adopt a "generalized TLM" current distribution similar to that of Cooray and Orville [1990]. The current as a function of time and position on the lightning channel is given by

$$i(t, s) = a(s)\, I(t_1, s) \tag{5}$$

where t is time measured from stroke onset at the surface, s is path length measured upward from the surface along the tortuous channel, and $a(s)$ is an amplitude factor that allows for permanent charge deposition along the channel. $I(t_1,s) \equiv 0$ for $t_1 \leq 0$, and the current onset is assumed to propagate monotonically upward with position-dependent "TLM velocity," $v(s)$. t_1 accounts for the resulting propagation delay as a function of s:

$$t_1 = t - \int_0^s \frac{ds'}{v(s')} \tag{6}$$

The current waveform that was measured at the surface, $i_0(t)$, is smoothed by convolution,

$$I(t_1, s) = \int_0^{t_1} i_0(t_1 - t')\, K(t', s)\, dt', \quad t_1 > 0 \tag{7}$$

where the limits of integration result from the requirement that both $i_0(t)$ and $K(t, s)$ vanish for $t <$ 0. We use the following form for our "causal" smoothing kernel:

$$K(t', s) = \frac{e^{-\frac{t'}{\tau(s)}}\, t'^2}{2\,\tau^3(s)}, \quad t' \geq 0 \tag{8}$$

which has been normalized to conserve the total charge that is transported up the channel by any given current pulse. Therefore, although the peak amplitude of $I(t_1,s)$ typically decreases with increasing s as a result of increased smoothing, $a(s)$ scales the total charge passing any s. The "equivalent width" (the width of a rectangle with the same peak magnitude and total area) of this convolution kernel is $[\tau(s)\, e^2]/2$. The forms chosen for the various parameters defined above are as follows:

$$a(s) = [a_{min1} + (1 - a_{min1})\, e^{-s/L_{a1}}]\,[a_{min2} + (1 - a_{min2})\, e^{-s/L_{a2}}] \tag{9}$$

$$v(s) = v_{min} + (v_{max} - v_{min})\, e^{-s/L_{v1}} + v_{ampl}\, e^{-s/L_{v2}} \tag{10}$$

$$\tau(s) = \tau_{max}\,(1 - e^{-s/L_\tau}) \tag{11}$$

where a_{min1}, a_{min2}, L_{a1}, L_{a2}, v_{min}, v_{max}, v_{ampl}, L_{v1}, L_{v2}, τ_{max}, and L_τ are constants.

Note that the generalized-TLM form that is adopted here (as opposed to the piecewise TLM requirement in the previous section) restricts somewhat the possible current distributions along the return-stroke channel. Nevertheless, the present assumptions allow us to explore the current variations that we expect, based on optical observations, while introducing a manageable number of free parameters. An understanding of the effects of these various parameters can be obtained by examining the examples of $I(t_1,s)$ in Figure 1 and of $v(s)$ and $a(s)$ in Figures 5 and 7, respectively, below. (The corresponding free-parameter values are given in the figure captions.)

Eleven free parameters may seem like a lot to fit a given observed electric-field-change waveform. Note, however, that we are really just allowing the current amplitude to vary on two different height scales (often required to fit the peak radiation field, as illustrated below), the TLM velocity to vary on two scales as well, and the current rise time to vary on one height scale. In a later section, a physical explanation is offered for on e of the amplitude scales, probably rendering it moot. The second TLM-velocity scale is required for only a few strokes. Finally, it

is not the values of the individual free parameters themselves, but rather the characters of the variations of current amplitude, rise time, and propagation speed with height, that are the real objectives of this investigation. Therefore, our fitting procedure does not turn out to have as many degrees of freedom as it might seem.

Detailed Example of Fitting Procedure -- Stroke 8732/2

The approach that is used in this paper to deduce the evolution of return-stroke current with height comprises the following steps: 1) Guess the current parameters in Equations 9 - 11. 2) Compute the magnitude of the resulting field change, $E_c(t)$, at the observing site from Equations 2 - 4, according to Appendix B. 3) Compare $E_c(t)$ with the measured field change for the same stroke, $E_m(t)$. 4) Iterate until a good fit is obtained. We shall see that this procedure gives reasonably definite results, in spite of the apparent ill-posed-ness of the general mathematical inversion problem. As an example, we examine in detail the fitting of stroke 2 in flash 8732 (stroke and flash identifiers as in Willett *et al.* [1989]).

Smoothing and Extrapolation of the Current Waveform

The channel-base current for these events was recorded for either 20 μs (flashes 8715 and 8717) or 5 μs (flashes 8725 - 8732), including pre-trigger delay. In order to compute $E_c(t)$ for the entire time interval during which the current onset propagates from bottom to top of the visible channel -- typically about 10 μs -- it was therefore necessary to extrapolate the measured current waveforms for more than half of the events in our dataset. Furthermore, the smaller-amplitude waveforms were rather noisy, leading to (1) uncertainty in the precise time of current onset and (2) spurious noise in our piecewise-linear calculation of the radiation field via Equation 2, so some smoothing was beneficial. (If the current waveform is significantly different on adjoining channel segments, errors are produced in the radiated field. These errors can be minimized either by smoothing the channel-base current or by using inconveniently short channel segments near the ground.)

In practice, the onset of the measured current waveform was truncated at some small magnitude (less than the digitization interval), and then the remaining record was smoothed with a tapered, 11-point (60 ns FWHM) moving average. This resulted in a relatively smooth $i_0(t)$ having a definite onset time ($t = 0$) without appreciably changing its rise time or wave shape. Next the decaying portion of the recorded waveform, starting well after the peak, was fitted with the sum of a constant, a linear slope, and (in many of the cases) an exponential decay. The resulting analytic shape was used to extrapolate $i_0(t)$ to later times, as needed. This quasi-objective extrapolation procedure is not regarded as part of the matching of $E_c(t)$ to $E_m(t)$, *per se*. In most cases the results are reasonable (see Figures 2 for two examples), but they appeared to produce artifacts in a few cases, as we shall see later.

Determination of Current Rise Time

The most obvious result of our analysis, first reported by Willett e*t al.* [1989] and by Willett and Le Vine [1996], is that the current rise time must increase rapidly with height (or with path length, s) in order for $E_c(t)$ to resemble $E_m(t)$. Thus, the first step in our fitting procedure was always to adjust τ_{max} and L_τ in Equation 11 in order to obtain an $E_c(t)$ with approximately the right amount of "fine structure."

Figure 3 illustrates the excessive fine structure that is obtained for stroke 8732/2 if $i_0(t)$ (see Figures 2) is allowed the propagate up the reconstructed channel at a constant speed of 1.71 X 10^8 m/s -- effectively the pure TLM. (Note that this propagation speed along our 3-D channel was chosen to be somewhat faster than the measured 2-D propagation speed of 1.6 X 10^8 m/s ± 20% in order to line up the major waveform features in time.) The fine structure on $E_c(t)$ is reduced to a reasonable level, as shown by the green curve in Figure 4, when $\tau_{max} = 4.36$ μs and $L_\tau = 7084$ m (that is, $\tau(s)$ is nearly linear with an *initial* slope of 0.615 μs/km). Unfortunately, the remaining fine structure is now delayed significantly with respect to that of the observed waveform, forcing us to adjust the propagation speed. The reason for this delay is that increased smoothing (via Equations 7 and 8) delays the fast-rising portion of the current waveform by an increased interval relative to current onset [which, by definition, propagates according to $v(s)$] -- see also Figure 1.

Determination of Propagation Speed

The horizontal, solid-green line in Figure 5 illustrates the constant TLM-velocity profile that corresponds to the green curve in Figure 4. In the numerical code it is possible to calculate, at each time step, the propagation speed of the half-amplitude point on the rising portion of the current front, while accounting for the fact that the current waveform is becoming increasingly smooth (the rise time is becoming longer) with increasing height. [Later, this calculation also accounts for a decreasing amplitude factor, $a(s)$, with height.] For $v(s) = 1.71 \text{ X } 10^8$ m/s, the resulting "front velocity, $v_{eff}(s)$," as we call this calculated effective speed, is shown by the green dots in Figure 5. Notice that, not only is $v_{eff}(s)$ significantly lower than $v(s)$, but it also increases somewhat with height.

In general, we adjusted the TLM velocity profile so that the fine structure of $E_c(t)$ coincided in time with that of $E_m(t)$, while striving to keep the front velocity constant or decreasing with height. (The latter was not always possible, however, as shown below.) For stroke 8732/2 a nearly constant $v_{eff}(s)$ was obtained with $v_{min} = 2.1 \text{ X } 10^8$ m/s, $v_{max} = 2.6 \text{ X } 10^8$ m/s, $v_{ampl} = 0$, and $L_{vl} = 500$ m, as shown by the red profiles of Figure 5. Here the average front velocity is almost exactly $1.71 \text{ X } 10^8$ m/s, and the fine structure of the resulting $E_c(t)$ waveform is in good temporal agreement with that of $E_m(t)$, as can be seen from the red curve in Figure 4.

Determination of Amplitude Factor

It turns out to be generally true (at least within the context of Equations 5 - 11) that the amplitude of $E_c(t)$ is directly proportional, not to $v(s)$, but to $v_{eff}(s)$. Thus, it is not surprising to find the peak amplitude of the red curve in Figure 4 (corresponding to $v_{eff}(s) \approx 1.7 \text{ X } 10^8$ m/s) to be about 29% larger than that of the green curve ($v_{eff}(s) \approx 1.3 \text{ X } 10^8$ m/s). Unfortunately, the red curve also peaks about 37% higher than the black curve, $E_m(t)$, indicating that some adjustment of the current amplitude is required.

It is not satisfactory in general to eliminate this "over-prediction" of peak field by adjusting the velocity profile. First, this would normally result in the front velocity's increasing with height, which is considered un-physical. More importantly, it would almost always delay features of the predicted fine structure relative to those observed. Therefore, the only practical

367 way to adjust the amplitude of $E_c(t)$ is to adjust the amplitude factor in Equation 5. In the case of
368 stroke 8732/2, the parameters, $a_{min1} = 0.70$, $a_{min2} = 0.60$, $L_{a1} = 60$ m, and $L_{a2} = 400$ m, result in
369 good agreement, as shown in Figure 6.
370 The corresponding profile of $a(s)$ is given by the red curve in Figure 7. Notice that two
371 height scales are usually required -- a short one to bring the peak field into agreement with
372 observation and a relatively long one to tailor the "tail" of the field-change waveform. As
373 mentioned above, non-uniform $a(s)$ results in a change in the linear charge density on the
374 channel from before to after the return stroke's passage. This "deposited" charge density is
375 proportional to -da/ds, as illustrated in the green curve of Figure 7. Notice that an appreciable
376 fraction of the stroke charge is deposited quite close to the surface in this case. This turns out to
377 be true generally in our dataset and is explained further in a later section.
378
379
380 Fitting Variations and Problem Cases
381
382 *Adjustment of $E_c(t)$ Peak Shape Using Velocity Profile*
383
384 Occasionally it was not possible to match the shape and/or amplitude of the $E_m(t)$ peak by
385 adjusting $a(s)$ alone. In such cases the initial front velocity could often be increased, at the
386 expense of introducing a second height scale for $v(s)$, to yield a larger and/or sharper $E_c(t)$ peak.
387 Figures 8 and 9 show the best example of this type of velocity adjustment and its results for
388 stroke 8732/1.
389
390 *Consequences of the Limit, $v(s) \leq c$*
391
392 There is a physical limit on the TLM velocity -- the current onset cannot propagate up the
393 channel faster than the speed of light. As indicated above, we tried to prevent $v_{eff}(s)$ from
394 increasing with height. This was not always possible, however, without violating the constraint
395 on $v(s)$, especially when a rapid increase in current rise time with height and/or a relatively large
396 $v_{eff}(s)$ was required. The most dramatic example of such behavior is stroke 8728/11, illustrated

in Figure 10. Nevertheless, we were able to fit $E_c(t)$ to $E_m(t)$ quite satisfactorily in this case, as can be seen in Figure 15a, below.

Extremely Fast Decay of Current Amplitude

Several cases require both a_{min1} significantly less than unity and $L_{a1} \leq 10$ m in order to obviate a sharp initial peak on $E_c(t)$. This implies that a significant fraction of the return-stroke charge is deposited in the lowest ~10 m above the ground in these cases (although the need for a very rapid decrease in $a(s)$ will be examined further below). Stroke 8726/3, for which $a_{min1} = 0.69$ and the preferred value of $L_{a1} = 5$ m, is one of the most extreme cases in this regard. Figure 11 compares $E_c(t)$ for three different values of L_{a1} with $E_m(t)$. Evidently the best agreement is for $L_{a1} = 5$ m. Figure 12 shows the resulting profiles of $a(s)$ and linear charge density on an expanded height scale. A possible physical explanation of this and other similar results is offered in the *Discussion* section below.

Probable Failure of Current Extrapolation

In a few cases it appears impossible to get a good fit to the latter part of $E_m(t)$. We have already seen an example in stroke 8732/1 (Figure 9), where the amplitude of $E_c(t)$ becomes too small after the first 6 μs. Since the current for this stroke (see Figure 16a) was extrapolated from a linear fit to less than 3 μs of fairly steeply falling data following the peak, it seems probable that this phenomenon is caused by poor extrapolation. A more extreme example of this behavior is stoke 8725/4. The green waveform in Figure 13 shows the original current extrapolation for this case -- simply our standard constant-plus-linear-plus-exponential fit to some 3.8 μs of descending current record -- which falls to zero about 12 μs after onset. The resulting modeled field change is shown in green in Figure 14 and is seen to disagree with observation after the first 5 μs or so. If we arbitrarily force the current extrapolation to remain high, however (red curve in Figure 13), the resulting $E_c(t)$ -- red curve in Figure 14, all fitting parameters remaining the same -- agrees much better with $E_m(t)$. [This is the only case in which we have "tinkered" with the current extrapolation in order to obtain a better fit to the observed field change.]

[Neglecting the high-frequency noise from the current waveform, notice that there is still too much fine structure in $E_c(t)$, relative to $E_m(t)$, during the first 5 μs of stroke 8725/4. We could not further increase the current rise time during the early part of this stroke while maintaining the observed peak field change without violating the constraint that $v(s) \leq c$. Such a rapid increase of $\tau(s)$ near channel base would significantly reduce $v_{eff}(s)$ there and, consequently, limit $E_c(t)$.]

Summary of Results for All 24 Strokes

Table 1 gives values of the 11 free parameters in Equations 9 - 11 for each stroke in our dataset. A few explanatory remarks are in order here. The "Geometry" values in columns 3 and 4 indicate the path length from the surface to the tip of the triggering wire and to the top of the reconstructed channel, respectively. "Initial Slope" (column 6) is the only parameter quoted for the kernel time scale, $\tau(s)$, in cases where L_τ is much longer than the reconstructed channel, so that the profile of $\tau(s)$ is effectively linear. Values are omitted for unused parameters in $v(s)$ and $a(s)$. Instead of the exponential form specified in Equation 10, a linear decrease of $v(s)$ from an initial value of c appeared to be more appropriate for stroke 8726/1, as indicated in column 12. The last column of Table 1 gives the retarded time at which the onset of the current waveform arrives at the top of the reconstructed channel -- the latest observer time, t, at which $E_c(t)$ can be computed.

Table 2 gives the corresponding values of 10 - 90% current rise time, effective front velocity, $v_{eff}(s)$, and amplitude factor, $a(s)$, at representative path lengths along the channel in each case. It is these values that should be considered the results of our matching of $E_c(t)$ to $E_m(t)$, whereas the parameters in Table 1 are dependent on the specific form that is assumed for the current (Equations 7 - 11). (Recall that the amplitude factor in Equation 5 determines the total charge passing a given point on the channel.) Note that the average of $v_{eff}(s)$ over the entire current-propagation interval -- maximum path length reached by the half-amplitude point on the current waveform divided by the actual (not retarded) arrival time of current onset at the channel top -- is given in column 8, and that values of v_{eff}(1000 m) are omitted from column 12 for the few strokes in which this half-amplitude point never reached s = 1000 m.

Figures 15 compare $E_c(t)$ and $E_m(t)$ for all 24 strokes. The pairs of strokes from three different flashes in Figure 15a make a familiar point: The field-change waveforms that are produced by strokes within the same flash tend to be more similar than those from different flashes [*e.g.*, Le Vine and Willett, 1995]. This is not always the case, however, as illustrated by Figure 15b, in which a single flash is seen to produce two qualitatively different classes of waveforms. Another example, in which two sharply peaked, relatively simple waveforms coexist with three having more rounded peaks and more pronounced fine structure, is shown in Figure 15c. The remaining eight strokes, all from the same flash, are shown in Figure 15d. Notice that we have been able to obtain good agreement in both fine structure and absolute amplitude between modeled and observed field changes over a wide variety of wave shapes. The corresponding extrapolated waveforms of channel-base current are given in Figures 16.

Relative Light Intensity from Streak Photographs

In addition to providing direct measurements of vertically averaged, two-dimensional, return-stroke-propagation speed [see Willett *et al.*, 1989], the streak photographs of 14 of the 24 strokes in five of our six reconstructed lightning channels were processed to determine relative light intensity (RLI) as a function of time and position. A typical leader/return-stroke image from our data set is shown in Figure 17. Such images were digitized, calibrated, and converted to time series of RLI at selected vertical levels. The resulting time series were then smoothed and analyzed to determine both peak amplitude and 10 - 90% rise time of the return strokes, for comparison with similar parameters deduced above for the corresponding current waveforms (see Table 2). This optical analysis is described in detail in Appendix C, and the results are presented in Table 3. Although we don't attempt to infer current amplitudes or rise times from the optical parameters tabulated here, for the reasons explained in the *Introduction*, such a comparison is reasonable in view of the approximately linear relation that we found between RLI amplitude and peak current over our 14 strokes (like that reported by Idone and Orville [1985]) and the similarly linear relation between instantaneous RLI and current during the fast-rising portions of four triggered strokes that was reported by Wang *et al.* [2005].

The reconstructed height above ground and the path length along the lightning channel are shown in Table 3 for each measurement level on each streak photograph. (For comparison with the model results in Table 2, the path length must be used.) As detailed in Appendix C, the stroke RLI amplitude is the difference between the upper and lower limits of the fast-rising portion of the corresponding time series. At levels above the first, the lower limit, or "baseline" (also tabulated), can be viewed as an estimate of the residual brightness of the leader channel, just before stroke onset, since the zero of RLI was determined from the "background" film density prior to leader onset. The uncertainty in RLI amplitude is estimated at about ±0.1, based on the typical noise level illustrated in Figure C1. The uncertainty in rise time is more difficult to estimate, depending as it does on the clarity with which the fast-rising portion is manifest in the RLI waveforms. The error estimates in the last column of the table are based on the scatter among multiple estimates of rise time, where such existed, as described with respect to Figures C2. The worst of these uncertainties are about ±23%, although most are much smaller.

The optical parameters in Table 3 have been plotted against the corresponding electrical estimates in Figures 18a and 18b. Recall that the model peak current, $i_p(s)$, is not identical to the amplitude factor, $a(s)$, given in Tables 1 and 2. $i_p(s)$ is determined by both $a(s)$ (see Equations 5 and 9) and the convolution smoothing (see Equations 7, 8, and 11), which increases with path length as specified in Table 1. Therefore, $i_p(s)$ has been computed and given in Table 4. (The values for zero path length are, of course, those directly measured at the surface.)

Discussion

The entire procedure of adjusting the current-model parameters in order to match the computed $E_c(t)$ waveform to the measured $E_m(t)$ has been illustrated in previous sections. Not only is this procedure somewhat subjective, but the various parameters interact with one another to a greater or lesser extent. We have already seen how the introduction of a current rise time that increases with height, through $\tau(s)$ in Equation 8, causes the effective front-propagation speed, $v_{eff}(s)$, to decrease relative to $v(s)$, although this particular interaction does not cause any ambiguities beyond an occasional encounter with the physical limitation, $v(s) \leq c$. It has also been pointed out that the amplitude of E_c is directly proportional to v_{eff}, so that speed changes

affect the inferred amplitude factor, $a(s)$. Again, this causes no serious difficulties, since both the rise time and the effective speed of the current waveform are strongly tied to observed features of $E_m(t)$.

The amplitude factor, in turn, affects not only the overall amplitude of E_c but also the amplitude of its fine structure. (Compare the red curves in Figures 4 and 6.) Nevertheless, one cannot normally trade off (for example) increased $a(s)$ against increased $\tau(s)$, maintaining the same level of fine structure, because this would make the overall amplitude of E_c too large. A significant concern arises, however, when the extrapolation of the measured current waveform to later times is uncertain, as illustrated in Figure 13 for stroke 8725/4. In such cases it would be possible to trade off (for example) a higher current extrapolation against decreased $a(s)$ -- maintaining the same overall amplitude of E_c but reducing the fine structure -- and decreased $\tau(s)$ -- boosting the fine structure back to the correct level but yielding different inferred current rise time *vs.* height.

This last ambiguity exists to some extent in all 14 strokes having short current records (flashes 8725, 8726, 8728, and 8732), although examination of the measured current and/or computed field-change waveforms in Figures 15 and 16 suggests that it might be a significant problem in only 8 (strokes 8725/2, 8725/3, 8725/4, 8725/5, 8726/1, 8726/4, 8732/1, and 8732/2). Since we have no way of assessing the accuracy of the extrapolated currents at late times in these cases, we cannot accurately evaluate the true uncertainties in the inferred rise time or peak amplitude of the current at those late times. (This is also why we have refrained from tinkering with the measured currents in all cases except 8725/4.) The potential uncertainties in these parameters, primarily at the higher altitudes, due to the extrapolation of measured current waveforms are therefore ignored in the following discussion.

Rise Time of Current

The rapid increase in current rise time with increasing path length, illustrated in Figure 1 for example, is the most robust and inescapable conclusion of the present analysis. We could find no alternative to spreading out the fast-rising current front, at least within the framework of our generalized transmission-line model, to obviate the excessive high-frequency radiation that would otherwise result from the observed channel tortuosity. The first few rows of Table 5 show

551 that the inferred 10 - 90% current rise time, averaged over all 24 strokes in the dataset, increases
552 by a factor of seven, from 0.31 ± 0.17 μs at the surface to 2.2 ± 0.5 μs at 1000 m. (It is worth
553 mentioning that the results do not change much, especially at the higher altitudes, if we average
554 only over the 10 strokes with long current records. In fact, the increase from the surface to 1000
555 m for this subset is nearly a factor of 12, apparently as a result of shorter rise times at the surface
556 for these strokes!) Although there is considerable relative variation from stroke to stroke around
557 these means, the reduction in coefficient of variation from 55% at the surface to only 22% at
558 1000 m suggests that much of this is due to differences among the measured current waveforms
559 at the surface.

560 The accuracy of the individual rise times in Table 2 is difficult to assess, given the
561 qualitative nature of the fitting procedure, but the inferred values appear good to ±20% or better.
562 This uncertainty was estimated by varying the rise time of the assumed current and observing the
563 effects on the computed field change in comparison to the observed waveform. In any case, the
564 uncertainty in deduced current rise time is clearly far too small to negate the overall conclusion
565 here.

566 Referring to the right sides of Figures 18, we see that the optical rise times deduced from
567 the streak photographs are nearly always larger than the inferred current rise times, although the
568 overall trends of these two parameters with increasing path length are roughly parallel in most
569 cases (notable exceptions being 8725/5 and 8726/3). These results are also summarized in Table
570 5, where the estimated optical rise times have been averaged over all 14 strokes and over all path
571 lengths within ±100 m of the nominal 30, 300, and 1000 m levels. (The mean and standard
572 deviation of the path lengths included in each of these averages are also given in the table.)

573 As discussed in the *Introduction*, there are no direct comparisons in the literature for the
574 current rise times inferred by our modeling. We can, however, compare our optical rise times
575 with other optical measurements. Most relevant is the streak-recording analysis of Jordan *et al.*
576 [1997] on dart leader and return stroke luminosity variation with height. Indeed, the return-
577 stroke rise-time variation with height cited by Jordan *et al.* (1.5 to 4.0 μs between ground and 1.4
578 km aloft) is very similar to that presented here in Table 5. Also, Olsen *et al.* [2004], using a
579 photoelectric technique applied to a triggered flash, provided in their Figure 3 a series of
580 luminosity traces that have very similar characteristics to ours. Mach and Rust [1989] also
581 presented some luminosity traces from a photoelectric sensor that are apparently quite consistent

582 with our derived traces. On the other hand, Wang *et al.* [1999] reported that the 10 - 90% rise
583 time of RLI in two triggered return strokes increased by factors of 2 and 3.5 over the lowest 40 -
584 45 m of channel, a region rarely imaged in time-resolved photography.
585 Comparing estimated optical and inferred current rise times in Table 5, we see that the
586 former average about 1 μs longer than the latter at 30 m and 300 m but almost 2 μs longer at 1
587 km. These differences cannot be fully explained by the approximately 0.5 μs time resolution of
588 the streak camera that was used for these measurements. In addition to the uncertain relationship
589 between luminosity and current in return strokes (see literature review in the *Introduction*),
590 however, there are two possible reasons for the greater discrepancy at the highest altitudes (latest
591 times) in the present dataset: 1) The uncertainty in our estimates of RLI rise time tends to be
592 relative (see the last column of Table 3), so that the absolute uncertainty is greater for the larger
593 values. This might be due, in part, to our use of stronger temporal filtering for the slower-rising
594 waveforms, which also tend to have smaller amplitude (lower signal-to-noise). 2) The uncertain
595 current extrapolations in some cases (see the beginning of the *Discussion* section) result in
596 greater uncertainty in the inferred current rise times (and amplitudes) at late times (high
597 altitudes).
598
599 *Propagation Speed*
600
601 Table 5 also gives the mean, inferred, effective, current-front-propagation speeds, both at
602 four representative path lengths above the surface and averaged over the full extent of the
603 reconstructed channel for which this parameter could be computed. The individual inferred
604 speeds (see Table 2) are fairly consistent from stroke to stroke -- they have low a coefficient of
605 variation around their mean at each level -- the only obvious outlier being 8725/4, with an
606 averaged speed of only 0.9 X 10^8 m/s. The means are also fairly uniform with height at about
607 1.8 X 10^8 m/s, in spite of the fact that there is a substantial (and apparently unavoidable) increase
608 in $v_{eff}(s)$ with height in two strokes (8728/10 and 8728/11) and an appreciable decrease with
609 height in one other (8726/1). These trends in propagation speed should not be taken very
610 seriously, as mentioned earlier, but the averaged speeds are probably good to better than ±10% --
611 it's fairly easy to detect and eliminate timing differences between the computed and measured
612 fine structure. The variation of averaged v_{eff} from stroke to stroke is probably also real.

The mean, two-dimensional, optical propagation speed, v_{2D}, over 14 of these same strokes in five of the six channels is given in Table 5 for comparison, from original data (averaged over the lowest several hundred meters of channel) reported by Willett *et al.* [1989]. Note that our mean, averaged, three-dimensional v_{eff} is about 23% larger than the mean, averaged, 2-D, optical speed. This difference is not too surprising in the light of previous work on 2-D *vs.* 3-D channel lengths by Idone *et al.* [1984]. It can also be seen from Table 3 that the ratio of the total path length to the vertical height from the surface to optical level nine averages 1.45 ± 0.30 over our six reconstructed channels.

Once again there are no direct comparisons for our inferred current-front speeds, but the originally reported optical two-dimensional mean speed of 1.5×10^8 m/s is quite consistent with the results of Idone *et al.* [1984] and Mach and Rust [1989], both of which had sizeable numbers of strokes analyzed from triggered flashes over comparable heights.

Amplitude of Current

The mean, inferred, charge-amplitude multiplier, $a(s)$, can be seen in Table 5 to decrease from unity at the surface (by definition) to 0.68 ± 0.08 at 100 m and to 0.49 ± 0.09 at 1000 m. (It is worth mentioning that the result at the 1000 m level does change appreciably when we average only over the 10 strokes with long current records. This suggests that $a(s)$ in the upper parts of the channels *might* be affected significantly by our extrapolation of the corresponding surface current records, as mentioned in the sub-section, *Rise Time of Current.*) The relative variability of the values for individual strokes at the various levels is quite small, although 8725/3 and 8726/1 might be considered outliers at the lower levels (see Table 2). As before, the uncertainty in our inferred values of $a(s)$ (and in the peak currents in Table 4, discussed below) was estimated to be $\pm 10\%$ or better by varying $a(s)$ and observing its effects on the computed field-change amplitude in comparison to the observed waveform. This low apparent uncertainty should not be too surprising, since amplitude differences between computed and measured field change are fairly easy to detect and eliminate.

Recall from earlier sections that two length scales were usually required for $a(s)$ -- a shorter one of a few tens of meters or less to fit the peak measured field change, E_{mp}, and a longer one of a few hundred meters to fit the amplitude of $E_m(t)$ at later times. We have tried to

644 capture the relative importance of these two scales by focusing above on the 100 m and 1000 m
645 levels, but it can be seen better by examining the relevant fit parameters in Table 1. Mean values
646 of these parameters over the 19 strokes for which all four of them are defined are $a_{min1} = 0.72 \pm$
647 0.09, $L_{a1} = 31 \pm 29$ m, $a_{min2} = 0.62 \pm 0.15$, and $L_{a2} = 430 \pm 280$ m. As mentioned previously
648 (*e.g.*, Figure 12), the very rapid decreases in $a(s)$ with increasing path length that are inferred in
649 several cases imply that these return strokes deposit a significant fraction of their total charge in
650 the lowest few tens of meters above the surface.
651 Such localized charge depositions are *not* implied by very close measurements, however.
652 For example, Schoene *et al.* [2003] found that the ratio of return-stroke electric-field change
653 measured 15 m from the channel base to that at 30 m range averaged 1.76 ± 0.15 over 77 rocket-
654 triggered strokes, suggesting a range dependence of $r^{-0.8}$ -- a fall-off noticeably slower than $1/r$.
655 This may be compared with a similar average ratio for the field change due to the immediately
656 preceding dart leaders of 1.88 ± 0.15, suggesting a range dependence of $r^{-0.9}$. Such a slow fall-
657 off of field change with range could be interpreted to indicate that the magnitude of the linear
658 charge density deposited by the stroke (usually assumed to be equal and opposite to that
659 deposited by the leader) *increases* with height over the lowest hundred meters of so of channel
660 [Rakov *et al.*, 1998]. In contrast, our own calculations of the close field changes that would be
661 produced by model strokes having very rapid decreases in $a(s)$ (such as 8725/3 and 8726/3)
662 predict a fall-off with range that is considerably *faster* than $1/r$ within a few tens of meters of the
663 channel base.
664 We have found only one reference in the literature that appears consistent with our
665 inference of rapidly decreasing $a(s)$ near the surface. Wang *et al.* [1999] reported that time-
666 resolved optical imaging near the channel base of two triggered strokes showed peak RLI to
667 attenuate by about 30% over the lowest tens of meters. In spite of this lone observation,
668 however, the discrepancy between our inference and the recent observations of close electric
669 fields cited above leads us to question the meaning of our deductions. An alternative
670 interpretation that is motivated by our streak images and appears more physically reasonable is
671 proposed in the next section.
672 Further insight into the need for coupling a value of a_{min1} that is significantly less than
673 unity with a very short L_{a1} in certain cases (especially 8715/7, 8715/9, 8715/10, 8725/3, 8725/5,
674 8726/1, 8726/3, and 8726/5) can be obtained by comparison of the physical propagation speeds

675 that are discussed above with the so-called transmission-line-model velocity, $v_{TLM} \equiv -$
676 $(2\pi D/\mu_0)E_{mp}/i_p(0)$ [*e.g.*, Willett *et al.*, 1989]. This v_{TLM} is just another way of looking at the ratio
677 of peak radiation field measured at horizontal range, D, to peak current measured at the surface.
678 Its values have been recalculated at our observing range, $D = 5.2$ km, using the new zero and
679 peak levels of $E_m(t)$ that are shown in Figures 15, where we have attempted to better remove any
680 field change due to the leader. The ratio of observed v_{2D} to calculated v_{TLM} averages 1.17 ± 0.20
681 over the 14 strokes for which both are available. The fact that v_{2D} tends to be the larger of the
682 two indicates that its use as a physical propagation speed for the return-stroke current front in our
683 (or any other transmission-line-like) model will tend to over-predict E_{mp} in many cases (as
684 already found, though to a lesser extent, by Thottappillil and Uman [1993]) unless draconian
685 measures are taken to prevent this.

686 We have already seen in the previous section that the inferred 3-D speed, $v_{eff}(s)$, when
687 averaged over most of the reconstructed channel, tends to be even larger than v_{2D}. Thus, it is not
688 surprising that $v_{eff}(10)/v_{TLM}$ (where the effective front speed at the 10 m level from Table 2 has
689 been used as the most relevant to the peak of $E_c(t)$) averages 1.34 ± 0.32 over all 28 return
690 strokes. This implies an even greater over-prediction of E_{mp} in the present modeling, as
691 illustrated in Figure 4 for example. To obviate this over-prediction, a very rapid decrease in $a(s)$
692 with increasing path length is required in several cases. Indeed, the same strokes listed in the
693 previous paragraph have among the largest ratios, $v_{eff}(10)/v_{TLM}$.

694 Inferred peak currents at several levels have been listed in Table 4 for the 14 strokes also
695 having streak photographs. Mean values of $i_p(s)$ are given in Table 5 for comparison with the
696 corresponding average amplitudes of relative light intensity from Table 3 (shown in the same
697 manner as those of 10 - 90% RLI, discussed above). It is gratifying that both of these averages
698 decrease at roughly the same rate with increasing height. (The agreement becomes nearly
699 perfect if the mean RLI amplitude at optical level one is compared with i_p at the surface instead
700 of that at 30 m. An argument for this adjustment will also be discussed in the next section.)
701 Looking back at the left sides of Figures 18, we also see that individual profiles of $i_p(s)$ and RLI
702 amplitude agree reasonably well, both in slope and in overall relative magnitude, although
703 exceptions to the former include strokes 8715/10 and 8726/1 and exceptions to the latter include
704 8726/2, 8726/3, 8726/4, 8732/1, and 8732/2.

705 The evolution of relative light intensity with height in return-stroke channels has also
706 been evaluated photographically by Jordan and Uman [1983] and by Jordan *et al.* [1997]; Mach
707 and Rust [1989] do not present formal analyses, but assert that their photoelectric data is
708 generally consistent with that of Jordan and Uman [1983]. Fundamentally, the peak luminous
709 intensity of the subsequent return stroke is observed to decrease with height by about a factor of
710 two over 500 m, in fair agreement with the present results.
711 Another noteworthy feature of the left sides of Figures 18 is that the RLI amplitude at
712 optical level one is occasionally much brighter than that at level two. That is, there is sometimes
713 a dramatic change in the slope of the amplitude profile at level two. This is especially evident in
714 strokes 8715/9, 8726/2 and 8728/10. Looking at the streak photographs themselves, it is obvious
715 that the first and last of these three strokes, plus 8725/3 and 8726/1, are preceded by particularly
716 bright dart leaders. Figure 19 shows the most dramatic example, stroke 8725/3, which may be
717 compared with more typical stroke 8725/1 in Figure 17. Since the optical emissions from leader
718 and return stroke are generally indistinguishable at optical level one, because of the limited time
719 resolution of the streak camera, the tabulated values of stroke RLI amplitude at the lowest
720 measurement level must have been significantly exaggerated by leader light emission in at least
721 some cases.
722 An objective evaluation of any such exaggerated stroke brightness at the lowest optical
723 level would involve a comparison of the brightness of the leader relative to its return stroke.
724 This comparison can be made reasonably quantitative by forming the ratio, from Table 3, of the
725 RLI "baseline" to its "amplitude" at each level. Recall that this baseline is measured
726 immediately before the onset of the return stroke and thus approximately represents the *residual*
727 brightness of the leader channel (relative to a zero at the same level before leader onset), whereas
728 the amplitude is the difference between the peak RLI during the onset of the return stroke
729 (relative to the same zero) and the corresponding baseline value. (At the higher levels this
730 baseline value may be substantially less accurate than the stroke amplitude because considerable
731 time may have elapsed since the corresponding zero reading. Note that the leader *tip* is often
732 appreciably brighter, as in Figure 21, but is not measured here.) This ratio has been calculated
733 for each stroke at every level (except where "baseline" is negative or where "amplitude" is small
734 enough to produce excessive noise in the ratio) and then averaged over all levels except the
735 lowest (where leader and return stroke are presumed indistinguishable). The results are

indeterminate in two cases (8725/5 and 8726/3) because of low return-stroke amplitudes, but otherwise range from near zero (strokes 8726/2, 8726/4, 8732/1 and 8732/2) to over 30% (8715/9, 8725/3, 8726/1, and 8728/10), the largest ratio being 59% for stroke 8725/3.

The first indication that anomalously bright dart leaders do occur was from Guo and Krider [1985], who reported one or more of them in about 5% of natural multiple-stroke flashes in Florida and argued that leader brightness might occasionally equal or even exceed that of the corresponding subsequent return stroke. Idone and Orville [1985] found that the ratio of dart-leader to return-stroke RLI (measured 50 m above the channel base) averaged 0.1 ± 0.07 over 22 triggered strokes in which leader brightness could be measured; and they estimated the corresponding ratio of peak currents to average 0.17, but with a rather large range of [0.03, 0.3]. Jordan *et al.* [1997] reported that the brightest three of 23 dart leaders in natural subsequent strokes had peak RLIs 30 - 50 % that of the corresponding return strokes. They also referred to (but did not report) measurements of the "plateau" brightness -- after the dart peak but before the stroke onset -- which is the quantity that is approximated by the "baseline" values in our Table 3. Mach and Rust [1997] reported what they called "postdart" brightness relative to that of the dart peak. Dividing mean values from their Table 1, we infer an average ratio of postdart to return-stroke peak brightness of roughly 1/16. Finally, Kodali *et al.* [2005] reported a mean ratio of dart-leader current (inferred from their near-field measurements on triggered strokes, assuming the leader current above the tip to be uniform and constant) to measured return-stroke peak current of 0.22. Based on these references, the values in our Table 3 seem reasonable.

Leader vs. Return-Stroke Current

Table 6 compares our objective measure of leader/return-stroke relative brightness with two possible indicators of draconian measures to fit E_{mp} -- $a(100)$ and $v_{eff}(10)/v_{TLM}$, both discussed in the previous section. As expected, the correlation coefficient between $a(100)$ and $v_{eff}(10)/v_{TLM}$ is high -- -0.88 over all 24 strokes, significantly different from zero at well over the 99% confidence level. The correlations of our leader/return-stroke brightness ratio with these two parameters are -0.74 and +0.41, respectively, over 12 strokes. Thus, the brightness ratio is significantly correlated with the 100 m charge-amplitude multiplier at the 99% confidence level, although its correlation with the velocity ratio is not statistically significant. These results

767 suggest that the peak currents measured at the surface exaggerate those in the return strokes
768 themselves by essentially the same mechanism described above, at least in cases of relatively
769 bright (high-current) leaders. We suspect that this is the reason for the above-mentioned
770 tendency toward over-prediction of E_{mp}, as well as for the extremely rapid decreases in $a(s)$ that
771 we have employed to obviate it.
772 Although this is a new idea, to our knowledge, the relationship between leader and
773 return-stroke current that it presumes is not new. For example, Lin *et al.* [1980] assumed that the
774 leader current continues to flow after the onset of the return stroke, remaining uniform and
775 constant above the advancing return-stroke front. This concept is re-iterated by Jordan *et al.*
776 [1997], who remarked that the optical "plateau" that they observed in natural dart leaders
777 suggested "that a steady leader current flows through each channel section behind the downward
778 moving leader tip before, and perhaps for some time after, the return stroke has passed that
779 channel section."
780 Consider the following simple argument, based on the transmission-line model. (Here we
781 ignore the transient effects of any upward-connecting discharges and/or reflections at the ground
782 on the currents and radiation fields in these triggered subsequent strokes.) Let the current and
783 front-propagation speed of the dart leader be i_L and $-v_L$, respectively, while the corresponding
784 parameters for the return stroke are i_S and $+v_S$. Near the surface the leader front radiates a field
785 proportional to $-i_L v_L$ that turns off when the leader reaches ground. The return stroke then begins
786 radiating a field proportional to $-i_S v_S$ as it propagates up the leader channel from ground.
787 Assume, with the references in the previous paragraph, that the leader current continues and
788 remains uniform along the channel after stroke onset. The peak total current at any level
789 (including that measured at stroke onset by a shunt at the surface) is then $i_L + i_S$, which may be
790 significantly greater than i_S alone in cases with relatively bright leaders. Since $i_L < i_S$ and $v_L <<$
791 v_S, however, the *change* in radiated field magnitude at return-stroke onset is proportional to $-i_S v_S$
792 $- (-i_L v_L) \approx -i_S v_S$. (For example, taking the average ratios, $v_L \approx v_S/6$ from Idone *et al.* [1984] and i_L
793 $\approx 0.22 i_S$ from Kodali *et al.* [2005], we find a radiation-field change proportional to $-0.96 i_S v_S$.)
794 Thus, it is essentially only the return-stroke current itself that is relevant to the distant (radiation)
795 field change. Our measured $E_m(t)$ at $D = 5.2$ km consists essentially of radiation field at the time
796 of E_{mp}, so this analysis should be relevant here.

The above argument appears consistent with both the streak photographs and our inferred rapid decreases of $a(s)$ and $i_p(s)$ in cases of relatively bright leaders. We claim that the latter are merely the inevitable result of presenting our model-fitting procedure with exaggerated measurements of return-stroke-current amplitude at the surface. It even makes sense to compare the mean RLI amplitude at optical level one with i_p at the surface if both measurements then fully include the effects of the leaders. If correct, this argument obviously also has implications for the widespread estimation of return-stroke speeds from measured E_{mp} and $i_p(0)$ through v_{TLM}. This matter could be further investigated using modern, near-field measurements, such as have been reported recently from Camp Blanding, Florida [*e.g.*, Kodali *et al.*, 2005], together with far-field measurements of the peak fields radiated by the same return strokes.

The question remains whether the above inferences about $a(s)$ and $i_p(s)$ can be corrected for this effect. Since we do not know how to accurately remove the leader current from the measured surface-current waveforms, however, we confine ourselves here to a single illustrative example. In stroke 8725/3 both the velocity ratio, $v_{eff}(10)/v_{TLM} = 1.62$, and the level-averaged leader/return-stroke brightness ratio, 0.59, suggest that the peak current due to the return stroke alone should be reduced to about 62% of the measured peak current at the surface. In the model, a slightly larger reduction of this peak current to 56% of the measured value allows us to entirely eliminate the shorter of the two length scales for $a(s)$. (To achieve this reduction, the measured waveform is decreased to 56% of its original magnitude throughout the time interval before its peak, whereas a constant 18.9 kA is subtracted from it at all later times. Obviously this method of modifying the current waveform is somewhat arbitrary.) A fit of $E_c(t)$ to $E_m(t)$ that is essentially the same as that shown in Figure 15c can then be obtained using $a_{min1} = 0.82$, $L_{a1} =$ 500 m, and $a_{min2} = 1.0$ (all other parameters remaining as in Table 1). The resulting measurements of 10 - 90% current rise time and of effective stroke-front speed at the various levels remain essentially unchanged from those in Table 2. Although $a(s)$ changes dramatically, of course, $i_p(s)$ changes from the values in Table 3 only at the lowest two levels, remaining essentially the same at 30, 100, 300, and 1000 m. This result is considered to corroborate our suspicion of exaggerated return-stroke currents near the surface.

Thus, the inference in Tables 1, 2, 4, and 5 (and elsewhere) of very rapid decreases in $a(s)$ and $i_p(s)$, and the consequent concentrations of charge deposition that are illustrated in Figures 7 and 12, near the surface in several cases are probably invalid. These artifacts are

argued to result from using the total measured current at the surface as the initial current into the base of the return stroke itself. There is no fully satisfactory way to correct this problem in the present dataset. Nevertheless, it appears that the inferred values of current rise time at all levels and of average effective stroke-propagation speed are unaffected, even in strokes with very bright leaders. Further, we believe our inference of decreasing current amplitude above about 100 m of path length (taken as a compromise between the mean values of $L_{a1} = 31$ m and $L_{a2} = 430$ m, noted in the previous sub-section, the former length scale now being assumed to be largely spurious). The last two rows of Table 4 are intended to better distinguish the presumed valid and the probably invalid variations of inferred peak current. There we have first scaled the values tabulated for each stroke relative to that at 100 m and then calculated means and standard deviations of these scaled results for each level. We conclude that the peak current probably does decrease by about 37%, on averaged, between 100 m and 1000 m of path length above the ground. On the other hand, the peak current may well increase much less than 58%, on average, between 100 m and the surface.

Summary and Conclusions

This paper has attempted to take advantage of three-dimensional channel reconstructions of rocket-triggered lightning flashes in Florida in order to infer the behavior of the current in return strokes above the ground from current waveforms measured at the channel base and electric-field-change waveforms measured at a range of 5.2 km. The reconstruction of six lightning channels from stereo photographs was described in detail in Appendix A. The method of calculating field-change signatures due to return strokes that follow these piecewise-linear channels was then explained. Formal assumptions about the variation stroke-current waveforms along the channels constrained the problem enough that the rise time, propagation speed, and peak amplitude of the current could be estimated as a function of path length with reasonable confidence. Results were first presented on the tacit assumption that the measured current waveforms were entirely due to the return strokes themselves.

Some of the results derived in this way that we still believe are the following: 1) The fine structure of the field-change waveforms that are radiated by subsequent return strokes can be

859 explained, in large part, by channel geometry, although it can also be affected significantly by
860 the shape of the current waveform that enters the channel base. 2) The average 10 - 90% rise
861 time of the stroke current increased by about a factor of seven in our sample of 24 triggered
862 strokes, from an observed 0.31 ± 0.17 μs at the surface to an inferred 2.2 ± 0.5 μs at 1 km path
863 length above the surface. 3) The three-dimensional propagation speed of the current front
864 averaged $1.80 \pm 0.24 \times 10^8$ m/s over channel lengths typically greater than 1 km for the same 24
865 strokes.

866 Next, streak photographs of a subset of these return strokes were analyzed in terms of
867 relative light intensity versus path length and time, and the resulting estimates of rise time,
868 propagation speed, and peak amplitude of the RLI were compared with the corresponding
869 electrical estimates for current. Although these comparisons appeared generally reasonable, two
870 anomalies were noted that suggested a variation in the modeling. First, it was remarked that
871 even the optically measured, two-dimensional, stroke-propagation speeds (which were an
872 appropriate factor smaller than the electrically inferred, three-dimensional, current-front-
873 propagation speeds) led to an over-prediction of peak radiation fields in several cases, unless
874 draconian measures (which appeared to conflict with other results in the literature) were
875 employed to obviate this. Second, it was noted that peak RLI amplitudes for return strokes
876 sometimes decreased dramatically between the lowest measurement level, where the leader and
877 return stroke could not be distinguished, and the next higher level, where they could be. Both of
878 these anomalies tended to occur most markedly in cases where the leaders were brightest relative
879 to their strokes. It was concluded that (4) a significant fraction of the measured current at the
880 surface was probably due to the leaders in cases when they were relatively bright. Therefore, our
881 assumption that these measured currents were entirely due to the return strokes was forcing an
882 unreasonably large and abrupt reduction in inferred current amplitude over the first few tens of
883 meters above the surface.

884 With this conclusion in mind, the first inferences of current amplitude as a function of
885 height were re-examined. It was judged that the anomalously abrupt decreases with increasing
886 height near the surface were probably spurious, but that the slower increases at higher altitudes
887 were probably still valid. Thus, the final conclusion of our study was that (5) return-stroke peak
888 currents decreased by about $37 \pm 12\%$ from 100 m to 1 km of path length above the surface over

our 24 strokes. Although these peak currents likely also decreased between the surface and 100 m, this decrease was probably not as great as originally inferred.

Appendix A -- 3-D Channel Reconstruction

Figure A1 shows one example (flash 8732) of the six stereo pairs of still photographs that were taken with automated 35 mm cameras from the two sites (NRL and SUNY) during the 1987 experiment. These photographs were all printed at the same magnification (6.8X) on 8" X 10" paper, and the lightning channels were then digitized by marking a point at every visually detectable deviation from straight lines. Typically, this produced a few hundred points per channel image that were tabulated in centimeters (X, Y) relative to the "principal point" [Hallert, 1960, p.18], which was taken to be at the center of the print (±0.5 cm). Connecting these points with straight lines results in a piecewise-linear representation of the channel.

Figure A2a shows the locations of the two cameras relative to the triggering site, which is taken as the origin of a right-handed, Cartesian coordinate system (x, y, z) with its z-axis vertical and its x-axis passing through the NRL site (almost due east of the triggering site). The position parameters for each site are given in the figure, as determined (±0.6 m) from a survey of the area that was conducted by KSC. The azimuthal orientation of the cameras (rotation about the vertical axis passing through each camera -- *e.g.*, γ_S in Figure A2b) could not be accurately measured in the field, but the "swing" (rotation of the image frame about the "optical axis" -- the ray passing through the optical center of the lens and the principal point on the image) was approximately zeroed (±0.3 deg.) by leveling the camera bodies, and the camera elevation angles (rotation about the horizontal axis that is perpendicular to the optical axis -- *e.g.*, α_N in Figure A2c) were estimated (±0.5 deg.) with a spirit level to be 10.0 deg. at NRL and 9.5 deg. at SUNY. Finally, the focal lengths of the camera lenses (nominally 55 mm at NRL and either 35 mm or 24 mm at SUNY) were carefully measured (±1%) to be 54.7 mm, 35.7 mm, and 23.7 mm, respectively. The "barrel distortion" of the 24 mm lens that produced all of the SUNY photographs except that of flash 8715 was also measured and was applied to correct the corresponding tabulations (but see the discussion below).

Extrapolating the lightning channels (which were nearly straight at the bottom, following the triggering wires) to ground level (estimated from the measured camera elevation angles), it was possible to accurately determine the azimuth angles of the two camera optical axes (*e.g.*, γ_S in Figure A2b). This procedure was insensitive to small errors in the camera elevation angles because the triggering wires were nearly vertical. By visually identifying the top of the triggering wire on each image and forcing these points to coincide in the 3-D reconstruction of each channel, it was also possible to correct the measured elevation angle of the NRL camera (α_N in Figure A2c -- note that this sketch has been slightly simplified and gives the precise definition of α_N only when $\gamma_N = 0$ so that the optical axis lies in the x-z plane) relative to that of the SUNY camera, which was assumed correct. It would have been better to have two or more fixed objects of known location in the field of view of both cameras, from which to fully determine the camera orientations, but the triggering site was not suitable for this refinement. Table A1 lists the camera-orientation parameters that were determined in this manner. Notice that the deduced camera azimuths, as well as the corrected elevation of the NRL camera, varied slightly from flash to flash, presumably due to instability of the tripods on which they were mounted.

The formulae of Hallert [1960, Appendix A], together with the camera-orientation parameters tabulated above, have been used to convert the points (X, Y) that were digitized from the photographic prints into absolute angle pairs (θ, φ) -- elevation measured upward from horizontal and azimuth measured clockwise from the direction of the y axis, respectively -- that define rays from the camera positions. Then the position parameters in Figure A2a have been used to compute the intersections of these rays (x, y, z) in our Cartesian coordinate system. The latter step is non-trivial and was performed in practice by solving simultaneous equations with the Mathematica (TM) software, following an outline originally due to Stan Heckman [personal communication, 1995].

Figure A3 is a conceptual illustration of the channel-reconstruction procedure. (Note that α_P here has been given the opposite sign from Figure A2a, solely for convenience of illustration.) The central problem is that, in general, it is not possible to identify any given point on the lightning channel in one image with the corresponding point in the other image. Therefore, this is *not* the classical double-theodolite problem, where there is redundant data (four angles to determine a point in 3-space). A heuristic description of the channel-reconstruction method is as follows. The ray, l_r, that is defined by point r in the first camera image can be projected onto the

second camera image as the line, l'_r, which intersects the second channel image somewhere (in general, between two of the vertices, s and s+1, as shown in the inset of Figure A3). This intersection point -- call it s' -- defines a ray from the second camera, $\boldsymbol{l}_{s'}$, that intersects the first ray, defining a point in 3-space -- identified by the indices, (r, s') -- on the reconstructed channel. The apparently redundant piece of information (the fourth angle) is effectively used up to determine the intersection point, s', on the second channel image.

Mathematically, our solution of this problem proceeds from two vector equations, each specifying the location in 3-space of the intersection point, $\boldsymbol{r}$, of rays $\boldsymbol{l}_r$ and $\boldsymbol{l}_{s'}$ in terms of the angles, (θ_i, φ_i), and the range, r_i, from camera i:

$$\mathbf{r} = \mathbf{r}_{01} + r_1\left[\hat{\mathbf{x}}\sin(\phi_1)\cos(\theta_1) + \hat{\mathbf{y}}\cos(\phi_1)\cos(\theta_1) + \hat{\mathbf{z}}\sin(\theta_1)\right]$$

$$\mathbf{r} = \mathbf{r}_{02} + r_2\left[\hat{\mathbf{x}}\sin(\phi_2)\cos(\theta_2) + \hat{\mathbf{y}}\cos(\phi_2)\cos(\theta_2) + \hat{\mathbf{z}}\sin(\theta_2)\right] \qquad \text{(A1)}$$

The $\boldsymbol{r}_{0i}$ are the positions of the two cameras; $\hat{\boldsymbol{x}}$, $\hat{\boldsymbol{y}}$, and $\hat{\boldsymbol{z}}$ are the unit vectors in our Cartesian coordinate system. Equating these two expressions for $\boldsymbol{r}$, we obtain three linear scalar equations in two explicit unknowns, r_1 and r_2. Recall, however, that the angles from camera 1, (θ_1, φ_1), are implicitly functions of the index, r, whereas those from camera 2 are implicitly functions of s -- we have linearly interpolated the angles between integral values of these indices -- and that it has not yet been explained how to find the s' (see Figure A3) that corresponds to any particular value of r. Given r, we might simply solve numerically the three simultaneous equations (now non-linear in the implicit variable, s) for r_1, r_2, and s', as Stan Heckman [personal communication, 1995] originally suggested. Once r_1 and r_2 are known, it is obviously trivial to find $\boldsymbol{r}$ from either of Equations A1. (This approach might be generalized to find the "best" solution, in the least-squares sense, from three or more camera images of a single lightning channel.) Because we have only two cameras, however, the computation can be simplified as follows:

Three linear equations in two unknowns have a unique solution if and only if the rank of the 3X2 coefficient matrix and the rank of the 3X3 "augmented matrix," $\boldsymbol{A}$ (containing an additional column of the constant terms), both equal two [*e.g.*, Boas, 1966, Section 3.7]. Thus,

the determinant of the augmented matrix must equal zero. Given a particular value of r, the non-linear equation

$$\det(\boldsymbol{A}) \equiv 0 \qquad \text{(A2)}$$

can be solved numerically for the implicit variable, $s'(r)$. From Equations A1 the augmented matrix is found to be

$$\boldsymbol{A} = \begin{pmatrix} -\sin(\phi_1)\cos(\theta_1) & \sin(\phi_2)\cos(\theta_2) & x_{01} - x_{02} \\ -\cos(\phi_1)\cos(\theta_1) & \cos(\phi_2)\cos(\theta_2) & y_{01} - y_{02} \\ -\sin(\theta_1) & \sin(\theta_2) & z_{01} - z_{02} \end{pmatrix} \qquad \text{(A3)}$$

where (x_{0i}, y_{0i}, z_{0i}) are the known Cartesian components of $\boldsymbol{r}_{0i}$, the angles, (θ_1, φ_1), are known functions of the specified index r, and (θ_2, φ_2) are known functions of the unknown index, s. Once s' is determined, the two linear equations with the largest determinant are solved for r_1 and r_2, and $\boldsymbol{r}$ is found.

Occasionally, Equation A2 has multiple solutions for s' at a given r. One way to deal with this situation is as follows. Notice that the two rays, one from each camera intersecting at the reconstructed channel point (r, s') in Figure A3, define a plane. This "solution plane" is fully determined by the locations of the two cameras and by the point, r, on the first channel image, as described heuristically above. The plane cuts each camera image in a projection line, as further illustrated by l'_r and $l'_{s'}$ in Figures A4, where these projection lines correspond to the point, r = 155, on the NRL channel image of flash 8732. [Channel points are numbered here in ascending order from the channel base upward. Note that Figures A4 actually show the "image planes" after transformation from the original linear measurements on each print, (X, Y), into the absolute angles (θ, φ) -- independent of camera orientation, focal length, etc. -- since this was the notation in which the data were analyzed mathematically to find points on the lightning channel. Thus, "lines" l'_r and $l'_{s'}$ in Figures A4 are not actually straight, although they appear so in these small sections of the images.] There are two interesting facts to note here: (1) Any channel-image vertices that lie on the projection line in one photograph project onto the same line in the other

photograph and are thus indistinguishable. For example, points 152 - 156 on the NRL image all correspond to the projection line, l'_r, shown on the SUNY image of the same flash, which intersects that channel image near the point, $s = 145$, among other places. Close examination of the original photographs suggests channel propagation almost directly toward the SUNY camera in this region. (2) Downward apparent propagation relative to the projection line in one camera image must correspond to downward apparent propagation relative to the corresponding projection line in the other image. Hence, certain channel kinks can be unambiguously identified in both images. For example, the downward loop that is defined by points 162 - 176 in the NRL image corresponds to the downward loop, points 150 - 163, in the SUNY image.

Using these conclusions, we can resolve the apparent ambiguity of the multiple solutions that are indicated by the red [projection lines in Figures A4. Points 152 - 156 on the NRL image correspond to points 145 and 146 in the SUNY image (not to point 149 nor point 164), whereas NRL segment 161 - 162 corresponds to SUNY point 149, and NRL segment 176 - 177 corresponds to SUNY point 164.

Loops of the same sense, such as the pair (NRL 162 - 176 and SUNY 150 - 163) identified above, that could be unambiguously associated between the two images were used as a check on the uncertainties that are inherent in our 3-D channel reconstructions. In most of the flashes the top of the triggering wire was readily identifiable in both photographs. (As mentioned above, the elevation angle of the NRL camera was adjusted -- in each case by less than the 0.5 degree uncertainty in our measurement of that angle -- to make the top of the wire in both images coincide in the reconstruction.) In each of two flashes -- 8717 and 8732 -- there were two obvious kinks, in addition to the top of the wire, that could be used to check the reconstructions. (Figures A4 illustrate one of these four major kinks.) Surprisingly, best agreement was obtained by eliminating the correction for barrel distortion of the 24 mm lens at the SUNY site. In fact, it was found that *all* identifiable kinks in all of the channel images could be made to coincide by this simple parameter change. In retrospect this seems reasonable, since the barrel distortion was measured at close focus, whereas the lens was actually used at infinity focus, where aberrations are usually minimized by design. Therefore, it is presumed that the reconstructions without the barrel-distortion correction are the best possible under the circumstances. (The data in Table A1 correspond to this assumption.)

The significance of eliminating the barrel-distortion correction, and an example of the uncertainty that is inherent in our reconstructions, are illustrated by Figures A5a & A5b, which show two views of reconstructed channel 8732, with (blue) and without (red -- preferred) the correction. Notice that the differences between these two reconstructions are a few tens of meters or less throughout, which is typical. Two views of all six reconstructed channels are given in Figures A6a & A6b. Flashes 8715, 8717, 8725, 8726, 8728, and 8732 are shown in cyan, magenta, blue, green, red, and black, respectively. Notice that there is considerable variability -- much greater than a few tens of meters -- in both the length of the triggering wire and the overall channel shape among these flashes.

In order to illustrate the impact of uncertainties in the reconstructed channels, Figure A7 compares electric-field changes for stroke 2 of flash 8732 that have been calculated from the two different channel reconstructions shown in Figures A5. The shape, amplitude, and propagation speed of the return-stroke current waveform that is deduced for this event in the body of the paper has been used in both cases. Again, the blue curve is with, and the red (preferred) curve is without, the barrel-distortion correction. The differences between these two waveforms are small and are typical of the impact of geometrical uncertainties on the model field changes in our dataset. This satisfying result is a consequence of both the good overall accuracy of the 3-D reconstructions and the considerable smoothing of fine structure that is caused by the rapid increase in current rise time with height, as discussed in the body of the paper.

Appendix B -- Calculation Method for Piecewise-Linear Channel

A numerical code was written in Mathematica [TM], following the general outline of the FORTRAN code that had been developed previously by Le Vine and Meneghini [1978], to compute the electric-field change at the observing site from simulated return strokes in the reconstructed channels. The adoption of the "generalized TLM" form for the stroke current (basically, Equations 5 - 7) allowed a number of simplifications in these calculations. The key attributes of this model are that the entire current waveform propagates monotonically upward along the channel while its principal parameters, $a(s)$, $v(s)$, and $K(t', s)$, depend only on position. Thus, the "pure-TLM" current parameters that are required on each linear channel segment for

Equations 2 - 4 (the fixed current wave shape, $I_{TLM}[argument]$, and constant propagation speed, v) can be computed in advance from knowledge of the channel geometry. Then the field-change calculation can proceed time step by time step.

At each successive time step the current integral on each channel segment is updated for use in Equation 4, and a list of the segments from which radiation can reach the observer is computed. Then the contributions to the total field change are summed, both over Equations 2 - 4 and over all such "radiating" segments. In this way the field-change waveform is built up over time. The size of the time steps is not critical (as long as they are short enough to compute the current integrals with sufficient accuracy), except in the sense that waveform details will be missed if they occur entirely between time steps. As long as the channel segments are made short enough, this calculation method has been shown to accurately approximate the exact field change from a tortuous channel, even when the peak amplitude, rise time, and propagation speed of the current waveform all depend strongly on position. The code has even been shown accurate in the near field by comparison with independent numerical calculations of Jens Schoene [personal communication, 2003] of the University of Florida.

Appendix C -- Analysis of Streak Photographs

Relative light intensity (RLI) determinations from the streak recordings were possible because the data strips were developed with a "calibration strip" of known relative exposure. Each calibration strip was exposed to a single Xenon flash of about 3 us duration, which evenly illuminated a film strip positioned directly behind a Kodak calibration step tablet. The tablet has 21 steps of known density values, thereby transmitting a 1000x range of RLI. With this information, film density can be converted reliably to RLI on a microsecond time scale, as previously demonstrated convincingly by Jordan and Uman [1983].

Here, a Xillix 1412 CCD camera was used to image the data and calibration film strips. The Xillix camera has an image-plane sensor of 1344 x 1035 square pixels and 12-bit output, with a specified dynamic range of >60 dB. Various tests confirmed that a factor of slightly more than a thousand in RLI could be reliably recognized with this device, comparable to the range of the Kodak step tablet and the film emulsion itself. The data and calibration strips were imaged

with the Xillix camera under identical illumination conditions; the Xillix output for known relative exposures on the calibration strip establishes a "lookup table" for values on the data strip, thereby yielding RLI values for the streak image data. Fortunately, the densities for almost all the data and calibration strips were outside the problematic "toe" and "shoulder" portions of the film-response curve, allowing good interpolation accuracy.

All images rendered with the Xillix camera were scanned at 77 pixels per mm on the film, appropriate to having the film grain ultimately limit the analysis. This yields a vertical (spatial) scale of about 0.84 pixels per meter in the object plane and a typical temporal scale of about seven pixels per microsecond for the streak camera.

In this analysis, eight or nine separate vertical levels were first selected for each image, being careful to avoid intense "streak lines" or scratches in the emulsion. Figure 17 for stroke 8725/1 is a typical example. At each pre-selected vertical level, a horizontal strip of 1344x7 pixels centered on that level was then extracted from the digital image and averaged vertically across the seven adjacent pixels (typically about 8 m of channel height) to reduce grain noise. Using the streak camera's known writing rate and the calibration information, the averaged values at each level were converted to a time series of RLI.

The background RLI before the onset of any perceptible leader illumination was estimated separately for the time series of each stroke at each level and used as the zero of RLI for that particular time series. A typical example of the resulting "raw" time series is given in Figure C1, corresponding to level seven (counting upward from the lowest level, always considered level one) of stroke 8725/1. This procedure should allow the RLI to be compared between different levels of the same stroke and also between different strokes in the same flash. (Comparison between strokes in different flashes is potentially somewhat problematic, since they are normally on different pieces of film developed on different days, although in principle the film calibration should permit such a comparison as well.)

To determine the true altitude and the path length along the channel that corresponds to any given level on a streak image, we projected the corresponding three-dimensional channel reconstruction from the perspective of the streak camera and then visually lined up features in the two images. (In many cases it was easier to do this with the leader image when it was visible, since it was often sharper than that of the return stroke.) In this way, for example, level seven of stroke 8725/1 (see Figure 17) was determined to be about 728 m above the surface, or

about 886 m of path length of from the channel base. Interpolation was required on the nearly strait sections of channel where the lightning had followed the triggering wire, of course. (The actual bottom of the channel was obscured by an intervening tree line. Consequently, level one was taken as 30 ± 15 m altitude in each case, based on several lines of evidence.) This procedure allowed the path length corresponding to each level to be determined to an accuracy of ±50 m or better. Based on the average 3-D stroke-propagation speeds estimated in Table 2, this corresponds to a temporal uncertainty of ±0.3 μs or better for these events -- certainly adequate for our purposes.

Determination of the 10 - 90% optical rise time and the peak optical amplitude are related by the choice of onset and peak RLI for the return stroke under consideration. Both determinations were made difficult by the noise on the raw RLI data (*e.g.*, Figure C1, already vertically averaged as indicated above), which became a greater problem as the stroke amplitude decreased. In an effort to minimize this noise without unduly broadening the observed rise time, the data were temporally smoothed by the application of a weighted moving average. The weighting function was a "cosine bell" [*e.g.*, Willett *et al.*, 1990, Equation A8] with an adjustable full width at half maximum (FWHM), normalized to have unity area. It was found experimentally that, as this FWHM was increased for a given time series, the ratio of apparent rise time to FWHM approached 0.80 (when the rise time became dominated by the width of the weighting function). Therefore, FWHM was kept as small as possible, consistent with the unambiguous determination of rise time, and an absolute minimum of 1.6 was imposed on this ratio.

In choosing the onset and peak RLI for each stroke, we focused only on the fast-rising portion of the time series (*e.g.*, about 75.5 to 82.5 μs in Figure C1). This was done both to avoid broadening of the rise time by any light scattering either in the camera or in the film itself and to ignore the gradual rise or "hump" that is often present later in return-stroke light emissions, particularly above the surface (again see Figure C1). In general, these levels were chosen by applying excessive smoothing to find an average "baseline" level just before the onset of the fast-rising portion, and an average peak or plateau just after it, that were reasonably independent of noise spikes. In the case of large, strongly peaked RLI records (typically at measurement levels near the surface for strokes with large peak currents), however, the peak value was allowed to "float" to the maximum of the smoothed waveform as FWHM was varied.

Once the onset and peak RLI were determined, 10% and 90% levels were "drawn" on the smoothed waveform for automatic determination of the last time that the 10% level was exceeded and the first time that the 90% level was exceeded, their difference being the estimated 10 - 90% rise time. The FWHM of the smoothing was then gradually increased from zero until the observed rise time stabilized, but not so much that it became steadily increasing. As FWHM increased, rise time typically passed through a minimum, which was generally taken as the best value, and then slowly increased. Often, however, inconveniently located noise spikes were large enough that they caused abrupt jumps in rise time as increasing smoothing caused them to fall below one or the other RLI threshold. In these cases the determination of rise time became more subjective. Sometimes two or more values of rise time seemed consistent with the data, as illustrated in Figures C2a and C2b, for which the relevant parameters are given in the caption. Fortunately, there was normally a rather small range of deduced rise times in such cases.

The optical peak amplitude of a stroke was taken as the difference between the baseline and peak values determined above. This measurement is also somewhat subjective, the more so as the stroke amplitude decreases toward the noise level.

Acknowledgments

The authors would like to thank W. Jafferis for making the field experiment possible at KSC, C. Leteinturier for making the current data available, S. Heckman for outlining an efficient calculation of channel geometry in Mathematica, J. Schoene for help validating our near-field calculations, and E.P. Krider for valuable consultations and encouragement. The field work was performed while the first author was employed by the Naval Research Laboratory in Washington, DC, with help from J.C. Bailey and R.V. Anderson. The analysis was conceived for, and begun during, a National Research Council senior associateship at the NASA GSFC, was continued while the first author was employed by the Air Force Geophysics Laboratory (sponsored in part by the Air Force Office of Scientific Research), and has been completed under National Science Foundation individual grant, ATM-00004372. Partial support was also provided by NSF grant, ATM-9627276.

1189 References

1190

1191 Berger, K., R. B. Anderson, and H. Kroninger, Parameters of lightning flashes, *Electra, 41*, 23-
1192 37, 1975.

1193

1194 Boas, M.L., Mathematical Methods in the Physical Sciences, John Wiley & Sons, New York,
1195 778pp, 1966.

1196

1197 Bruce, C.E.R., and R.H. Golde, The lightning discharge, *J. Inst. Electr. Eng. (London), 88*, 487-
1198 520, 1941.

1199

1200 Christian, H.J., V. Mazur, B.D. Fisher, L.H. Ruhnke, K. Crouch, and R.P. Perala, The
1201 Atlas/Centaur lightning strike incident, *J. Geophys. Res., 94*, 13,169-13,177, 1989.

1202

1203 Cooray, V., and R.E. Orville, The effects of variation of current amplitude, current rise time, and
1204 return stroke velocity along the return stroke channel on the electromagnetic fields generated by
1205 return strokes, *J. Geophys. Res., 95*, 18,617-18,630, 1990.

1206

1207 Colvin, J.D., C.K. Mitchell, J.R. Greig, D.P. Murphy, R.E. Pechacek, and M. Raleigh, An
1208 empirical study of the nuclear explosion-induced lightning seen on IVY-MIKE, *J. Geophys.*
1209 *Res., 92*, 5696--5712, 1987.

1210

1211 Cooray, V., and R.E. Orville, The effects of variation of current amplitude, current rise time, and
1212 return stroke velocity along the return stroke channel on the electromagnetic fields generated by
1213 return strokes, *J. Geophys. Res., 95*, 18,617-18,630, 1990.

1214

1215 Crawford, D.E., Multiple-station measurements of triggered lightning electric and magnetic
1216 fields, Masters thesis, Univ. of Fla., Gainesville, 1998.

1217

1218 Depasse, P., Statistics on artificially triggered lightning, *J. Geophys. Res., 99,* 18,515–18,522,
1219 1994.

Diendorfer, G., and M.A. Uman, An improved return stroke model with specified channel-base current, *J. Geophys. Res., 95,* 13,621-13,644, 1990.

Eriksson, A. J., Lightning and tall structures, *Trans. S. Afr. Inst. Electr. Eng.*, *69*, 2-16, 1978.

Fisher, R. J., G. H. Schnetzer, R. Thottappillil, V. A. Rakov, M. A. Uman, and J. D. Goldberg, Parameters of triggered-lightning flashes in Florida and Alabama, *J. Geophys. Res.*, *98*, 22,887-22,902, 1993.

Garbagnati, E., and G.B. Lo Pipero, Parameter von Blitzstromen, *Electrotech. Z., 103*, 61-65, 1982.

Gomes, C., and V. Cooray, Correlation between the optical signatures and current wave forms of long sparks: applications in lightning research, *J. Electrostatics, 43*, 267-274, 1998.

Guo, C., and E.P. Krider, The optical and radiation field signatures produced by lightning return strokes, *J. Geophys. Res., 87,* 8913-8922, 1982.

Guo, C., and E.P. Krider, Anomalous light output from lightning dart leaders, *J. Geophys. Res., 90,* 13,073-13,075, 1985.

Hallert, B., Photogrammetry: *Basic Principles and General Survey*, McGraw-Hill Book Company, Inc., New York, 1960, 340 pp.

Heidler, F., Traveling current source model for LEMP calculation, in *Proc. 6th Int. Zurich Symp. Electromagn. Compat.*, pp. 157-162, Zurich, Mar. 1985.

Hill, R.D., Electromagnetic radiation from erratic paths of lightning strokes, *J. Geophys. Res., 74*, 1922-1929, 1969.

1251 Hubert, P., A new model of lightning subsequent stroke -- confrontation with triggered lightning
1252 observations, in *Tenth International Aerospace and Ground Conference on Lightning and Static*
1253 *Electricity (ICOLSE)*, pp. 211-215, Paris, June 10-13, 1985.
1254
1255 Idone, V.P., and R.E. Orville, Lightning return stroke velocities in the thunderstorm research
1256 international program (TRIP), *J. Geophys. Res., 87*, 6555-6562, 1982.
1257
1258 Idone, V.P., R.E. Orville, P. Hubert, L. Barret, and A Eybert-Berard, Correlated observations of
1259 three triggered lightning flashes, *J. Geophys. Res., 89*, 1385-1394, 1984.
1260
1261 Idone, V.P., and R.E. Orville, Correlated peak relative light intensity and peak current in
1262 triggered lightning subsequent return strokes, *J. Geophys. Res., 90*, 6159-6164, 1985.
1263
1264 Jordan, D., and M.A. Uman, Variations in light intensity with height and time from subsequent
1265 return strokes, *J. Geophys. Res., 88*, 4903-4915, 1983.
1266
1267 Jordan, D., V.A. Rakov, W.H. Beasley, and M.A. Uman, Luminosity characteristics of dart
1268 leaders and return strokes in natural lightning, *J. Geophys. Res., 102*, 22,025-22,032, 1997.
1269
1270 Kodali, V., V.A. Rakov, M.A. Uman, K.J. Rambo, G.H. Schnetzer, J. Schoene, and J. Jerauld,
1271 Triggered-lighting properties inferred from measured currents and very close electric fields,
1272 *Atmos. Res., 76*, 355-376, 2005.
1273
1274 Leteinturier, C., C. Weidman, and J. Hamelin, Current and electric field derivatives in triggered
1275 lightning return strokes, *J. Geophys. Res., 95*, 811-828, 1990.
1276
1277 Leteinturier, C., and J. Hamelin, Submicrosecond characteristics of lightning return-stroke
1278 currents, *IEEE Trans. EMC, 33*, 351-357, 1991.
1279
1280 Le Vine, D.M., and R. Meneghini, Simulation of radiation from lightning return strokes: The
1281 effects of tortuosity, *Radio Sci., 13*, 801-809, 1978.

Le Vine, D.M. and R. Meneghini, A solution for the electromagnetic fields close to a lightning discharge, in *International Aerospace and Ground Conference on Lightning and Static Electricity (ICOLSE)*, pp. 70-1 - 70-10, Fort Worth, Texas, June, 1983.

Le Vine, D.M., and M. Kao, The effects of current risetime on radiation from tortuous lightning channels, Proceedings 8th International Conference on Atmospheric Electricity, Uppsala, Sweden, 509-514, 1988.

Le Vine, D.M., J.C. Willett, and J.C. Bailey, Comparison of fast electric field changes from subsequent return strokes of natural and triggered lightning, *J. Geophys. Res.*, *94*, 13,259-13,265, 1989.

Le Vine, D.M., and J.C. Willett, Comment on the transmission-line model for computing radiation from lightning, *J. Geophys. Res., 97*, 2601-2610, 1992.

Le Vine, D.M., and J.C. Willett, The influence of channel geometry on the fine scale structure of radiation from lightning return strokes, *J. Geophys. Res.*, *100*, 18,629-18,638, 1995.

Lin, Y.T., M.A. Uman, and R.B. Standler, Lightning return stroke models, *J. Geophys. Res.*, *85*, 1571-1583, 1980.

Mach, D.M., and W.D. Rust, Photoelectric return-stroke velocity and peak current estimates in natural and triggered lightning, *J. Geophys. Res., 94*, 13,237-13,247, 1989.

Mach, D.M., and W.D. Rust, Two-dimensional speed and optical risetime estimates for natural and triggered dart leaders, *J. Geophys. Res., 102*, 13,673-13,684, 1997.

Master, M.J., M.A. Uman, Y.T. Lin, and R.B. Standler, Calculations of lightning return stroke electric and magnetic fields above ground, *J. Geophys. Res., 86*, 12,127-12,132, 1981.

1313 Mattos, M.A. da F., and C. Christopoulos, A nonlinear transmission line model of the lightning
1314 return stroke, *J. Phys. D, Appl. Phys., 23*, 40-46, 1990.
1315
1316 Mazur, V., B.D. Fisher, and J.C. Gerlach, Lightning strikes to an airplane in a thunderstorm, *J.*
1317 *Aircraft, 21*, 607-611, 1984.
1318
1319 Mazur, V., B.D. Fisher, and P.W. Brown, Multistroke cloud-to-ground strike to the NASA F-
1320 106B airplane, *J. Geophys. Res., 95*, 5471-5484, 1990.
1321
1322 Mazur, V., and J.-P. Moreau, Aircraft-triggered lightning: processes following strike initiation
1323 that affect aircraft, *J. Aircraft, 29*, 575-580, 1992.
1324
1325 Murphy, D.P., J.R. Greig, R.E. Pechacek, M. Raleigh, E. Laikin, and S. Hauver, Nuclear
1326 explosion induced lightning: a laboratory simulation, NRL Memo. Rept. 5688, US Naval
1327 Research Laboratory, Washington, DC, February 4, 1986.
1328
1329 Nucci, C.A., G. Diendorfer, M.A. Uman, F. Rachidi, M. Ianoz, and C. Mazzetti, Lightning return
1330 stroke models, *J. Geophys. Res.*, *95*, 20,395-20,408, 1990.
1331
1332 Olsen, R.C., III, D.M. Jordan, V.A. Rakov, M.A. Uman, and N. Grimes, Observed on-
1333 dimensional return stroke propagation speeds in the bottom 170 m of a rocket-triggered lightning
1334 channel, *Geophys. Res. Lett., 31*, L16107, doi:10.1029/2004GL020187, 2004.
1335
1336 Rakov, V.A., and M.A. Uman, Review and evaluation of lightning return stroke models
1337 including some aspects of their application, *IEEE Trans. EMC, 40*, 403-426, 1998.
1338
1339 Rakov, V.A., M.A. Uman, K.J Rambo, M.I. Fernandez, R.J. Fisher, G.H. Schnetzer, R.
1340 Thottappillil, A. Eybert-Berard, J.P. Berlandis, P. Lalande, A. Bonamy, P. Laroche, and A.
1341 Bondiouu-Clergerie, New insights into lightning processes gained from triggered-lightning
1342 experiments in Florida and Alabama, *J. Geophys. Res.*, *103*, 14,117-14,130, 1998.
1343

1344 Reazer, J.S., A.V. Serrano, L.C. Walco, and H.D. Burket, Analysis of correlated electromagnetic
1345 fields and current pulses during airborne lightning attachments, *Electromagnetics, 7*, 509-539,
1346 1987.
1347
1348 Schoene, J., M.A. Uman, V.A. Rakov, V. Kodali, K.J Rambo, and G.H. Schnetzer, Statistical
1349 characteristics of the electric and magnetic fields and their time derivatives 15 m and 30 m from
1350 triggered lightning, *J. Geophys. Res., 108*, 4192, doi:10.1029/2002JD002698, 2003.
1351
1352 Schonland, B.F.J., D.J. Malan, and H. Collens, Progressive lightning, 2, *Proc. Roy. Soc. London,*
1353 *Ser. A, 152*, 595-625, 1935.
1354
1355 Strawe, D.F., Non-linear modeling of lightning return strokes, in *Proc. Fed. Aviat.*
1356 *Administra./Florida Inst. Technol. Workshop Grounding Lightning Technol.*, FAA-RD-79-6, pp. 9-
1357 15, Melbourne, FL, March, 1979.
1358
1359 Thottappillil, R. and M.A. Uman, Comparison of lightning return-stroke models, *J. Geophys.*
1360 *Res., 98*, 22,903-22,914, 1993.
1361
1362 Uman, M.A., and D.K. McLain, Lightning return stroke current from magnetic and radiation
1363 field measurements, *J. Geophys. Res., 75*, 5143-5147, 1970.
1364
1365 Uman, M.A., *The Lightning Discharge*, Academic Press, Inc., Orlando, 377pp., 1987.
1366
1367 Uman, M.A., Natural and artificially-initiated lightning and lightning test standards, *Proc. IEEE,*
1368 *76*, 1548-1565, 1988.
1369
1370 Uman, M.A., V.A. Rakov, G.H. Schnetzer, K.J. Rambo, D.E. Crawford, and R.G. Fisher, Time
1371 derivative of the electric field 10, 14, and 30 m from triggered lightning strokes, *J. Geophys.*
1372 *Res., 105*, 15,577-15,595, 2000.
1373

1374 Vecchi, G., D. Labate, and F. Canavero, Fractal approach to lightning radiation on a tortuous
1375 channel, *Radio Sci., 29*, 691-704, 1994.
1376
1377 Wang, D., N. Takagi, T. Watanabe, V.A. Rakov, M.A. Uman, K.J. Rambo, and M.V. Stapleton,
1378 A comparison of channel-base currents and optical signals for rocket-triggered lightning strokes,
1379 *J. Geophys. Res., 104*, 2143-2150, 1999.
1380
1381 Wang, D., V.A. Rakov, M.A. Uman, N. Takagi, T. Watanabe, D.E. Crawford, K.J. Rambo, G.H.
1382 Schnetzer, R.G. Fisher, and Z.-I. Kawasaki, Attachment process in rocket-triggered lightning
1383 strokes, *Atmos. Res., 76*, 412-422, 2005.
1384
1385 Willett, J.C., J.C. Bailey, V.P Idone, A. Eybert-Berard, and L. Barret, Submicrosecond
1386 intercomparison of radiation fields and currents in triggered lightning return strokes based on the
1387 transmission-line model, *J. Geophys. Res., 94*, 13,275-13,286, 1989.
1388
1389 Willett, J.C., J.C. Bailey, C. Leteinturier, and E.P. Krider, Lightning electromagnetic radiation
1390 field spectra in the interval from 0.2 to 20 MHz, *J. Geophys. Res., 95*, 20,367-20,387, 1990.
1391
1392 Willett, J.C., D.M. Le Vine, M. Kao, and V.P. Idone, Calculated and observed electric fields of
1393 rocket-triggered-lightning return strokes with known channel geometries, *EOS, 70*, 1015, 1989
1394 (presented at the Fall Annual Meeting of the American Geophysical Union, San Francisco, CA,
1395 December).
1396
1397 Willett, J.C., D.M. Le Vine, and V.P. Idone, Lightning-channel morphology revealed by
1398 return-stroke radiation-field waveforms, *J. Geophys. Res., 100*, 2727-2738, 1995.
1399
1400 Willett, J.C., and D.M. Le Vine, 3-D channel reconstruction for triggered lightning return
1401 strokes, *EOS, 76*, Supplement, p.F118, 1995 (presented at the Fall Annual Meeting of the
1402 American Geophysical Union, San Francisco, CA, December).
1403

Willett, J.C., and D.M. Le Vine, On the current distribution in lightning subsequent return strokes, in *Proceedings, 10th International Conference on Atmospheric Electricity*, Osaka, Japan, 10-14 June 1966, International Commission on Atmospheric Electricity, pp. 492-495 (printed but not presented because of insufficient travel funds), 1996.

Willett, J.C., and D.M. Le Vine, Lightning return-stroke current waveforms aloft, from measured field change, current, and channel geometry, presented at the Fall Annual Meeting of the American Geophysical Union, San Francisco, CA, December, 2002.

Willett, J.C., and D.M. Le Vine, Lightning return-stroke current waveforms aloft, from measured field change, current, and channel geometry, in Proceedings, *12th International Conference on Atmospheric Electricity*, Versailles, France, 9-13 June, International Commission on Atmospheric Electricity, 2003.

Figure Captions

Figure 1 -- An example of our "convolution smoothing" of the measured current waveform (black curve) to produce different wave shapes, $I(t_1,s)$ in Equation 7, at different heights. The corresponding values of kernel time scale, $\tau(s)$, and 10 - 90% rise time are tabulated in the figure.

Figure 2 -- Two examples of truncated, smoothed, and extrapolated channel-base-current waveforms. (a) Full 15 μs time series, illustrating extrapolations. (b) First 1 μs, illustrating onset truncation and noise smoothing.

Figure 3 -- Measured field change for stroke 8732/2 (black) compared to that calculated when the measured current waveform propagates at a constant speed of 1.71×10^8 m/s without changing either shape or amplitude (green).

Figure 4 -- Similar to Figure 3, but this time convolution smoothing ($\tau_{max} = 4.36$ μs, $L_\tau = 7084$ m) is included to produce the green curve and then decreasing TLM velocity ($v_{min} = 2.1 \times 10^8$ m/s, $v_{max} = 2.6 \times 10^8$, $L_{v1} = 500$ m) is added to produce the red curve.

Figure 5 -- TLM-velocity profiles [$v(s)$, solid curves] and current-front effective-velocity profiles [$v_{eff}(s)$, dots] for the two calculations shown in Figure 4 (colors correspond).

Figure 6 -- Similar to Figure 4 except that the red curve has been further modified by a decreasing amplitude factor ($a_{min1} = 0.7$, $L_{a1} = 60$ m, $a_{min2} = 0.6$, $L_{a2} = 400$ m).

Figure 7 -- Profile of the amplitude factor [$a(s)$, red curve] and the corresponding relative profile of charge deposition on the channel by the model return stroke shown in Figure 6 (green).

Figure 8 -- TLM- and front-velocity profiles, as in Figure 5, for stroke 8732/1, which required propagation-speed adjustment, as well as amplitude adjustment, in order to match both the peak and the subsequent structure of $E_m(t)$. The solid green curve is for v_{min} = 2.0 X 10^8 m/s, v_{max} = 2.3 X 10^8, and L_{v1} = 500 m. The red curve adds the paremeters, v_{ampl} = 0.7 X 10^8 m/s and L_{v2} = 60 m.

Figure 9 -- Computed field-change waveforms (colors) corresponding to the velocity profiles in Figure 8 are compared with observed field change (black).

Figure 10 -- TLM-velocity (solid) and front-velocity (dots) profiles for stroke 8728/11. The parameters for the solid curve are v_{min} = 2.7 X 10^8 m/s, v_{max} = 3.0 X 10^8, and L_{v1} = 500 m.

Figure 11 -- The effect of a very rapid amplitude-factor decrease in a case with the parameters, τ_{max} = 1.16 μs, L_τ = 1851 m, v_{min} = 2.3 X 10^8 m/s, v_{max} = 3.0 X 10^8, L_{v1} = 500 m, and as given in the caption of Figure 12.

Figure 12 -- Similar to Figure 7 but shown on an expanded height scale for the parameters, a_{min1} = 0.69, L_{a1} = 5 m, a_{min2} = 0.35, L_{a2} = 1000 m, that correspond to the red curve in Figure 11.

Figure 13 -- Two different current-waveform extrapolations for stroke 8725/4.

Figure 14 -- Model field-change waveforms (green and red, corresponding to the similarly colored current waveforms in Figure 13) are compared with the observed field change (black).

Figure 15 -- Observed (black) and modeled (red) field-change waveforms for all 24 return strokes in our data set. (a) collects the events from three flashes for which we could analyze only two strokes each. (b), (c), and (d) each show several strokes from a single flash. The scales are V/m versus μs.

Figure 16 -- Measured and extrapolated current waveforms corresponding to the field-change waveforms of Figure 15. The scales are kA versus μs.

Figure 17 -- A typical streak image of leader/return-stroke sequence for stroke 8725/1 is shown as rendered by the Xillix camera. The analysis levels chosen for this event are illustrated by white horizontal bars. The vertical separation between level one (the lowest) and level nine (the highest) in this image corresponds to about 980 m at the range of the lightning channel. The horizontal extent of the image corresponds to about 125 μs of time. See Appendix C for further details.

Figure 18 -- Comparison of optical and electrical results as a function of path length. The left-hand panels show peak-relative-light-intensity and peak-current profiles, while the right-hand panels show 10 - 90% rise-time profiles of RLI and of current. Each flash has its own row of two panels showing all strokes for which both optical data and electrical inferences are available in that flash. Optical results are plotted with solid symbols and lines, whereas electrical results have hollow symbols connected by dashed lines.

Figure 19 -- Similar to Figure 17 but for stroke 8725/3, which has an especially bright leader.

Figure A1 -- Still-camera images of flash 8732 from the NRL site (a), located about 5.2 km east of the triggering site and using a 55 mm lens, and from the SUNY site (b), located about 2.2 km SSE of the triggering site and using a 24 mm lens.

Figure A2 -- Camera locations and orientations at the NRL (subscript N) and SUNY (subscript S) sites relative to the triggering site -- the origin, O, of the (x, y, z) coordinate system. (a) D_i and h_i represent the relative ranges and heights of the two cameras. The NRL site is taken to be just above the x-axis. Angle α_P represents the co-azimuth of the SUNY site. (b) The definition of the camera-azimuth angle at the SUNY site, γ_S. (c) The (simplified -- see text) definition of the camera-elevation angle at the NRL site, α_N.

Figure A3 -- A heuristic illustration of the channel-reconstruction method used in this paper. The locations of the two cameras are indicated by P_1 (representing NRL) and P_2 (representing SUNY, except for a change in the sign of α_P for convenience of illustration), with the other parameters as in Figure A2a. Point r on the channel in the first idealized image defines the ray, $\boldsymbol{l}_r$, which projects onto the second image as the line, l'_r. This line intersects that imaged channel at point, s', which in turn defines a second ray, $\boldsymbol{l}_{s'}$, and a point on the 3-D channel, identified as (r, s') -- see text.

Figure A4 -- Magnified portions of idealized images from the NRL (a) and SUNY (b) cameras, showing a major channel kink, leading to multiple solutions. The graph axes give the absolute elevation and azimuth angles, (θ_i, φ_i), in radians. Digitized points on the two images are numbered consecutively from the channel base upward. The "lines", l'_r and l'_s, where the "solution plane" corresponding to point $r = 155$ on the NRL image cuts both images are indicated in red. See text for interpretation.

Figure A5 -- Two views of the 3-D reconstructed channel for flash 8732, with (blue) and without (red) the barrel-distortion correction to the SUNY lens. The scales of the (x, y, z) axes are in meters relative to the location of the triggering site.

Figure A6 -- The same two views as in Figure 5, but showing all six reconstructed flashes used in this study.

Figure A7 -- Electric-field changes computed for stroke 8732/2 using the current model inferred in this paper (see the section, "Detailed Example of Fitting Procedure") together with the two channel reconstructions shown in Figure A5. The blue curve uses the barrel-distortion correction, whereas the red curve does not.

Figure C1 -- "Raw" relative light intensity, after averaging seven pixels vertically and after zero subtraction but before any temporal smoothing, at level seven of stroke 8725/1 (see Figure 17).

Figure C2 -- Similar to Figure C1, except that temporal smoothing has been added, the "baseline" and peak magnitudes of the fast-rising portion of the return-stroke RLI have been indicated in blue, and the corresponding 10 - 90% levels have been shown in green. (a) The "cosine-bell" smoothing comprises 13 horizontal pixels of the streak image in this case, for a FWHM of 0.81 μs, yielding a 10 - 90% rise time of 3.51 μs. (b) Here the smoothing comprises 27 pixels, FWHM = 1.78 μs, and 10 - 90% rise time is 3.78 μs. "Baseline" and peak RLI are 0.185 and 1.010, respectively, in both cases.

Table 1 -- Free Parameters in Current Model

Event	Geometry		Kernel Scale, $\tau(s)$			TLM Velocity, $v(s)$						Ampl. Factor, $a(s)$				Onset
	Wire Tip	Chnl. Top	τ_{max}	L_τ	Initial Slope	v_{min}	v_{max}	L_{v1}	v_{ampl}	L_{v2}	Const. Slope	a_{min1}	L_{a1}	a_{min2}	L_{a2}	@Chnl. Top
(Flsh/ Stroke)	(m)	(m)	(μs)	(m)	(μs/km)	(10^8 m/s)	(10^8 m/s)	(m)	(10^8 m/s)	(m)	(m/s/m)		(m)		(m)	(μs)
8715/2	184	1240			0.817	2.50	3.00	150	0.00			0.65	100	1.00		5.91
8715/3	184	1240			0.653	2.50	3.00	150	0.00			0.78	50	0.80	200	5.91
8715/4	184	1240			0.653	2.50	3.00	150	0.00			0.80	20	0.77	200	5.91
8715/6	184	1240			1.037	3.00			0.00			0.80	30	0.79	150	5.19
8715/7	184	1240			0.653	3.00			0.00			0.75	5	0.74	75	5.19
8715/8	184	1240			0.817	2.75	3.00	75	0.00			0.77	20	0.55	1000	5.55
8715/9	184	1240			0.817	3.00			0.00			0.59	35	1.00		5.19
8715/10	184	1240			0.653	2.50	3.00	150	0.00			0.73	5	0.85	200	5.91
8717/3	269	2220			0.935	2.10	2.60	70	0.40	700		0.45	130	1.00		10.94
8717/5	269	2220			0.935	2.10	2.60	70	0.40	700		0.55	130	1.00		10.94
8725/1	370	1842	0.663	782	0.848	2.20	3.00	400	0.00			0.69	40	0.52	400	8.73
8725/2	370	1842	0.663	782	0.848	2.20	3.00	400	0.00			0.81	5	0.52	200	8.73
8725/3	370	1842	0.663	782	0.848	2.10	3.00	400	0.00			0.58	10	0.64	500	9.01
8725/4	370	1842	1.691	845	2.001	0.75	2.15	100	0.85	800		0.50	150	1.00		18.09
8725/5	370	1842			0.682	2.30	2.70	100	0.00			0.70	5	0.50	500	8.85
8726/1	552	1704			0.236		3.00				-100000	0.46	10	0.90	300	8.97
8726/2	552	1704	1.160	1851	0.627	1.80	2.60	30	0.40	500		0.80	30	0.50	400	9.48
8726/3	552	1704	1.160	1851	0.627	2.30	3.00	500	0.00			0.69	5	0.35	1000	7.43
8726/4	552	1704	1.160	1851	0.627	1.80	2.60	30	0.40	500		0.80	30	0.50	400	9.46
8726/5	552	1704	1.160	1851	0.627	2.40	3.00	300	0.00			0.67	10	0.45	1000	7.40
8728/10	171	1754	0.792	814	0.973	2.70	3.00	500	0.00			0.68	70	0.65	500	8.13
8728/11	171	1754	0.727	531	1.369	2.70	3.00	500	0.00			0.75	100	0.50	400	8.13
8732/1	197	1844			0.458	2.00	2.70	60	0.30	500		0.70	80	0.64	300	9.75
8732/2	197	1844	4.360	7084	0.615	2.10	2.60	500	0.00			0.70	60	0.60	400	9.22

Table 2 -- Representative Values of Current Behavior

Event	10-90% Rise Time of Current						Front Velocity, $v_{eff}(s)$					Amplitude Factor, $a(s)$				
	Sfc.	10m	30m	100m	300m	1000m	Ave.	10m	100m	300m	1000m	10m	30m	100m	300m	1000m
(Flsh/ Stroke)	(μs)	(μs)	(μs)	(μs)	(μs)	(μs)	(10^8 m/s)	(10^8 m/s)	(10^8 m/s)	(10^8 m/s)	(10^8 m/s)					
8715/2	0.296	0.300	0.327	0.470	0.951	2.50	1.72	1.60	1.70	1.72	1.75	0.97	0.91	0.78	0.67	0.65
8715/3	0.179	0.180	0.196	0.329	0.764	1.99	1.85	1.90	1.85	1.82	1.85	0.95	0.88	0.75	0.66	0.63
8715/4	0.189	0.191	0.215	0.344	0.729	2.17	1.84	1.88	1.83	1.83	1.82	0.91	0.82	0.73	0.66	0.62
8715/6	0.175	0.183	0.228	0.436	1.050	3.39	1.74	1.52	1.70	1.75		0.93	0.84	0.72	0.65	0.63
8715/7	0.186	0.190	0.213	0.353	0.759	2.22	2.04	1.90	1.93	2.05	2.08	0.76	0.69	0.61	0.56	0.56
8715/8	0.191	0.193	0.215	0.360	0.794	2.58	1.84	1.70	1.78	1.83	1.86	0.91	0.81	0.74	0.68	0.55
8715/9	0.356	0.358	0.375	0.501	0.991	2.81	1.87	1.68	1.75	1.87		0.90	0.76	0.61	0.59	0.59
8715/10	0.270	0.268	0.275	0.375	0.757	2.12	1.84	1.88	1.82	1.83	1.84	0.76	0.72	0.69	0.64	0.62
8717/3	0.138	0.136	0.163	0.377	0.898	2.57	1.60	1.70	1.61	1.60	1.58	0.96	0.89	0.70	0.50	0.45
8717/5	0.111	0.116	0.152	0.335	0.854	2.57	1.60	1.65	1.65	1.62	1.55	0.97	0.91	0.76	0.59	0.55
8725/1	0.553	0.544	0.536	0.609	0.964	1.83	1.95	1.70	1.74	1.86	2.02	0.92	0.81	0.64	0.52	0.39
8725/2	0.433	0.432	0.437	0.550	0.969	1.76	1.95	1.63	1.72	1.83	2.00	0.82	0.76	0.66	0.51	0.42
8725/3	0.355	0.357	0.369	0.481	0.879	1.80	1.90	1.68	1.74	1.83	1.93	0.73	0.59	0.54	0.49	0.40
8725/4	0.162	0.171	0.249	0.541	1.400	3.09	0.93	1.11	1.20	1.01	0.90	0.97	0.92	0.75	0.45	0.45
8725/5	0.159	0.161	0.175	0.297	0.700	2.02	1.74	1.70	1.71	1.71	1.73	0.73	0.68	0.64	0.54	0.40
8726/1	0.888	0.875	0.871	0.871	0.944	1.54	1.84	2.76	2.36	2.21	1.76	0.66	0.48	0.45	0.43	0.42
8726/2	0.491	0.494	0.514	0.586	0.831	1.71	1.62	1.83	1.62	1.61	1.61	0.93	0.84	0.72	0.59	0.43
8726/3	0.269	0.266	0.268	0.358	0.720	1.91	1.96	1.90	1.92	1.97	1.97	0.73	0.68	0.65	0.57	0.41
8726/4	0.339	0.340	0.349	0.421	0.705	1.61	1.62	1.88	1.62	1.60	1.60	0.93	0.84	0.72	0.59	0.43
8726/5	0.323	0.322	0.316	0.412	0.828	2.09	1.93	1.90	1.91	1.90	1.95	0.79	0.68	0.63	0.57	0.44
8728/10	0.400	0.402	0.416	0.579	1.050	2.23	2.14	1.55	1.70	1.88	2.28	0.95	0.87	0.71	0.58	0.47
8728/11	0.216	0.223	0.273	0.522	1.120	2.15	2.18	1.30	1.60	1.87	2.41	0.96	0.90	0.75	0.56	0.41
8732/1	0.410	0.410	0.416	0.448	0.682	1.57	1.72	2.17	1.80	1.70	1.70	0.95	0.88	0.71	0.55	0.46
8732/2	0.408	0.408	0.413	0.494	0.870	2.09	1.71	1.70	1.71	1.72	1.71	0.94	0.86	0.69	0.55	0.44

Table 3 -- Optical Parameters from Streak Photographs

Event	Level	Reconstructed		RLI		Rise Time	
		Height	Path	Baseline	Amplitude	10-90%	Error
(Flsh/ Stroke)		(m)	(m)			(μs)	(μs ±)
8715/9	1	30	30	0.0	3.6	1.3	0.07
8715/9	2	144	144	0.8	1.5	0.9	0.07
8715/9	3	274	299	0.5	1.5	1.3	0.07
8715/9	4	407	480	0.9	2.2	1.7	0.14
8715/9	5	488	597	0.6	1.5	1.1	
8715/9	6	675	864	0.4	1.6	4.2	0.21
8715/9	7	787	983	0.5	1.8	2.7	0.49
8715/9	8	919	1128	0.5	1.6	2.6	0.48
8715/9	9	1021	1240	0.5	1.5	4.0	0.77
8715/10	1	30	30	0.1	2.3	2.0	
8715/10	2	144	144	0.1	1.4	1.7	
8715/10	3	274	299	0.0	1.2	2.8	0.07
8715/10	4	407	480	0.3	0.8	2.6	
8715/10	5	488	597	0.1	0.9	4.7	
8715/10	6	675	864	0.0	0.8	4.6	
8715/10	7	787	983	0.1	0.6	3.8	
8715/10	8	919	1128	-0.1	0.6	4.9	
8715/10	9	1021	1240	0.0	0.5	5.7	0.84
8725/1	1	30	30	0.0	1.8	1.6	
8725/1	2	149	150	0.1	1.1	2.3	
8725/1	3	267	269	0.2	0.9	1.8	
8725/1	4	394	409	0.3	0.9	2.8	
8725/1	5	515	580	0.2	0.8	1.4	
8725/1	6	603	734	0.2	0.7	3.4	
8725/1	7	728	886	0.2	0.8	3.7	0.13
8725/1	8	858	1077	0.2	0.5	3.0	0.06
8725/1	9	1011	1280	0.0	0.6	5.7	0.20
8725/2	1	30	30	0.0	1.5	0.8	
8725/2	2	149	150	0.2	0.7	1.8	
8725/2	3	267	269	0.1	0.7	2.2	
8725/2	4	394	409	0.2	0.7	2.0	
8725/2	5	515	580	0.1	0.7	4.2	
8725/2	6	603	734	0.1	0.6	3.1	0.14
8725/2	7	728	886	0.1	0.4	2.0	0.50
8725/2	8	858	1077	0.0	0.5	5.5	0.41
8725/2	9	1011	1280	0.1	0.4	5.3	0.07
8725/3	1	30	30	0.2	3.1	1.2	
8725/3	2	149	150	1.1	2.2	1.2	

8725/3	3	267	269	1.0	2.1	1.2	
8725/3	4	394	409	1.0	1.4	1.2	
8725/3	5	515	580	1.2	1.4	1.9	
8725/3	6	603	734	0.9	1.6	2.8	
8725/3	7	728	886	1.0	1.3	3.0	
8725/3	8	858	1077	0.7	1.5	4.2	
8725/3	9	1011	1280	0.5	1.3	4.5	
8725/5	1	30	30	0.0	0.6	1.2	
8725/5	2	149	150	0.0	0.4	2.4	
8725/5	3	267	269	0.0	0.3	1.2	
8725/5	4	394	409	0.0	0.3	3.5	
8725/5	5	515	580	0.0	0.3	6.3	1.42
8725/5	6	603	734	0.1	0.2	4.7	0.54
8725/5	7	728	886	0.0	0.2	5.8	0.55
8725/5	8	858	1077	0.1	0.2	3.9	0.54
8725/5	9	1011	1280	0.0	0.2	7.2	0.88
8726/1	1	30	30	0.1	2.6	0.9	
8726/1	2	151	151	0.8	2.2	1.4	
8726/1	3	269	270	0.7	1.8	1.6	
8726/1	4	388	390	0.5	1.7	2.0	
8726/1	5	510	513	0.5	1.6	2.3	
8726/1	6	627	642	0.7	1.6	1.6	0.34
8726/1	7	817	951	0.6	1.6	3.0	
8726/1	8	969	1167	0.7	1.5	2.1	0.21
8726/1	9	1098	1321	0.4	1.2	4.9	0.34
8726/2	1	30	30	0.2	3.0	0.9	
8726/2	2	151	151	0.0	1.0	1.4	
8726/2	3	269	270	0.1	1.0	2.2	0.07
8726/2	4	388	390	0.0	0.8	2.1	0.07
8726/2	5	510	513	-0.1	0.6	1.6	
8726/2	6	627	642	0.0	0.6	2.0	
8726/2	7	817	951	0.0	0.7	2.6	
8726/2	8	969	1167	0.1	0.5	4.5	0.68
8726/2	9	1098	1321	0.0	0.5	6.0	0.68
8726/3	1	30	30	0.0	1.0	1.3	0.07
8726/3	2	151	151	0.0	0.5	1.7	0.07
8726/3	3	269	270	0.1	0.5	2.4	0.07
8726/3	4	388	390	0.0	0.4	3.6	
8726/3	5	510	513	0.1	0.4	3.0	
8726/3	6	627	642	0.1	0.3	3.4	
8726/3	7	817	951	0.0	0.3	4.7	0.14
8726/3	8	969	1167	0.1	0.3	5.1	0.27
8726/3	9	1098	1321	0.0	0.2	6.8	0.07
8726/4	1	30	30	0.0	1.5	1.0	0.14

8726/4	2	151	151	0.0	0.9	1.4	
8726/4	3	269	270	0.0	0.6	1.4	
8726/4	4	388	390	0.0	0.5	1.4	0.14
8726/4	5	510	513	0.0	0.4	1.9	
8726/4	6	627	642	0.0	0.4	2.0	0.06
8726/4	7	817	951	0.0	0.4	2.8	0.07
8726/4	8	969	1167	0.0	0.3	4.6	0.13
8726/4	9	1098	1321	0.0	0.1	2.2	0.07
8728/10	1	30	30	0.1	3.2	1.5	
8728/10	2	139	139	0.6	2.0	1.3	
8728/10	3	253	273	0.5	1.9	1.9	
8728/10	4	394	472	0.3	1.5	2.3	
8728/10	5	526	665	0.5	1.3	2.7	
8728/10	6	643	851	0.6	1.4	3.1	
8728/10	7	738	1136	0.5	1.3	4.2	
8728/10	8	814	1273	0.2	0.7	4.0	0.40
8728/11	1	30	30	0.1	1.8	1.6	
8728/11	2	139	139	0.2	1.0	1.9	
8728/11	3	253	273	0.1	1.1	1.9	
8728/11	4	394	472	0.1	1.0	2.0	
8728/11	5	526	665	0.1	0.8	2.9	0.07
8728/11	6	643	851	0.2	0.7	3.9	
8728/11	7	738	1136	0.0	0.7	4.4	
8728/11	8	814	1273	0.0	0.3	4.8	0.14
8732/1	1	30	30	0.2	2.2	0.9	0.07
8732/1	2	150	150	0.1	1.6	0.9	0.07
8732/1	3	269	295	0.3	2.0	2.1	
8732/1	4	395	547	0.1	1.8	3.2	
8732/1	5	509	725	0.1	1.6	2.8	
8732/1	6	598	981	0.1	1.1	3.2	0.07
8732/1	7	639	1287	0.0	1.1	5.4	0.14
8732/1	8	705	1415	0.0	1.1	4.1	
8732/1	9	773	1534	0.0	0.7	4.6	
8732/2	1	30	30	0.2	2.3	1.7	0.07
8732/2	2	150	150	0.2	1.5	1.8	
8732/2	3	269	295	0.1	1.4	2.5	
8732/2	4	395	547	0.1	1.6	3.6	
8732/2	5	509	725	0.1	1.3	3.2	0.35
8732/2	6	598	981	0.1	1.0	4.7	
8732/2	7	639	1287	0.1	1.0	4.6	
8732/2	8	705	1415	0.1	0.9	4.6	0.14
8732/2	9	773	1534	0.0	0.7	4.6	

Table 4 -- Model Peak Current (kA) vs. Path Length

Event	Path Length (m)					
(Flsh/ Stroke)	0	10	30	100	300	1000
8715/9	32.7	29.3	24.9	19.9	18.4	16.8
8715/10	15.4	11.7	10.9	10.4	9.2	7.8
8725/1	20.1	18.4	16.0	12.5	9.8	7.1
8725/2	16.3	13.3	12.2	10.5	8.0	6.3
8725/3	43.0	31.3	25.2	23.0	20.0	15.8
8725/5	11.7	8.6	7.8	7.1	5.5	3.4
8726/1	38.3	25.1	18.4	17.0	16.4	15.8
8726/2	26.6	24.8	22.3	18.8	14.8	9.9
8726/3	16.2	11.8	10.9	10.3	8.9	6.2
8726/4	22.2	20.7	18.6	15.7	12.1	8.0
8728/10	26.8	25.5	23.3	18.8	14.9	12.0
8728/11	15.8	15.2	14.1	11.3	7.9	5.4
8732/1	17.9	17.1	15.6	12.5	9.5	7.3
8732/2	16.6	15.7	14.1	11.3	9.0	6.7
Mean Scaled (see text)	1.58	1.33	1.17	1.00	0.82	0.63
Stdev. Scaled	0.24	0.11	0.08	0.00	0.07	0.12

Table 5 -- Comparison Among Values Averaged Over Strokes

	Path Length above Surface						
Parameter	0 m	10 m	30 m	100 m	300 m	1000 m	Averaged
10-90% Rise Time of Current Waveform:							
Average (μs)	0.312	0.313	0.332	0.460	0.884	2.18	
Std. Dev. (μs)	0.172	0.168	0.158	0.126	0.165	0.47	
# Samples	24	24	24	24	24	24	
10-90% Rise Time of Relative Light Intensity:							
Average (μs)			1.3		2.0	3.8	
Std. Dev. (μs)			0.4		0.6	1.0	
# Samples			14		18	20	
Average Path (m)			30		303	1062	
Std. Dev. Path (m)			0		49	86	
Effective Current-Propagation Speed:							
Average (10^8 m/s)		1.76		1.75	1.78	1.81	1.80
Std. Dev. (10^8 m/s)		0.30		0.20	0.22	0.30	0.24
# Samples		24		24	24	22	24
2-D Average Optical-Propagation Speed:							
Average (10^8 m/s)							1.5
Std. Dev. (10^8 m/s)							0.1
# Samples							14
Charge-Amplitude Multiplier:							
Average	1.00	0.88	0.79	0.68	0.58	0.49	
Std. Dev.	0.00	0.10	0.11	0.08	0.06	0.09	
# Samples		24	24	24	24	24	
Peak Amplitude of Current Waveform:							
Average (kA)	22.8	19.2	16.7	14.2	11.7	9.2	
Std. Dev. (kA)	9.4	7.1	5.6	4.6	4.4	4.3	
# Samples	14	14	14	14	14	14	
Amplitude of Relative Light Intensity:							
Average			2.2		1.1	0.9	
Std. Dev.			0.9		0.6	0.5	
# Samples			14		18	20	
Average Path (m)			30		303	1062	
Std. Dev. Path (m)			0		49	86	

Table 6 -- Correlations with Leader Relative Brightness

Event	RLI Ratio	$a(100)$	$v_{eff}(10)/v_{TLM}$
8715/2		0.78	1.06
8715/3		0.75	1.20
8715/4		0.73	1.23
8715/6		0.72	1.08
8715/7		0.61	1.40
8715/8		0.74	1.16
8715/9	0.36	0.61	1.35
8715/10	0.10	0.69	1.35
8717/3		0.70	1.12
8717/5		0.76	1.11
8725/1	0.23	0.64	1.41
8725/2	0.17	0.66	1.32
8725/3	0.59	0.54	1.62
8725/4		0.76	0.96
8725/5		0.64	1.44
8726/1	0.37	0.45	2.63
8726/2	0.04	0.72	1.35
8726/3		0.65	1.44
8726/4	0.00	0.72	1.34
8726/5		0.63	1.50
8728/10	0.32	0.71	1.23
8728/11	0.13	0.75	0.98
8732/1	0.05	0.71	1.46
8732/2	0.08	0.69	1.34

Table A1 -- Camera-orientation angles, as defined in Figure A2. α_i represents elevation relative to the horizontal, and $-\gamma_i$ represents azimuth relative to the direction to the triggering site. Subscript "N" stands for the NRL site, and "S" stands for SUNY.

Flash:	8715	8717	8725	8726	8728	8732
Parameter						
α_N (deg.)	9.98	9.65	10.08	9.96	9.84	9.87
γ_N (deg.)	1.32	1.34	1.97	1.74	1.89	2.02
γ_S (deg.)	-0.77	-1.33	-1.61	-1.74	-1.16	-1.68

Figure 1

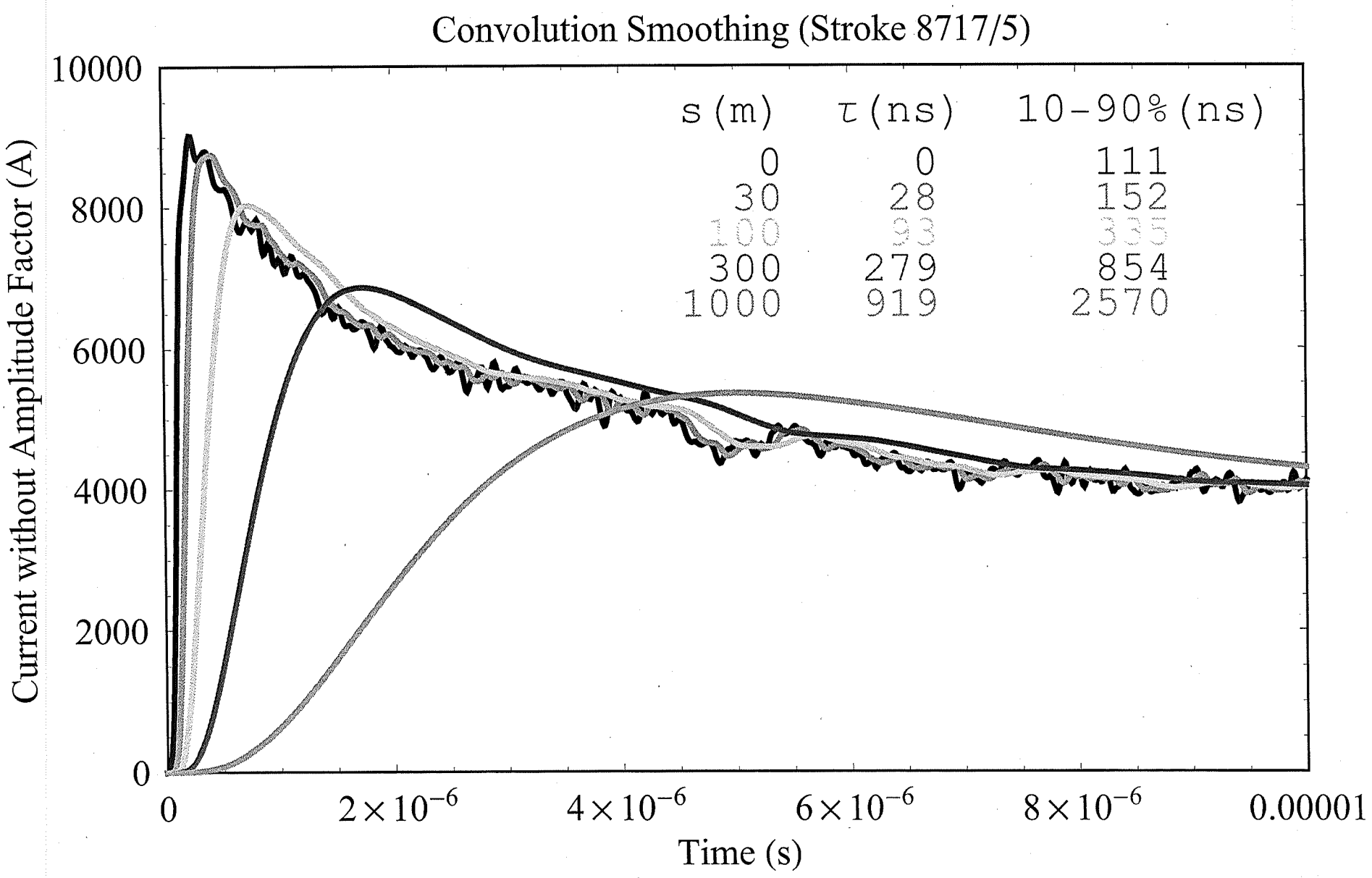
Convolution Smoothing (Stroke 8717/5)
Current without Amplitude Factor (A)
10000
8000
6000
4000
2000
0
0
2×10⁻⁶
4×10⁻⁶
6×10⁻⁶
8×10⁻⁶
0.00001
Time (s)
s(m) τ(ns) 10-90%(ns)
0 0 111
30 28 152
100 93 335
300 279 854
1000 919 2570

Figure 2a

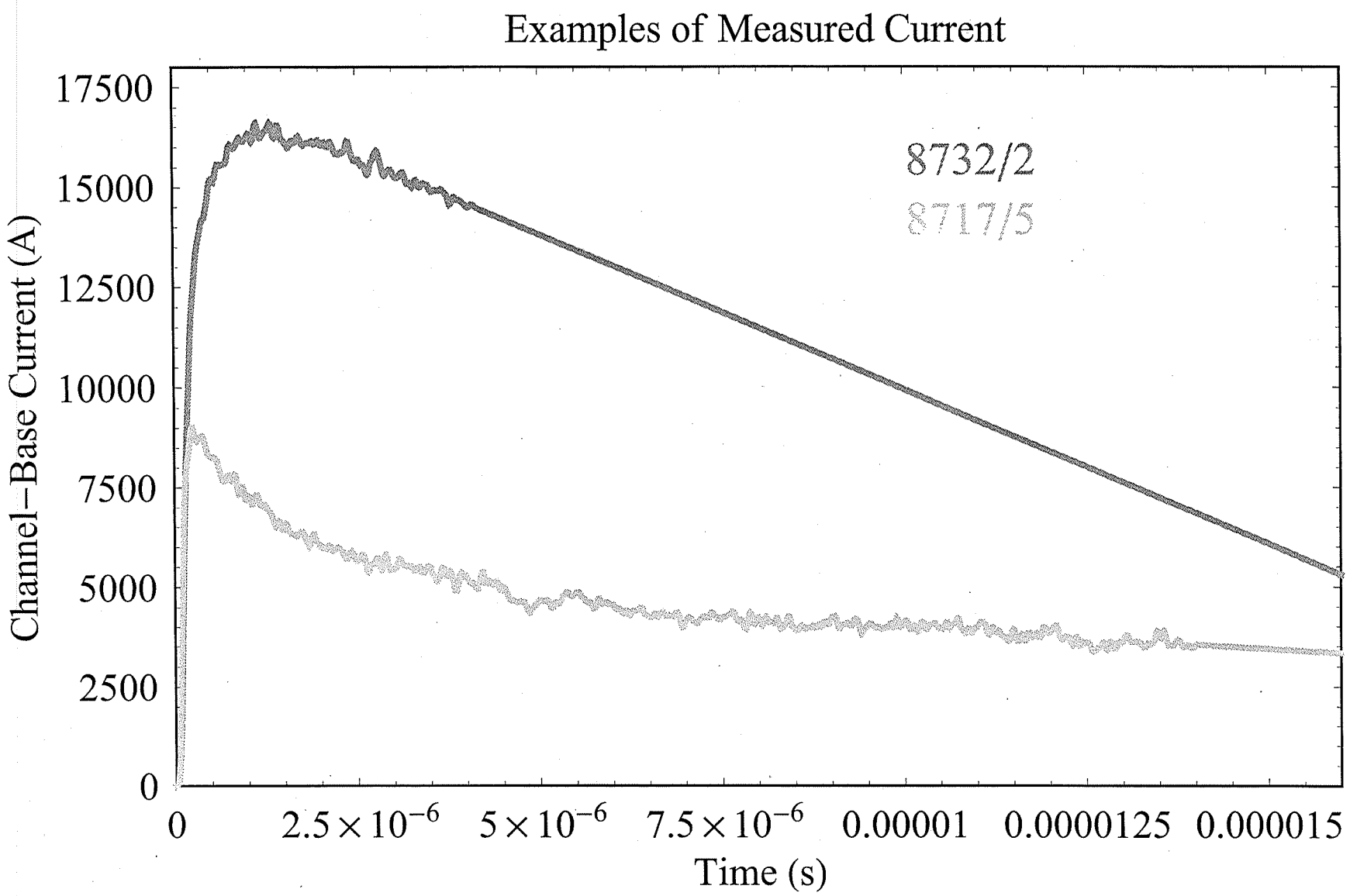
Examples of Measured Current
Channel–Base Current (A)
17500
15000
12500
10000
7500
5000
2500
0
8732/2
8717/5
0
2.5 × 10^−6
5 × 10^−6
7.5 × 10^−6
0.00001
0.0000125
0.000015
Time (s)

Figure 2b

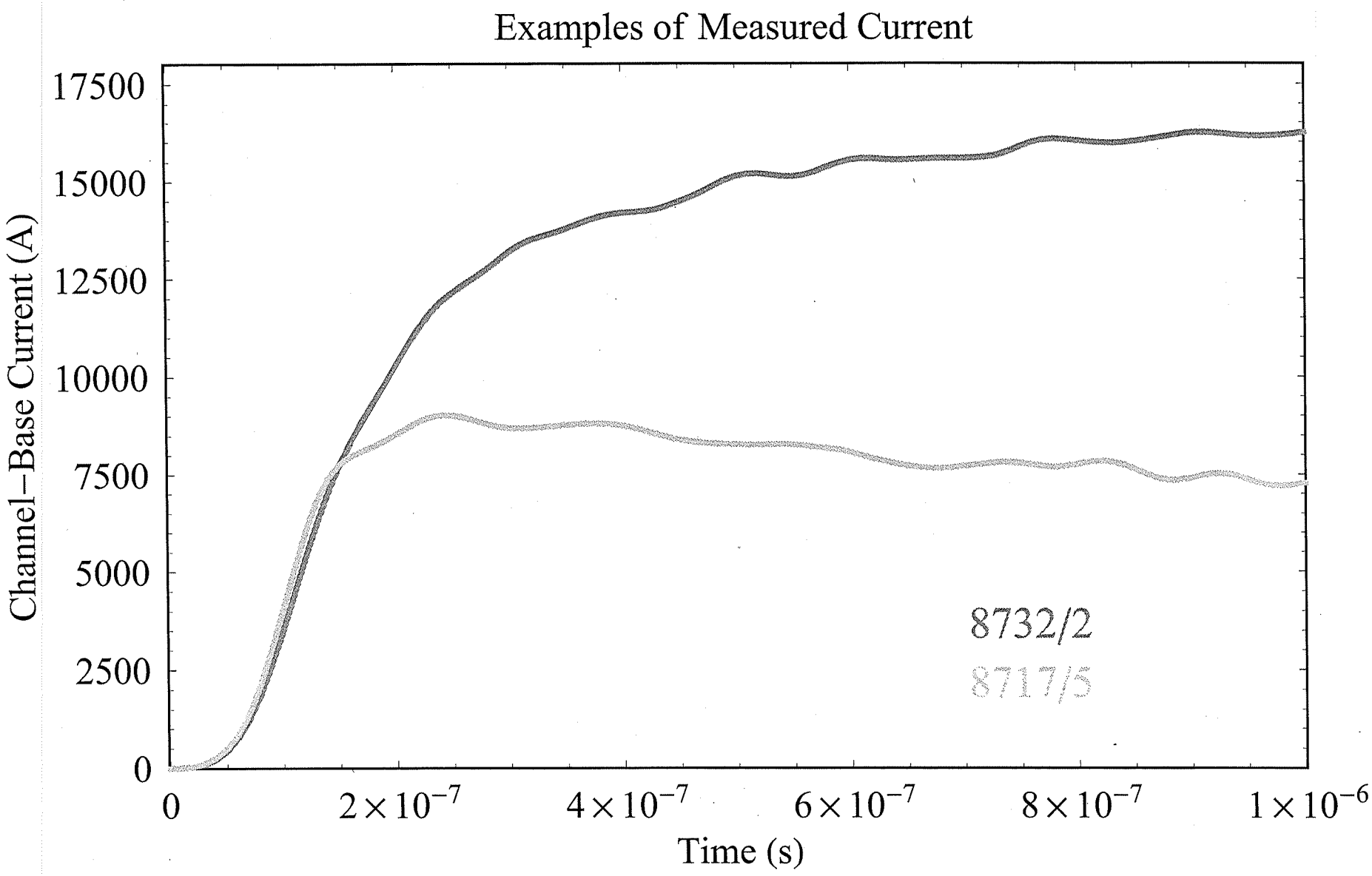
Examples of Measured Current
Channel–Base Current (A)
17500
15000
12500
10000
7500
5000
2500
0
0
2×10^{-7}
4×10^{-7}
6×10^{-7}
8×10^{-7}
1×10^{-6}
Time (s)
8732/2
8717/5

Figure 3

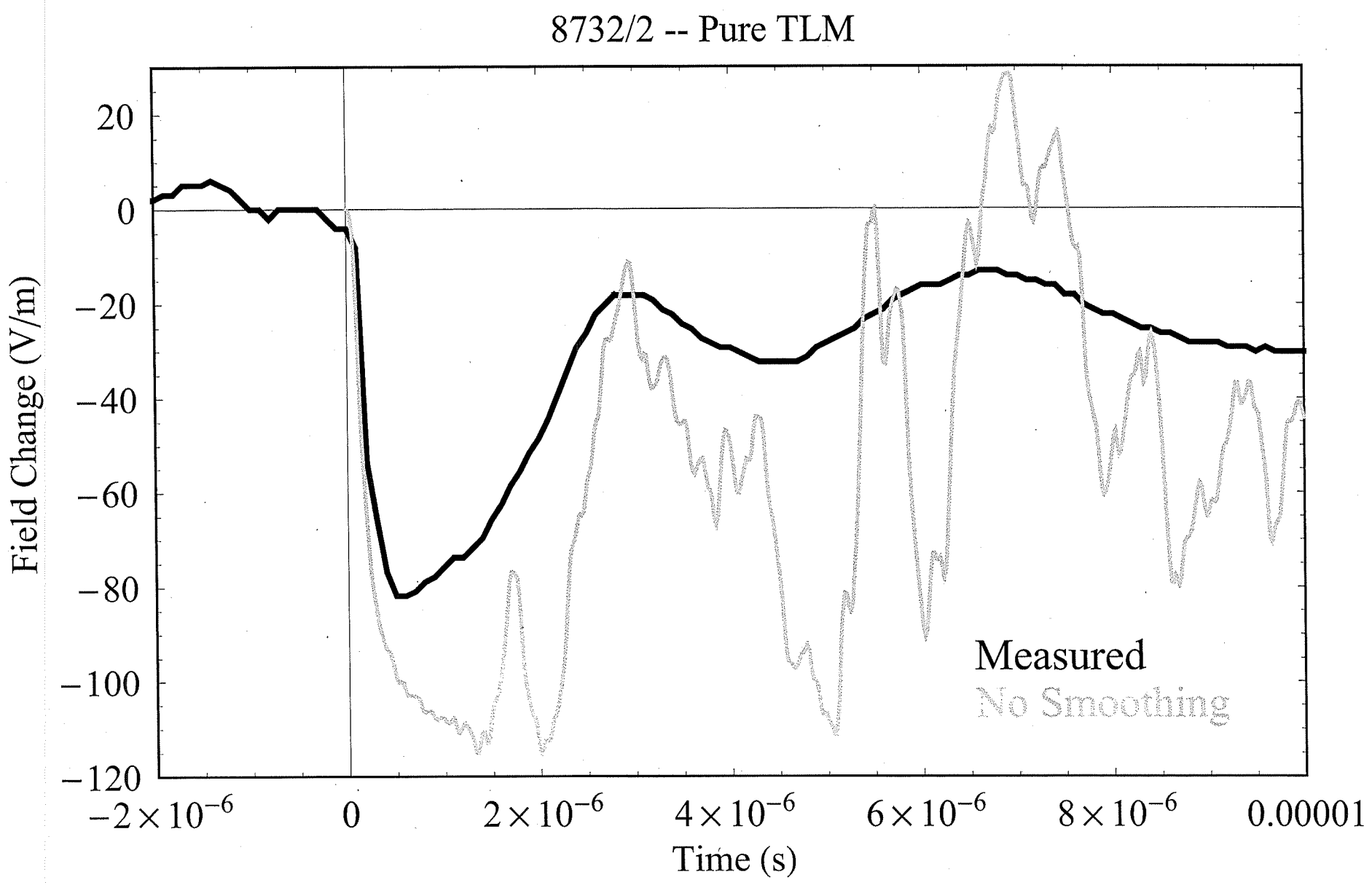
8732/2 -- Pure TLM
Field Change (V/m)
20
0
−20
−40
−60
−80
−100
−120
−2×10−6
0
2×10−6
4×10−6
6×10−6
8×10−6
0.00001
Time (s)
Measured
No Smoothing

Figure 4

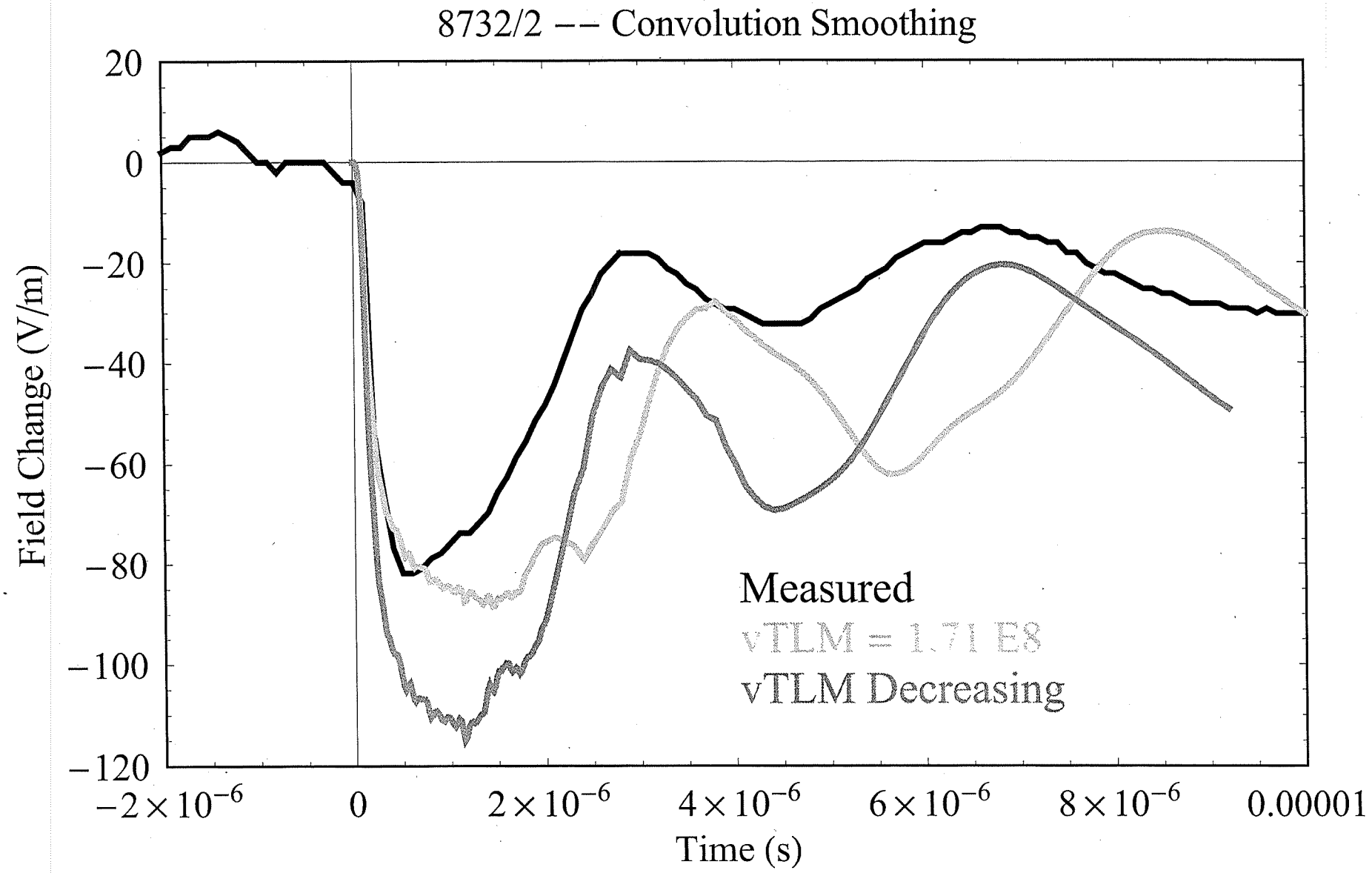
8732/2 -- Convolution Smoothing
Field Change (V/m)
20
0
−20
−40
−60
−80
−100
−120
−2×10−6
0
2×10−6
4×10−6
6×10−6
8×10−6
0.00001
Time (s)
Measured
vTLM = 1.71 E8
vTLM Decreasing

Figure 5

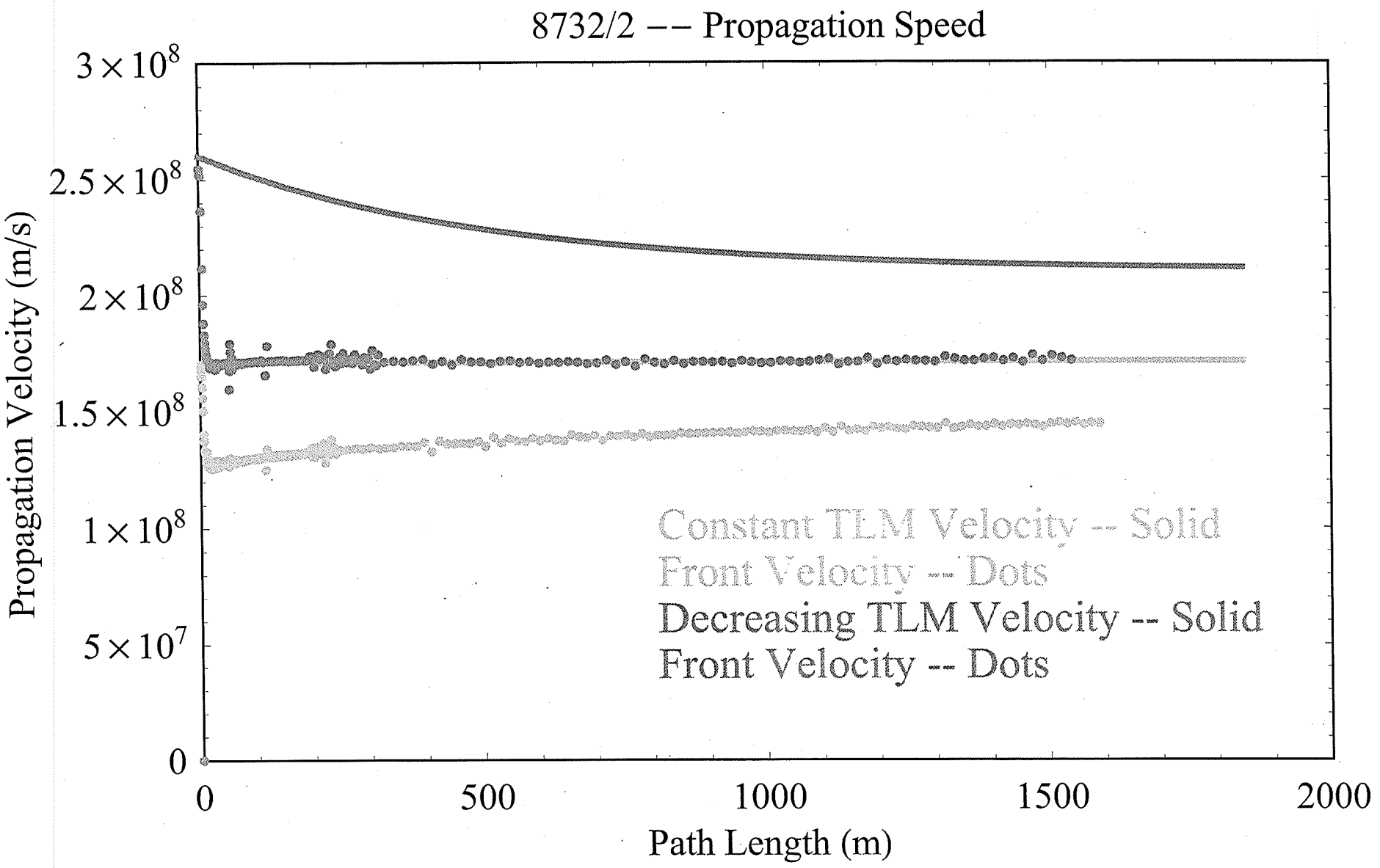
8732/2 -- Propagation Speed
Propagation Velocity (m/s)
3×10^8
2.5×10^8
2×10^8
1.5×10^8
1×10^8
5×10^7
0
0
500
1000
1500
2000
Path Length (m)
Constant TLM Velocity -- Solid
Front Velocity -- Dots
Decreasing TLM Velocity -- Solid
Front Velocity -- Dots

Figure 6

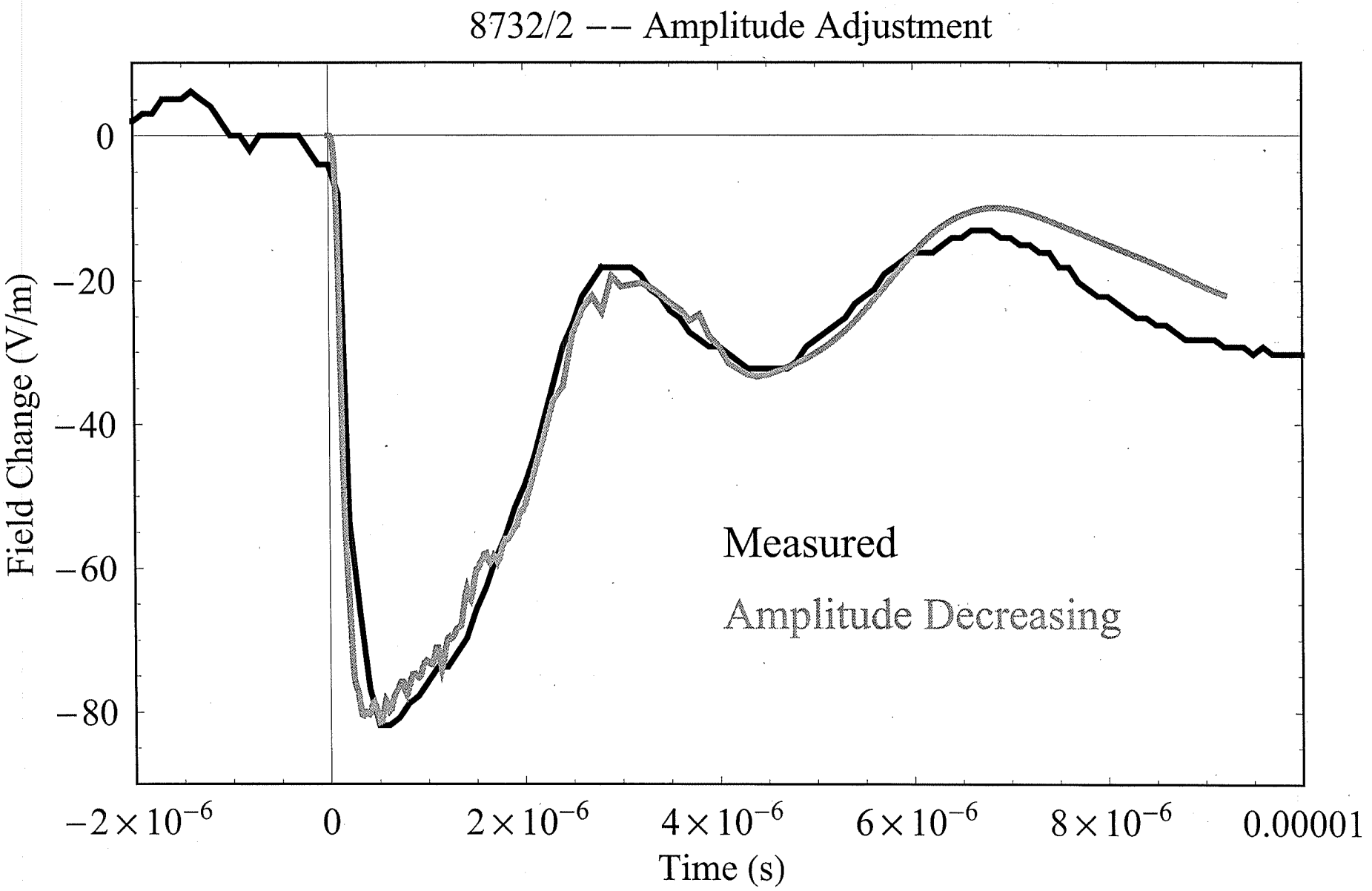
8732/2 -- Amplitude Adjustment
Field Change (V/m)
0
−20
−40
−60
−80
Measured
Amplitude Decreasing
−2×10−6
0
2×10−6
4×10−6
6×10−6
8×10−6
0.00001
Time (s)

Figure 7

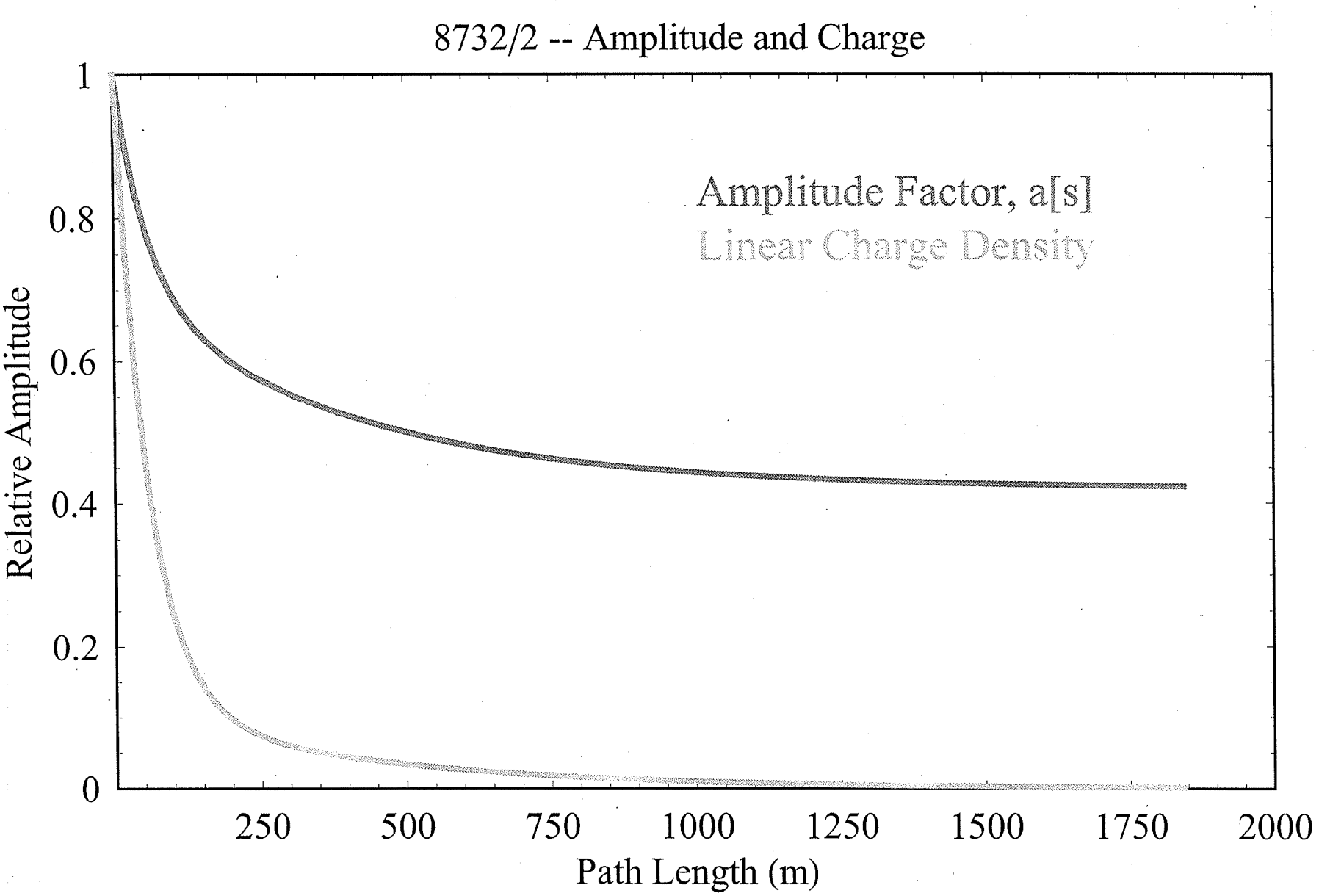
8732/2 -- Amplitude and Charge
Amplitude Factor, a[s]
Linear Charge Density
Relative Amplitude
1
0.8
0.6
0.4
0.2
0
250
500
750
1000
1250
1500
1750
2000
Path Length (m)

Figure 8

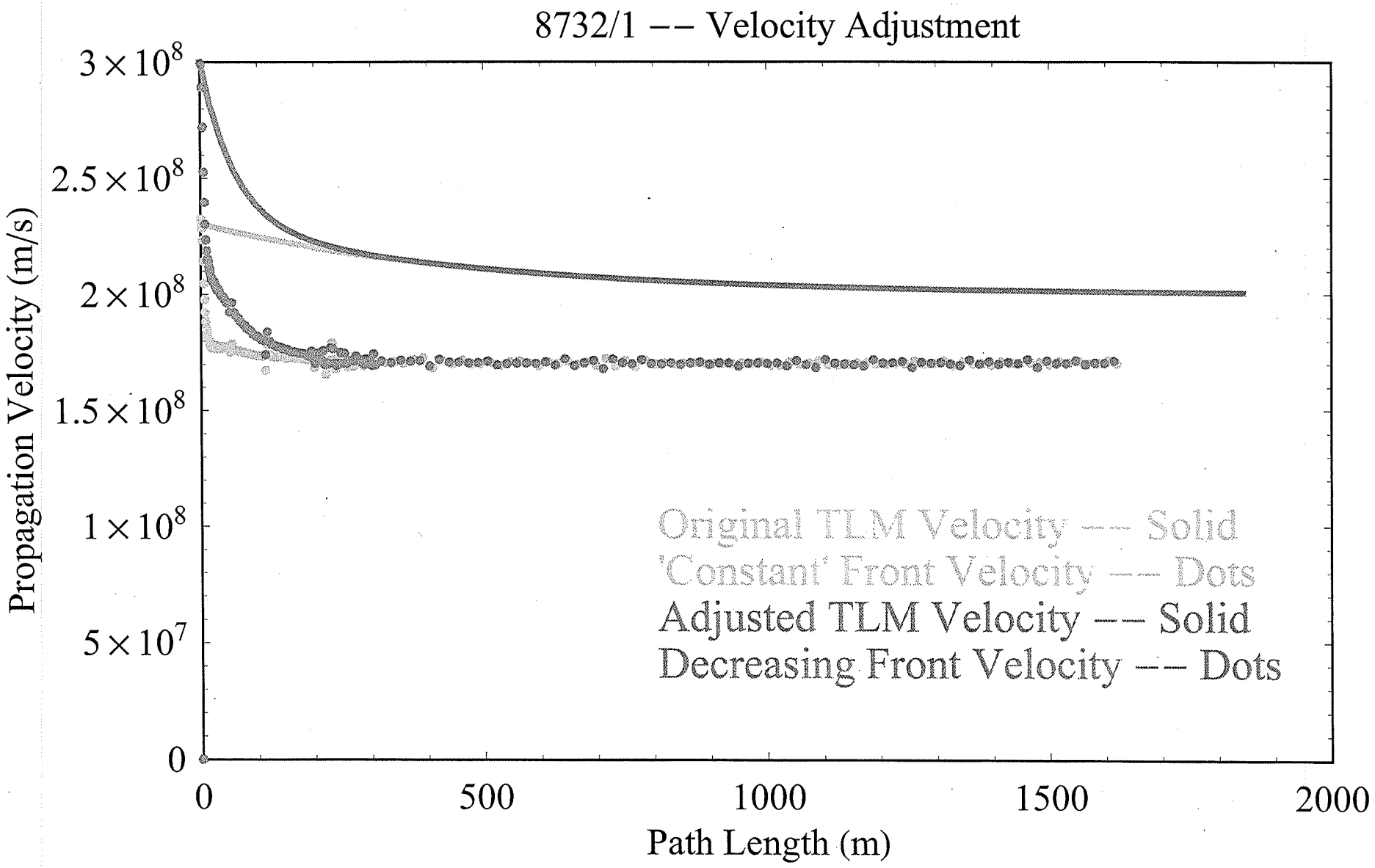
8732/1 -- Velocity Adjustment
Propagation Velocity (m/s)
3×10^8
2.5×10^8
2×10^8
1.5×10^8
1×10^8
5×10^7
0
0
500
1000
1500
2000
Path Length (m)
Original TLM Velocity -- Solid
'Constant' Front Velocity -- Dots
Adjusted TLM Velocity -- Solid
Decreasing Front Velocity -- Dots

Figure 9

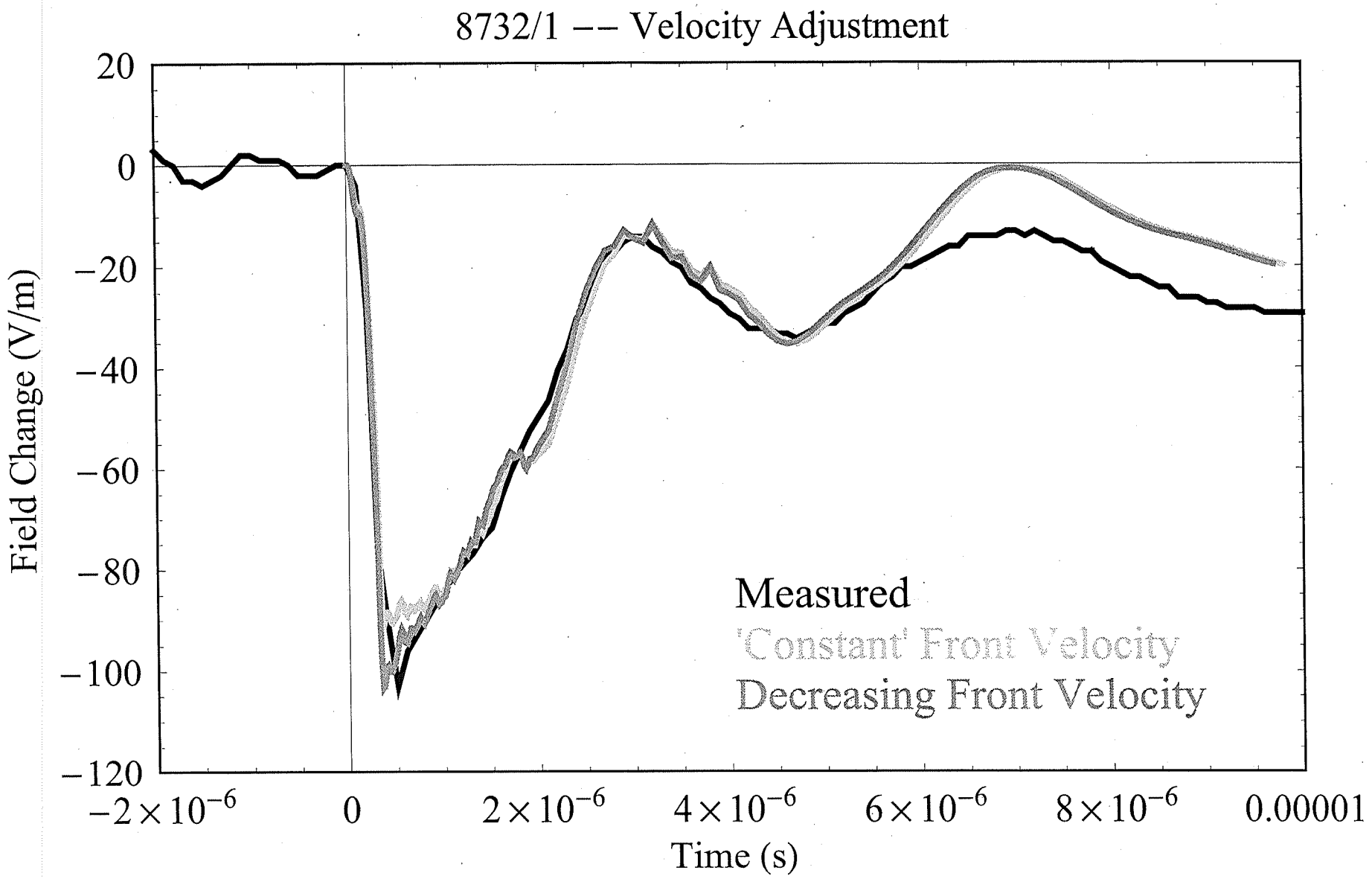
8732/1 -- Velocity Adjustment
20
0
−20
−40
−60
−80
−100
−120
Field Change (V/m)
−2×10−6
0
2×10−6
4×10−6
6×10−6
8×10−6
0.00001
Time (s)
Measured
'Constant' Front Velocity
Decreasing Front Velocity

Figure 10

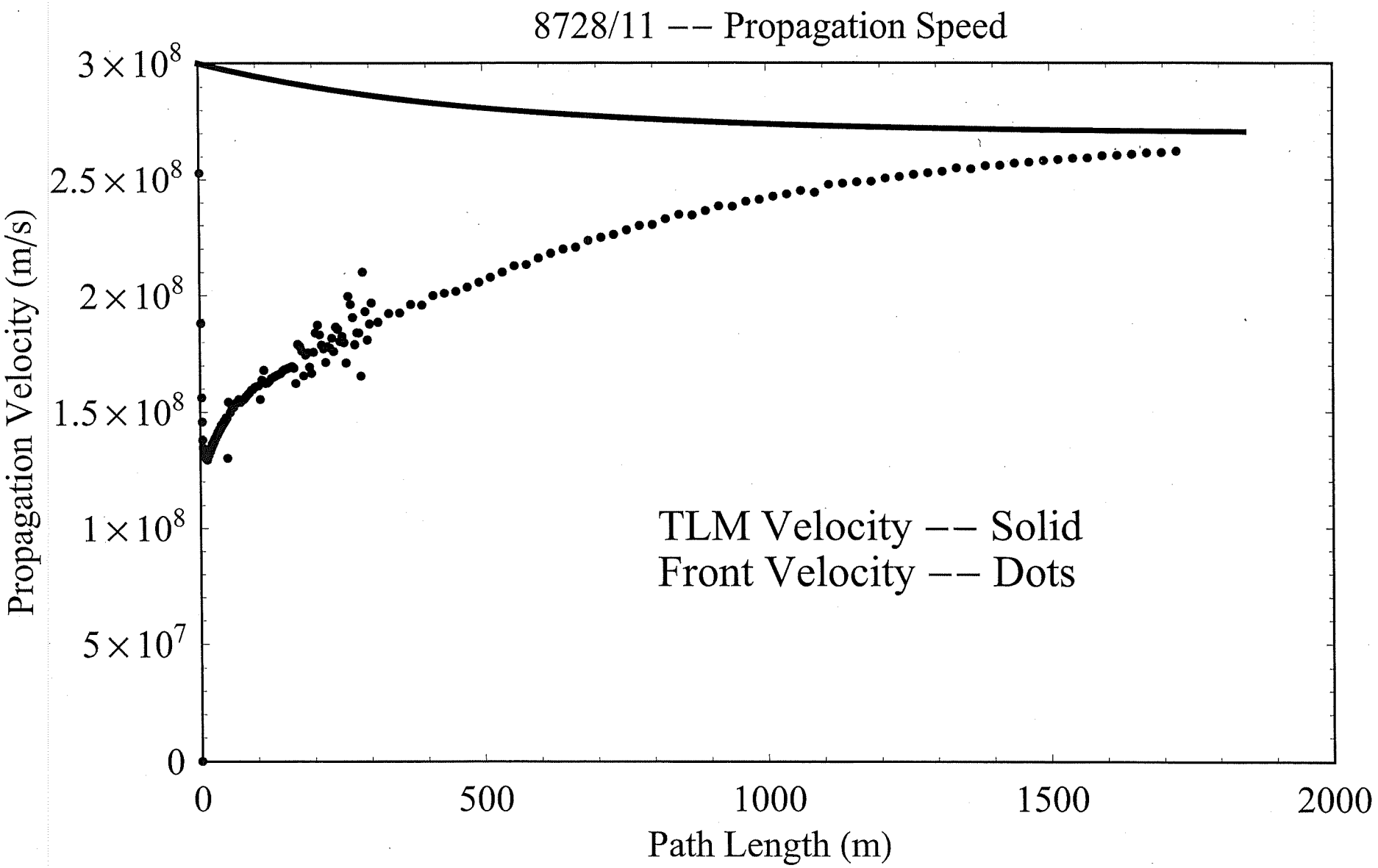
8728/11 -- Propagation Speed
Propagation Velocity (m/s)
3×10^8
2.5×10^8
2×10^8
1.5×10^8
1×10^8
5×10^7
0
0
500
1000
1500
2000
Path Length (m)
TLM Velocity -- Solid
Front Velocity -- Dots

Figure 11

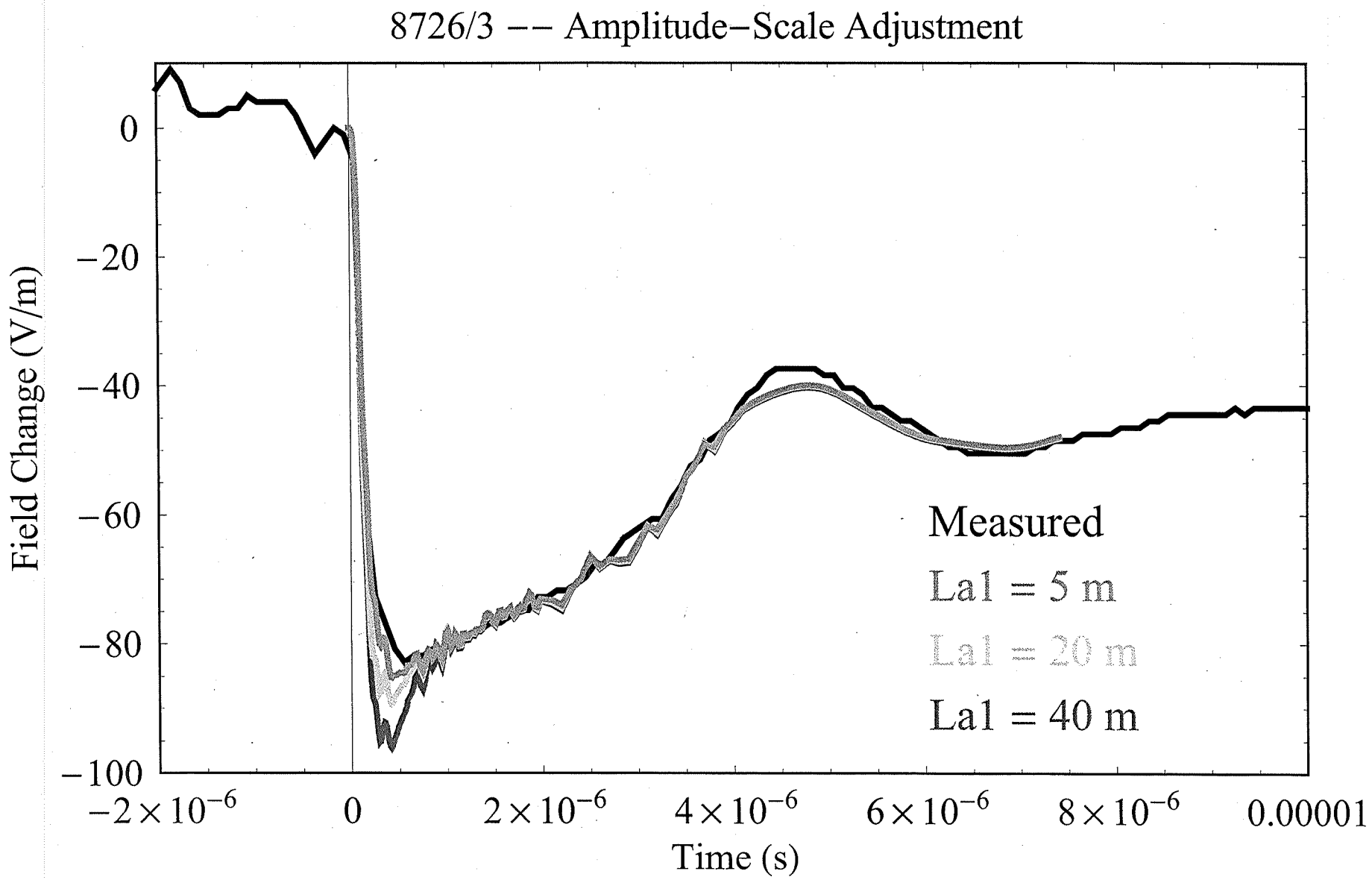
8726/3 -- Amplitude-Scale Adjustment
Field Change (V/m)
0
−20
−40
−60
−80
−100
−2×10^−6
0
2×10^−6
4×10^−6
6×10^−6
8×10^−6
0.00001
Time (s)
Measured
La1 = 5 m
La1 = 20 m
La1 = 40 m

Figure 12

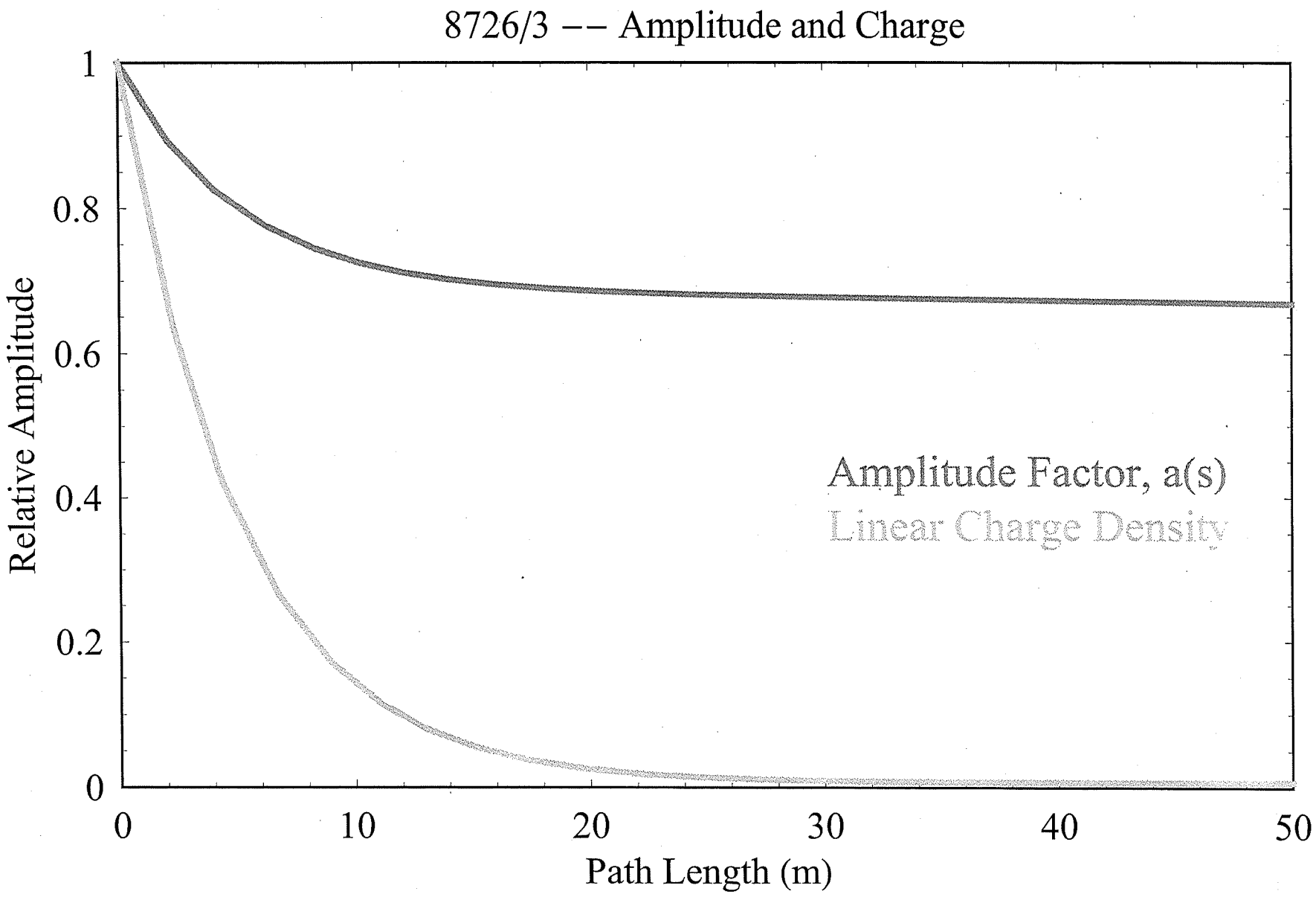
8726/3 -- Amplitude and Charge
Relative Amplitude
1
0.8
0.6
0.4
0.2
0
0
10
20
30
40
50
Path Length (m)
Amplitude Factor, a(s)
Linear Charge Density

Figure 13

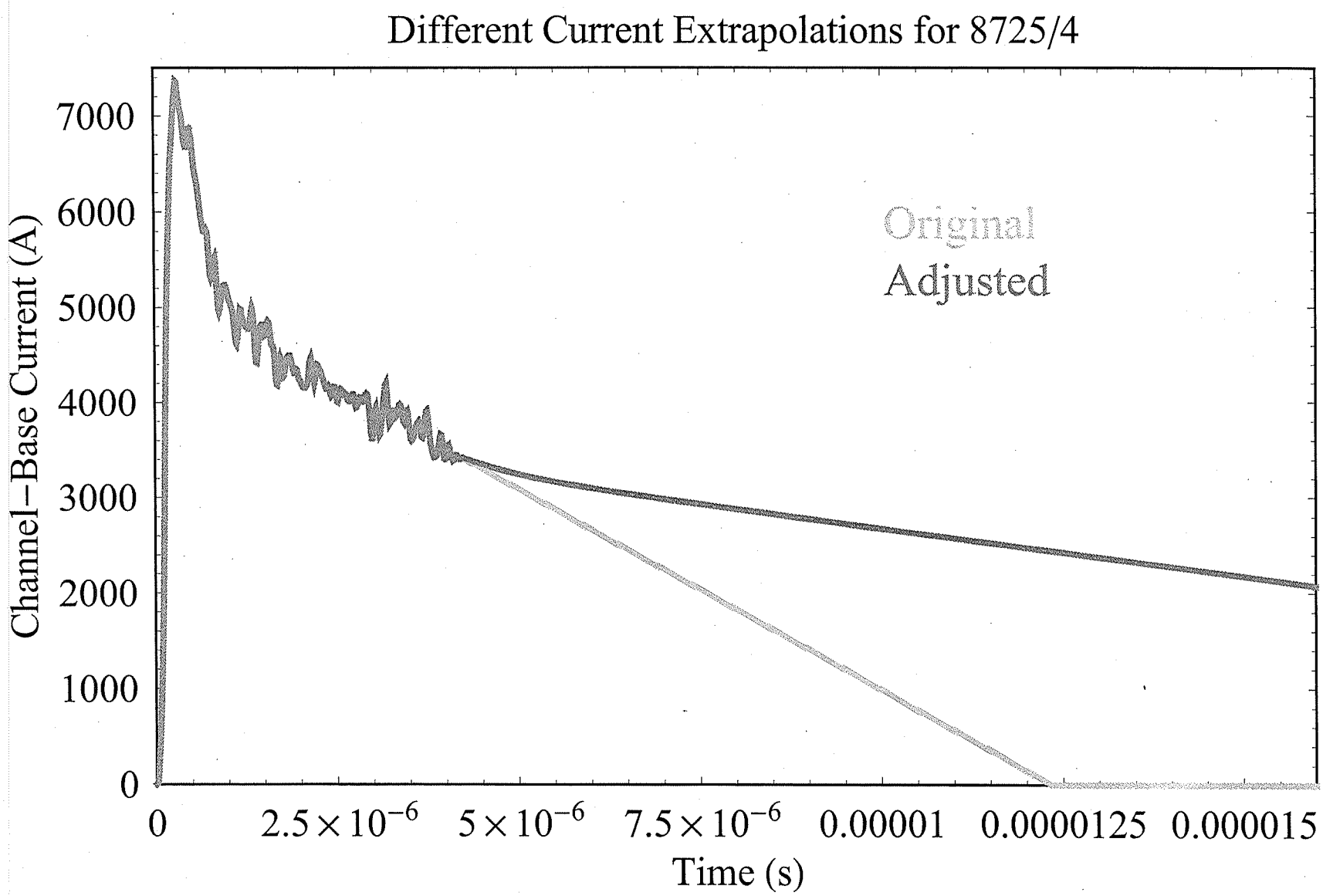
Different Current Extrapolations for 8725/4
Channel−Base Current (A)
7000
6000
5000
4000
3000
2000
1000
0
Original
Adjusted
0
2.5×10^−6
5×10^−6
7.5×10^−6
0.00001
0.0000125
0.000015
Time (s)

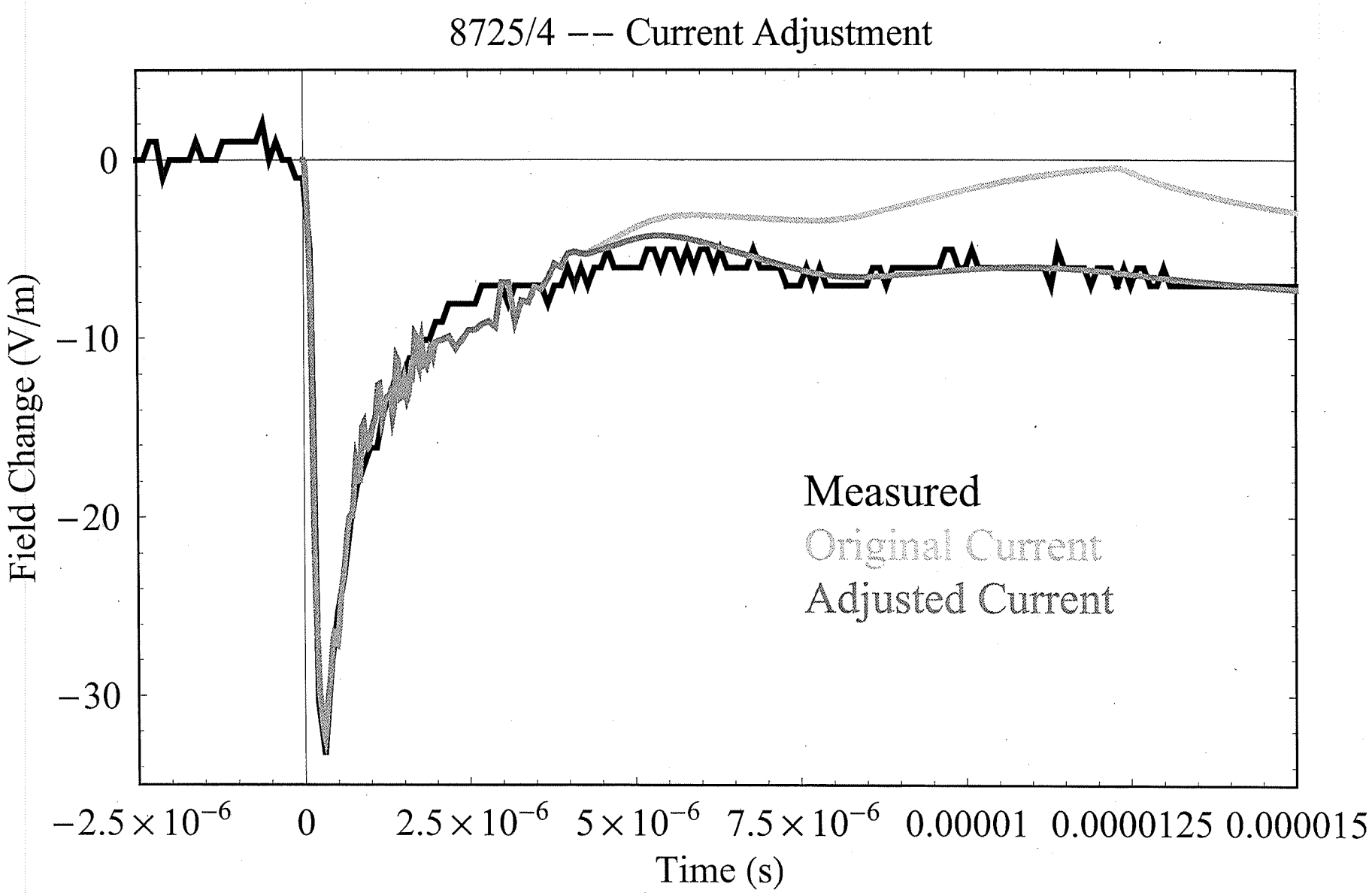
8725/4 -- Current Adjustment
Field Change (V/m)
0
−10
−20
−30
Measured
Original Current
Adjusted Current
-2.5×10^{-6}
0
2.5×10^{-6}
5×10^{-6}
7.5×10^{-6}
0.00001
0.0000125
0.000015
Time (s)

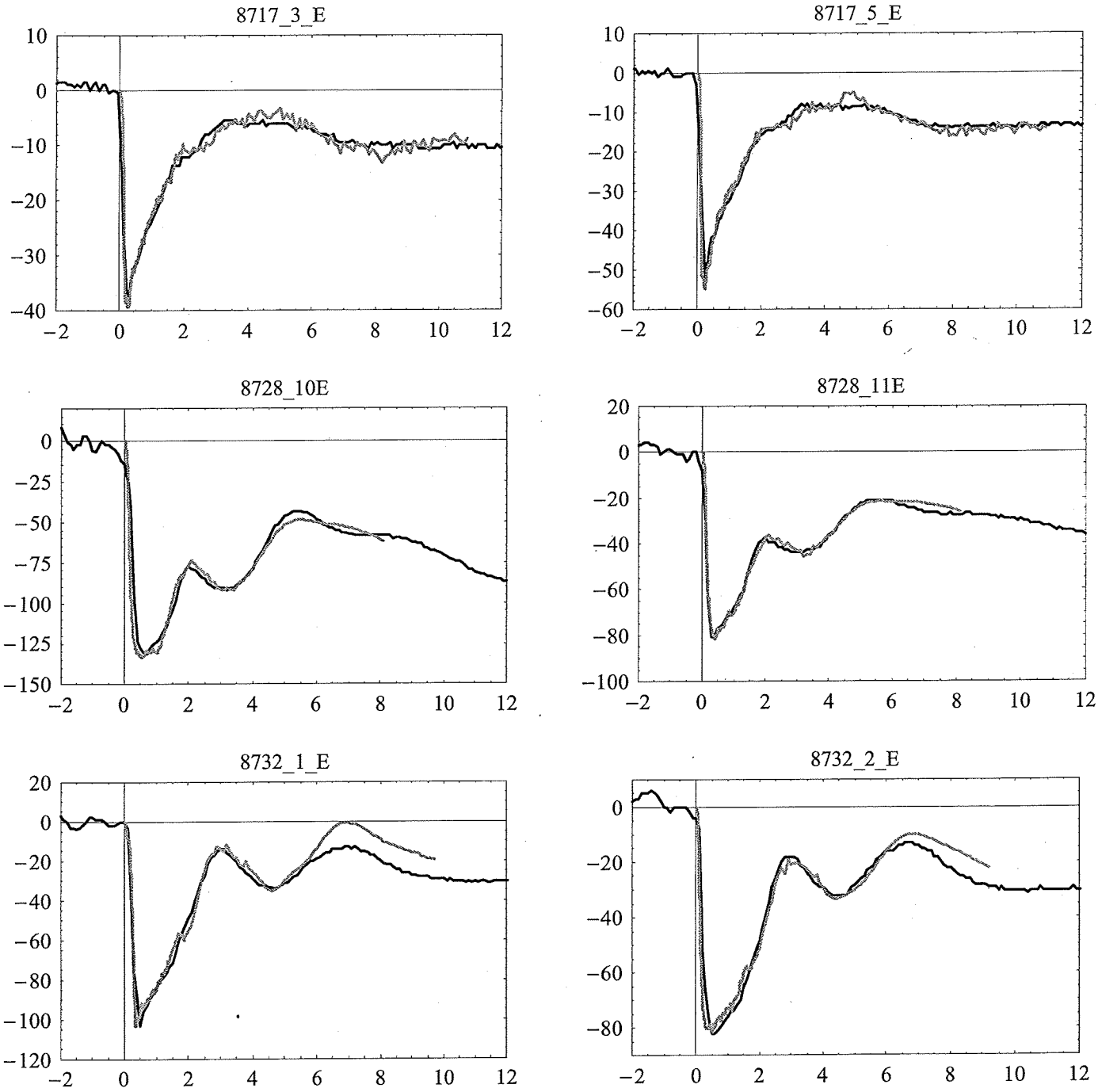

Figure 15a

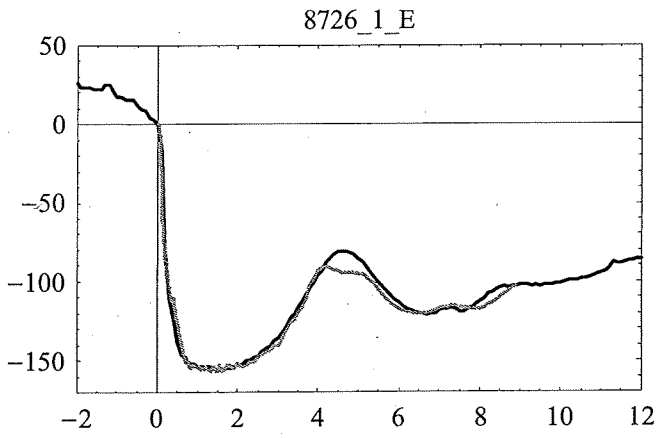
8726_1_E
50
0
−50
−100
−150
−2
0
2
4
6
8
10
12

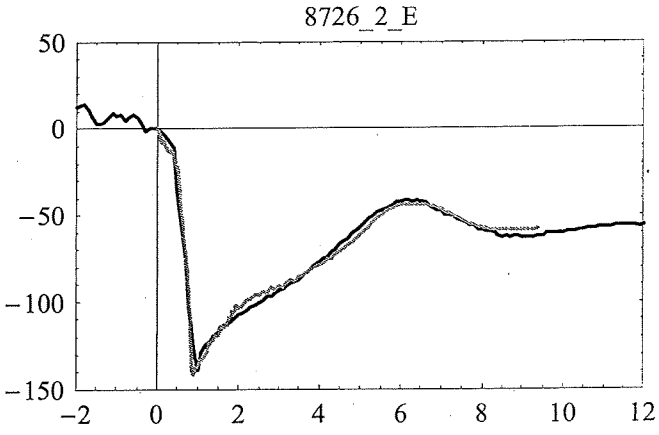
8726_2_E
50
0
−50
−100
−150
−2
0
2
4
6
8
10
12

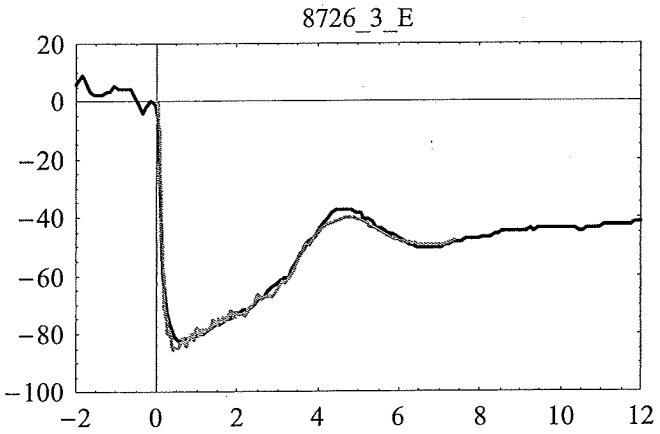
8726_3_E
20
0
−20
−40
−60
−80
−100
−2
0
2
4
6
8
10
12

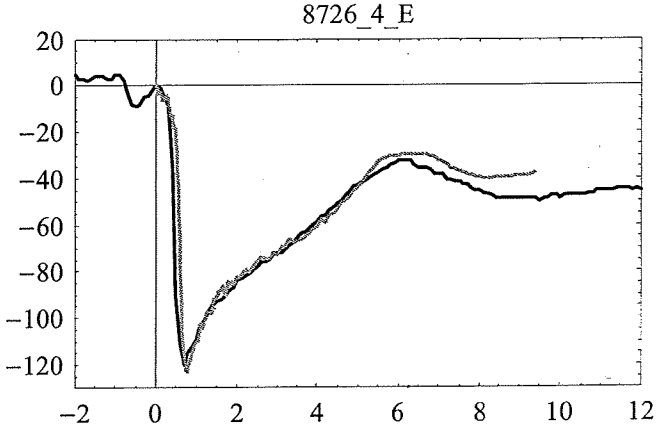
8726_4_E
20
0
−20
−40
−60
−80
−100
−120
−2
0
2
4
6
8
10
12

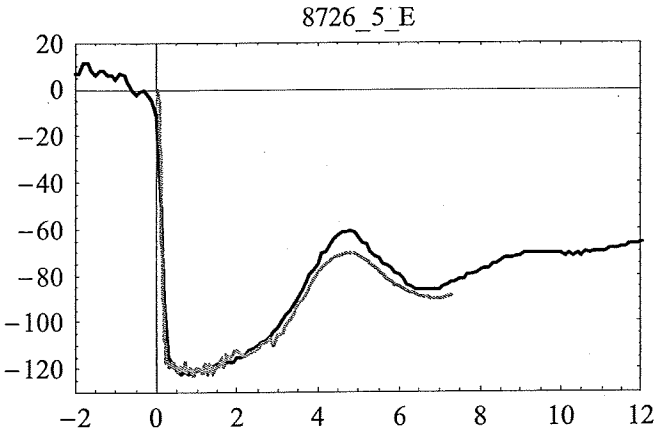
8726_5_E
20
0
−20
−40
−60
−80
−100
−120
−2
0
2
4
6
8
10
12

Figure 15b

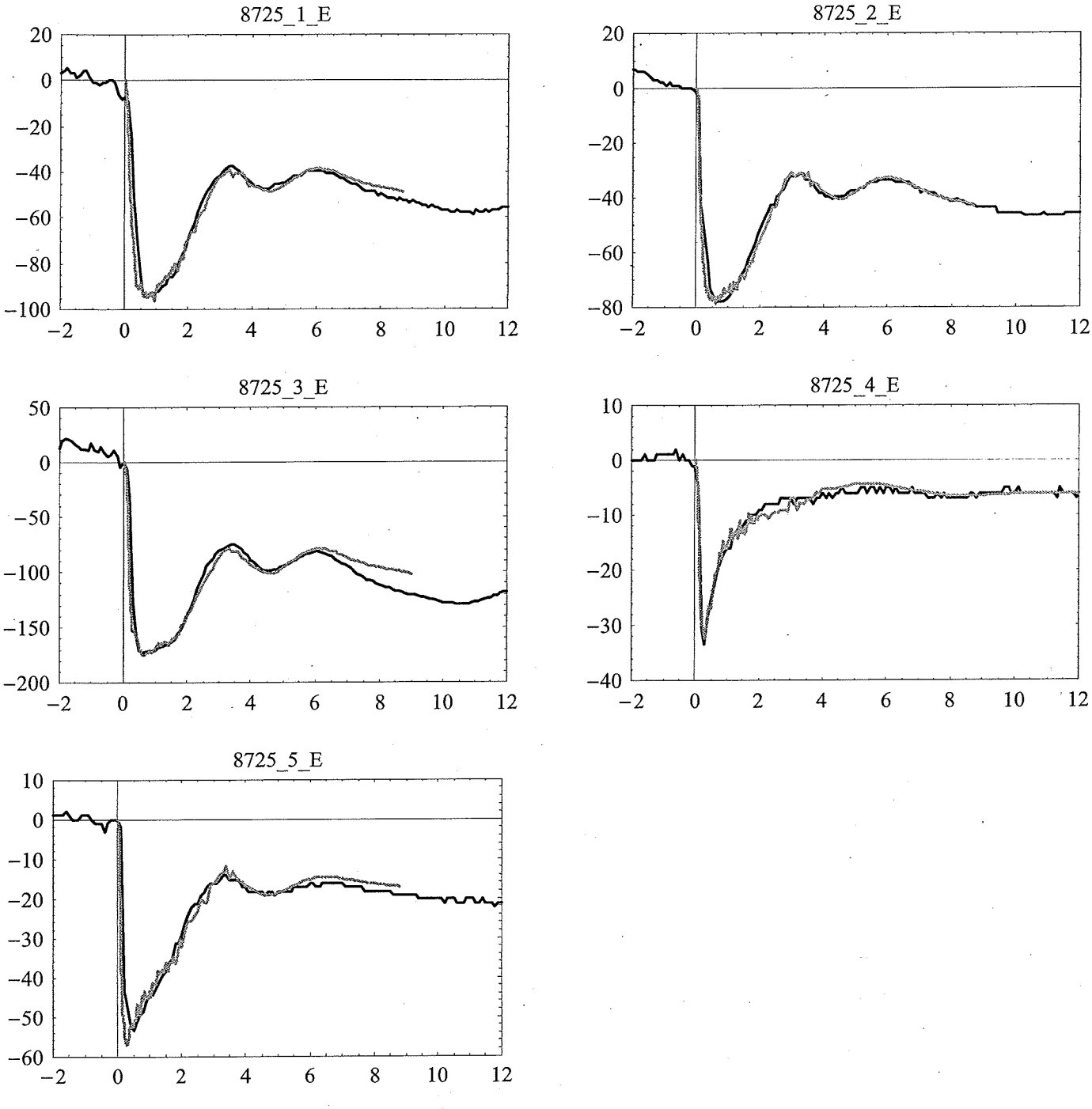

Figure 15c

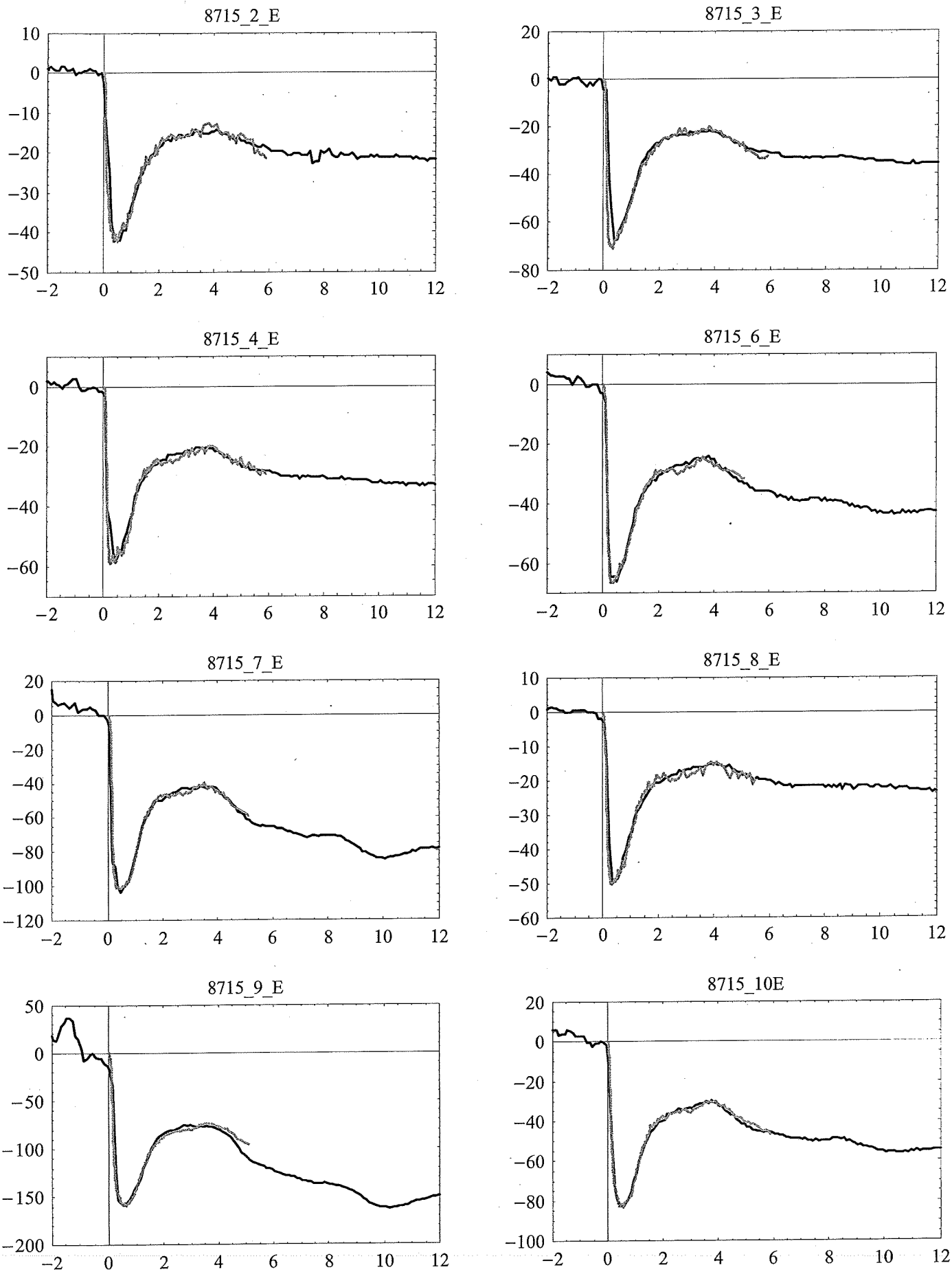

Figure 15d

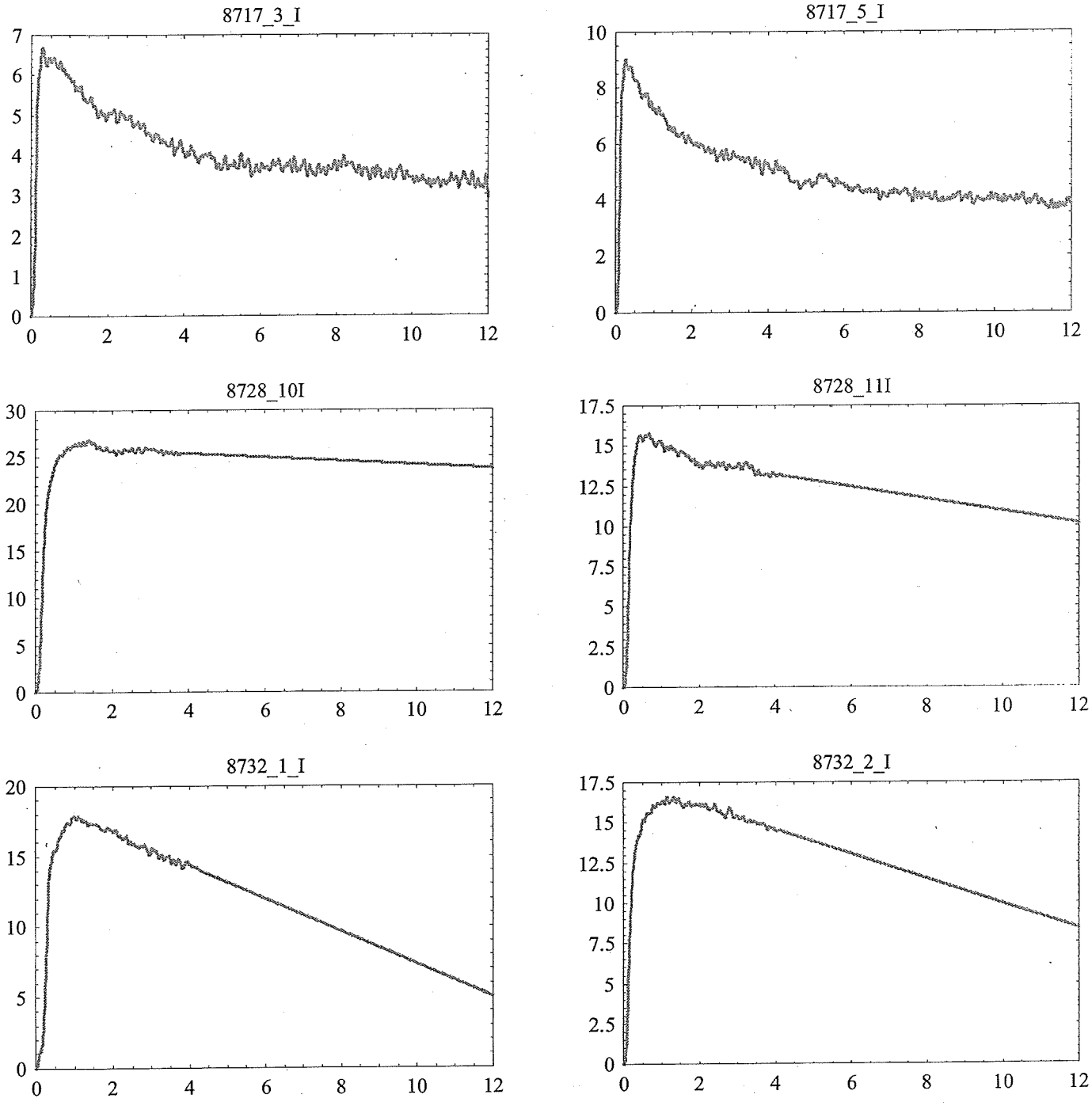

Figure 16a

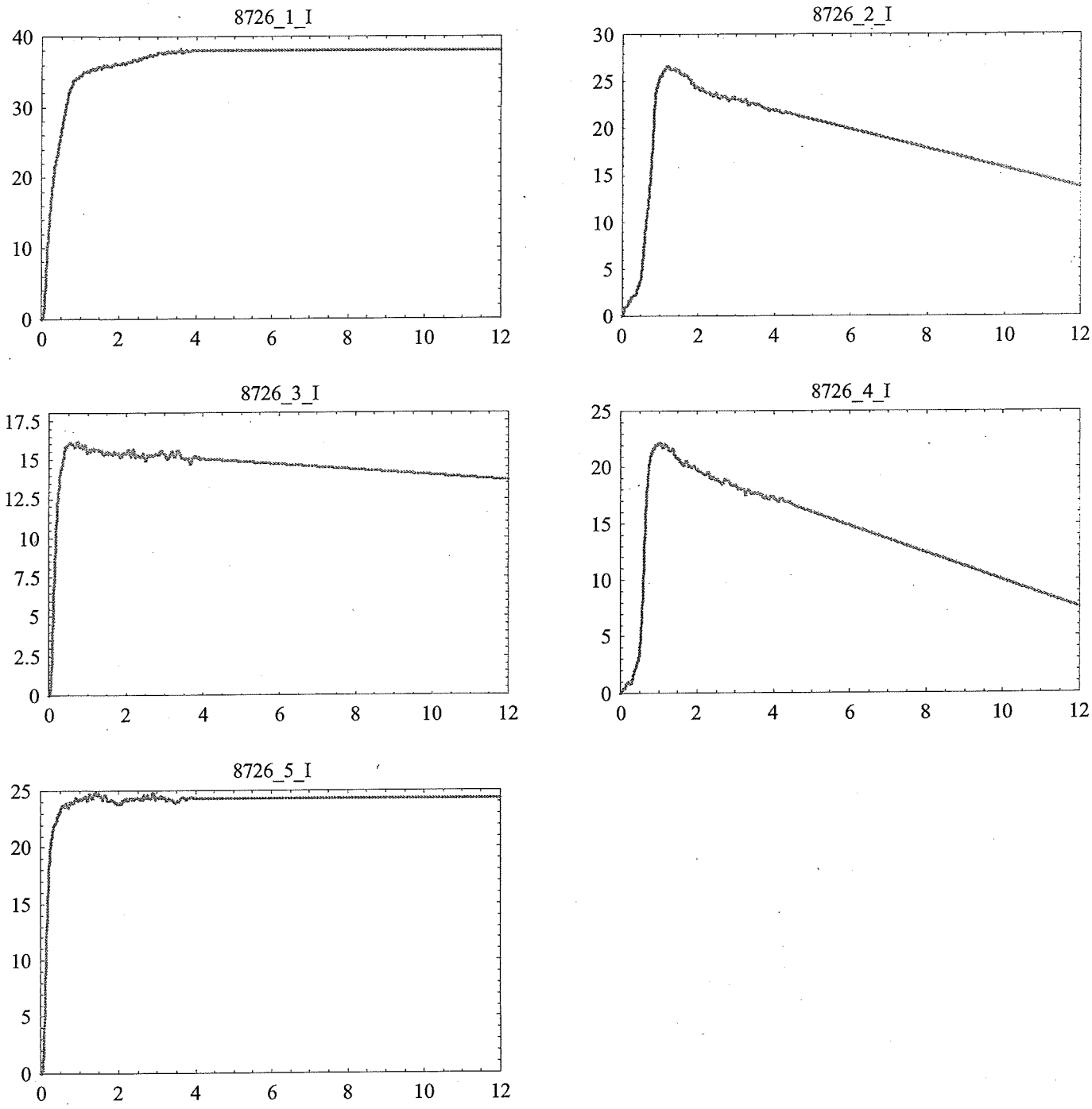

Figure 16b

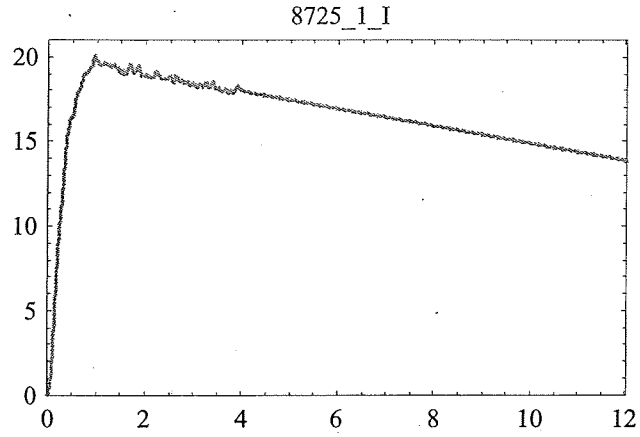
8725_1_I
20
15
10
5
0
0
2
4
6
8
10
12

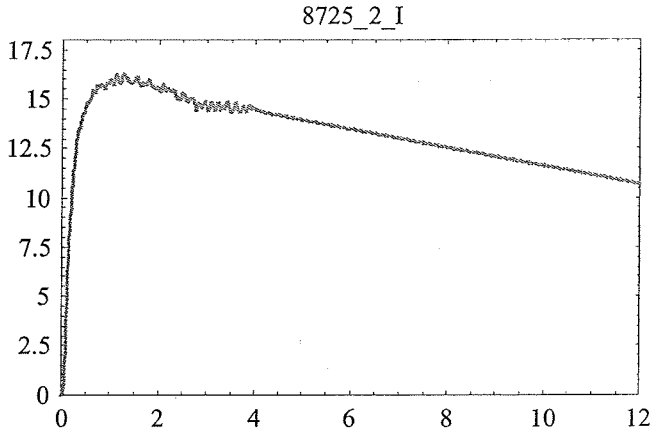
8725_2_I
17.5
15
12.5
10
7.5
5
2.5
0
0
2
4
6
8
10
12

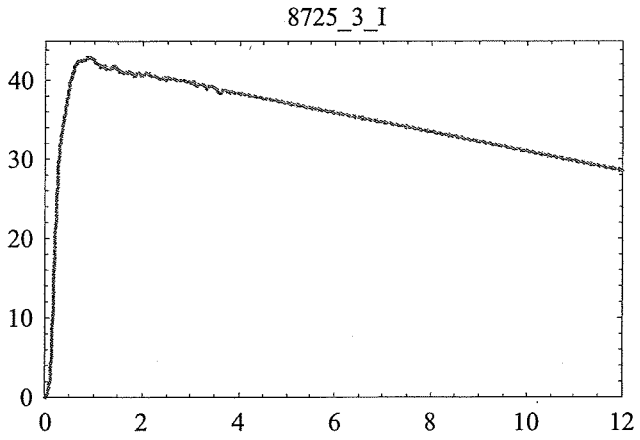
8725_3_I
40
30
20
10
0
0
2
4
6
8
10
12

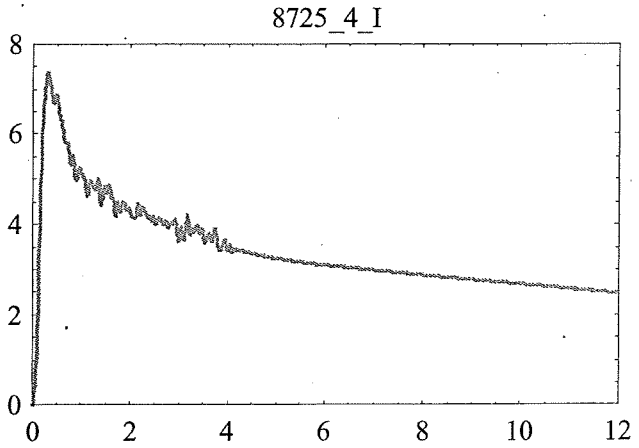
8725_4_I
8
6
4
2
0
0
2
4
6
8
10
12

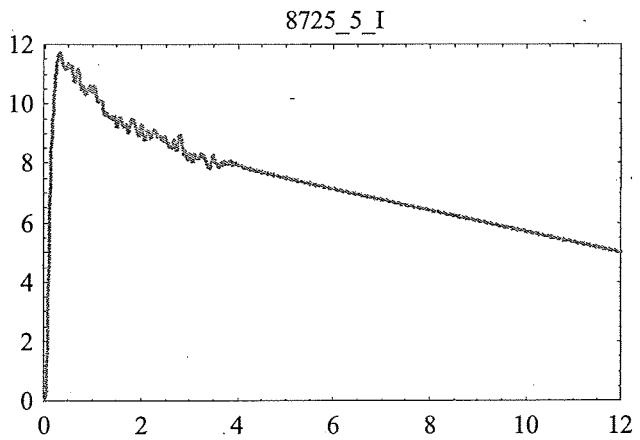
8725_5_I
12
10
8
6
4
2
0
0
2
4
6
8
10
12

Figure 16c

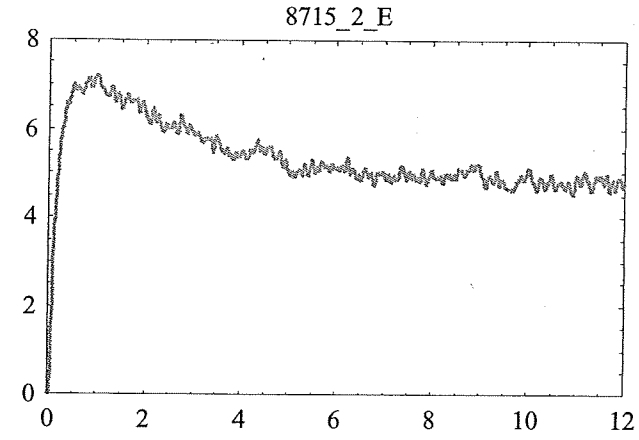
8715_2_E
0
2
4
6
8
0
2
4
6
8
10
12

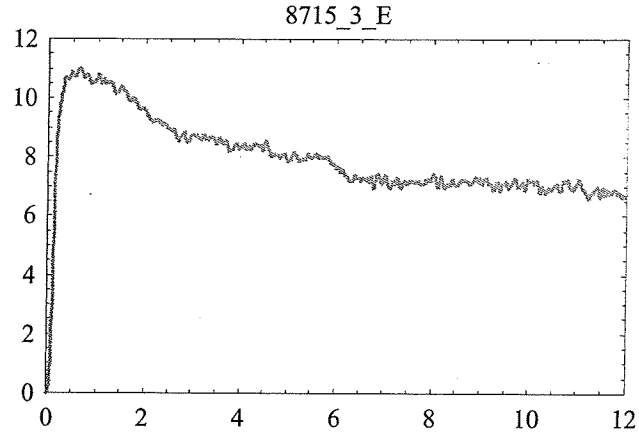
8715_3_E
0
2
4
6
8
10
12
0
2
4
6
8
10
12

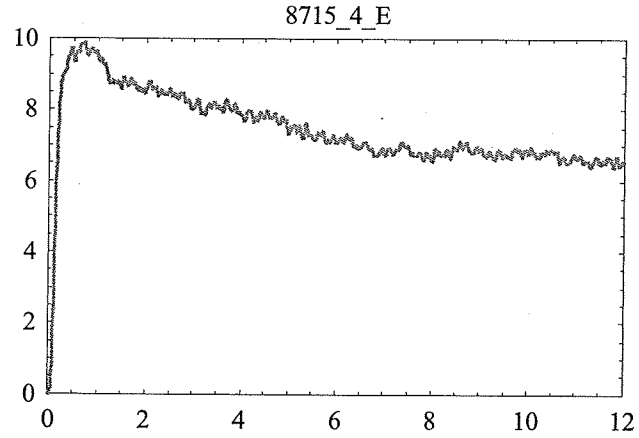
8715_4_E
0
2
4
6
8
10
0
2
4
6
8
10
12

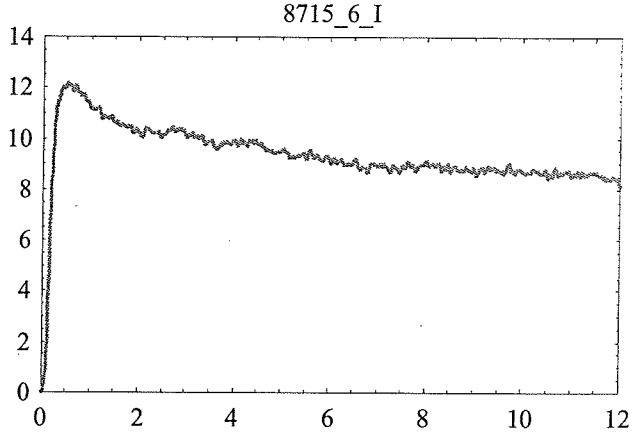
8715_6_I
0
2
4
6
8
10
12
14
0
2
4
6
8
10
12

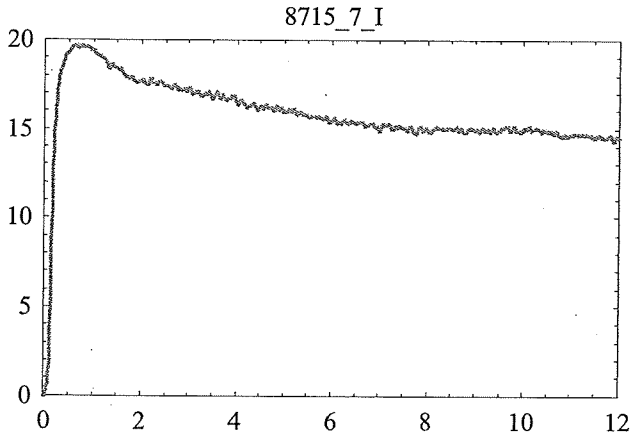
8715_7_I
0
5
10
15
20
0
2
4
6
8
10
12

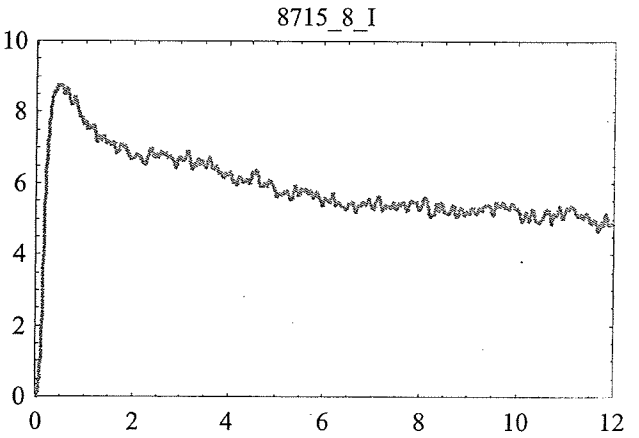
8715_8_I
0
2
4
6
8
10
0
2
4
6
8
10
12

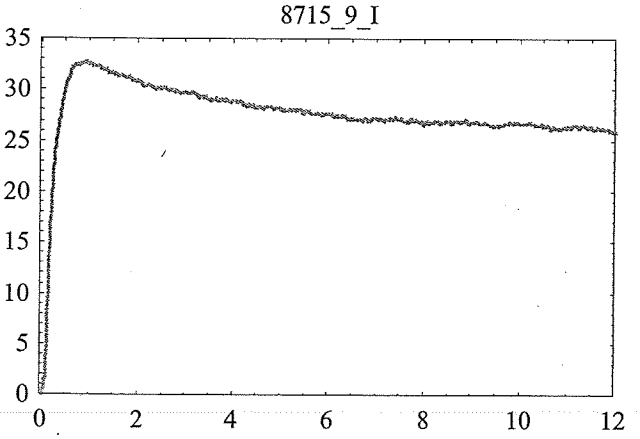
8715_9_I
0
5
10
15
20
25
30
35
0
2
4
6
8
10
12

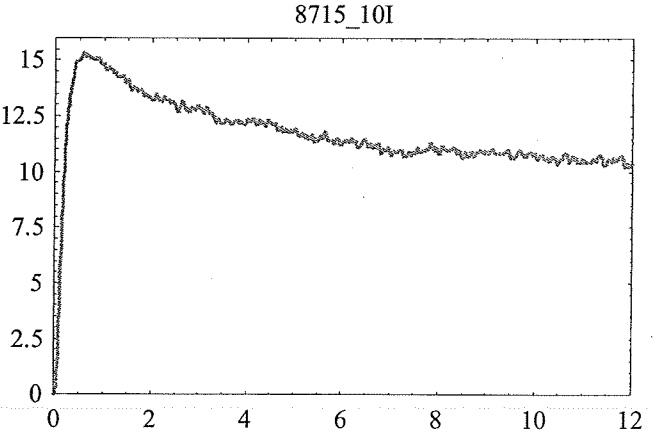
8715_10I
0
2.5
5
7.5
10
12.5
15
0
2
4
6
8
10
12

Figure 16d

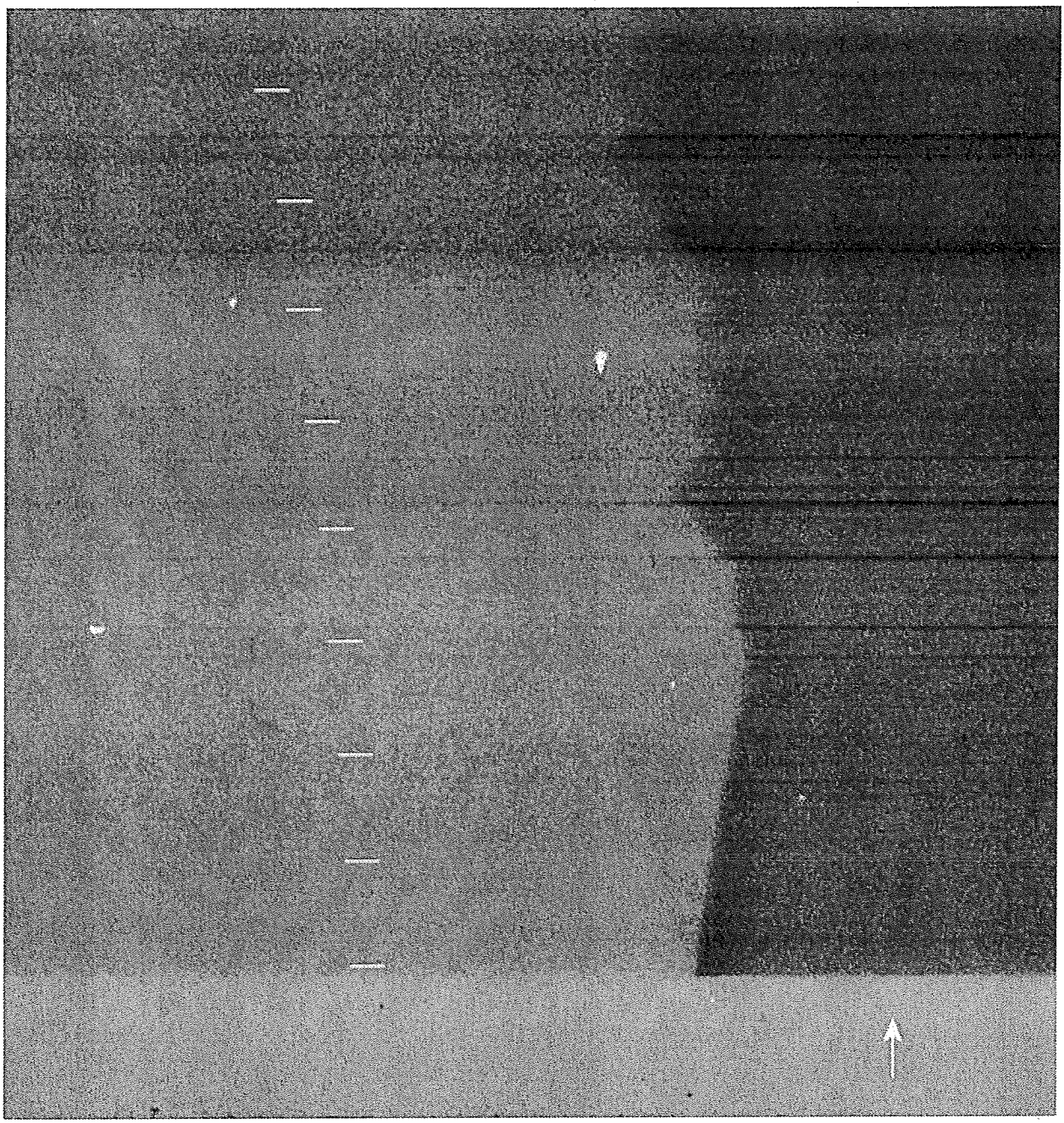

Figure 17

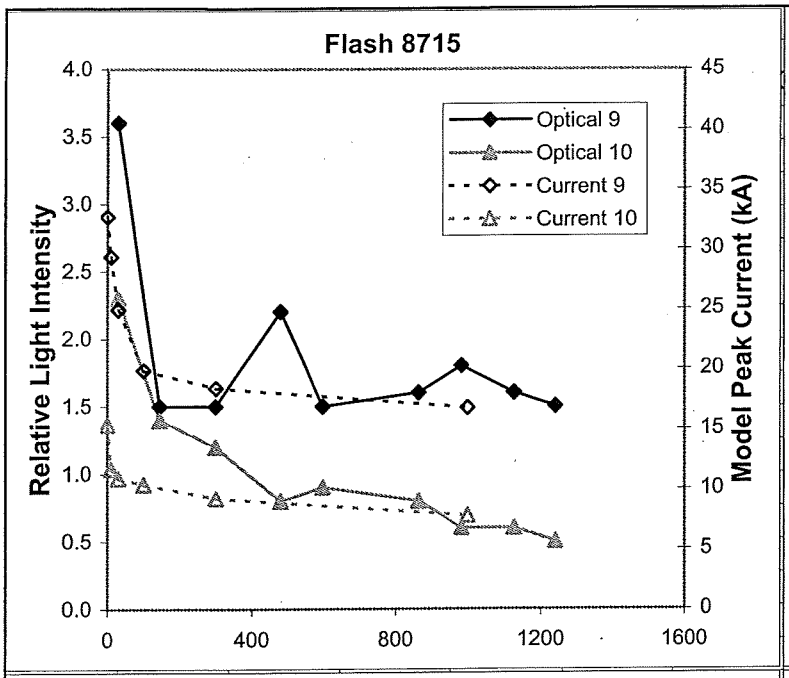
Flash 8715
Relative Light Intensity
Model Peak Current (kA)
Optical 9
Optical 10
Current 9
Current 10

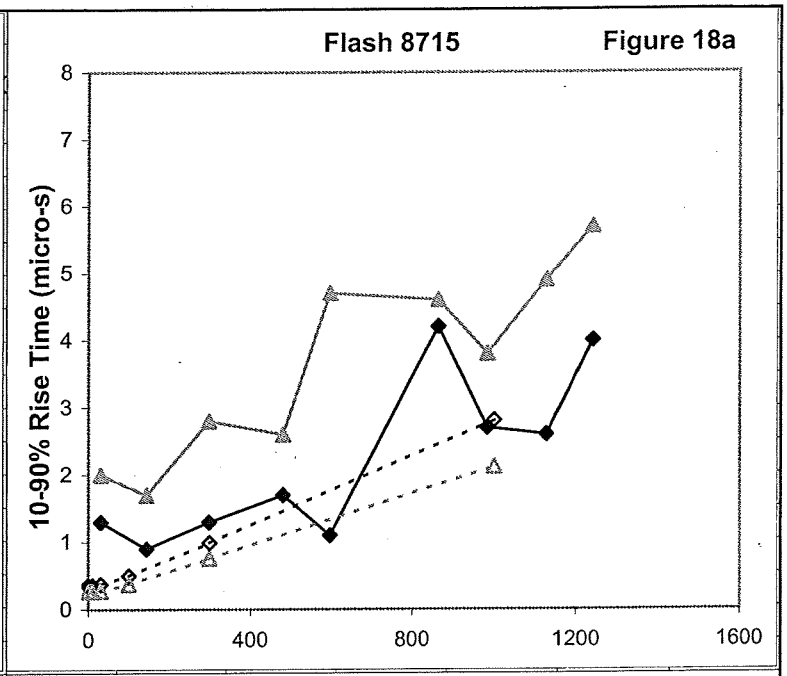
Flash 8715
Figure 18a
10-90% Rise Time (micro-s)

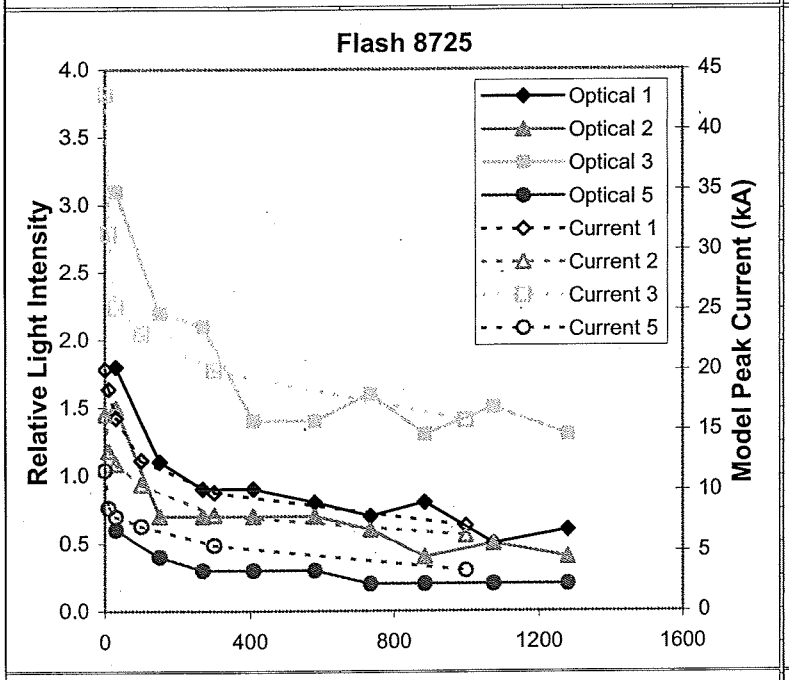
Flash 8725
Relative Light Intensity
Model Peak Current (kA)
Optical 1
Optical 2
Optical 3
Optical 5
Current 1
Current 2
Current 3
Current 5

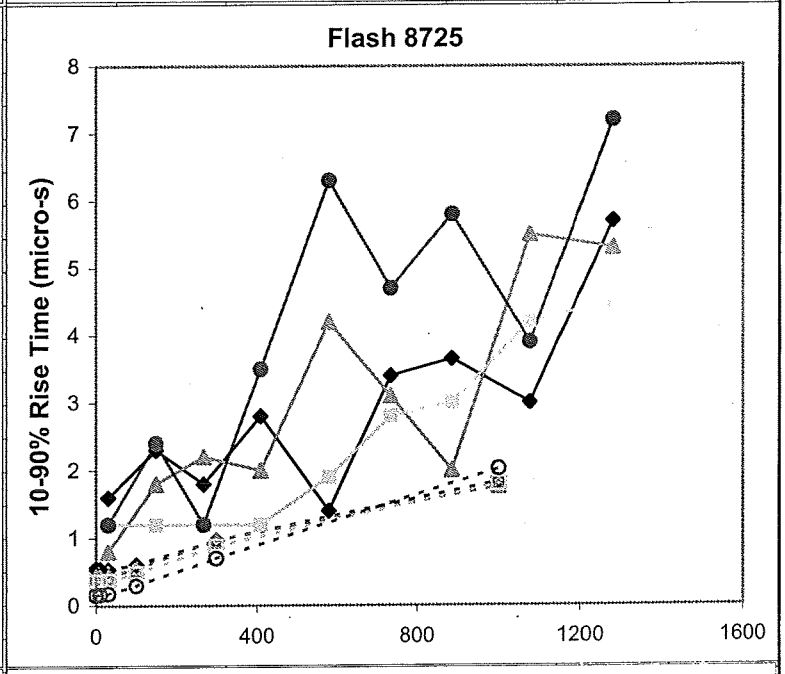
Flash 8725
10-90% Rise Time (micro-s)

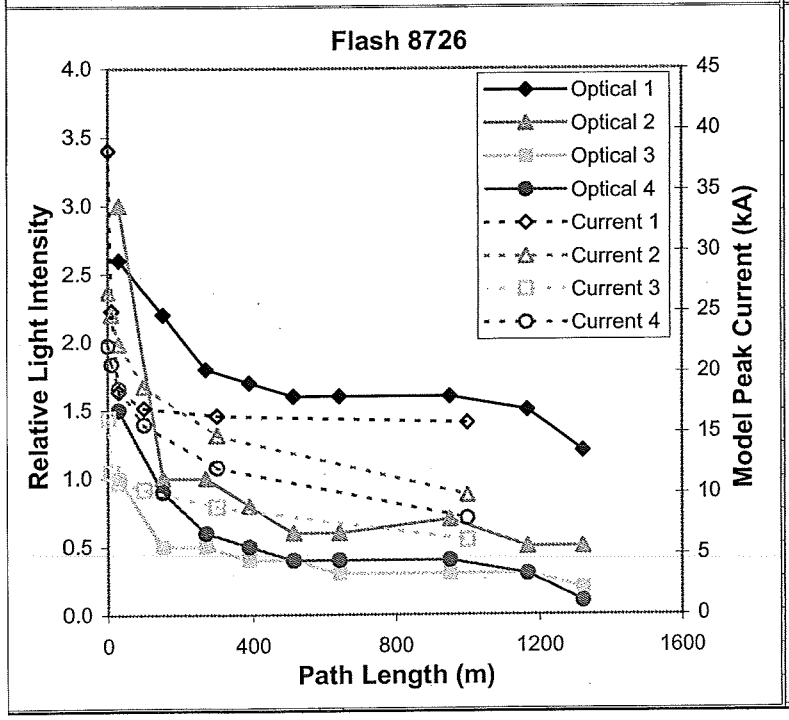
Flash 8726
Relative Light Intensity
Model Peak Current (kA)
Optical 1
Optical 2
Optical 3
Optical 4
Current 1
Current 2
Current 3
Current 4
Path Length (m)

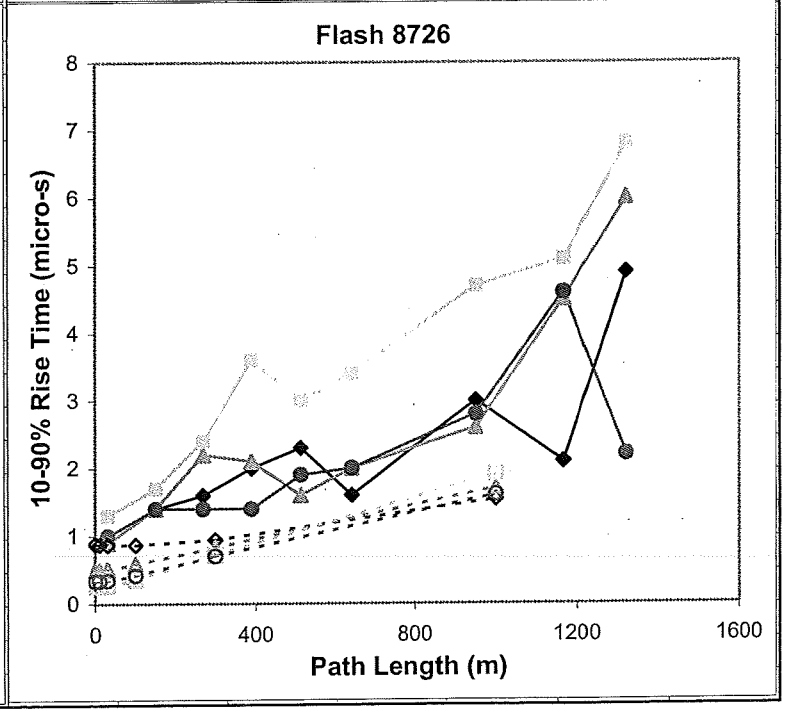
Flash 8726
10-90% Rise Time (micro-s)
Path Length (m)

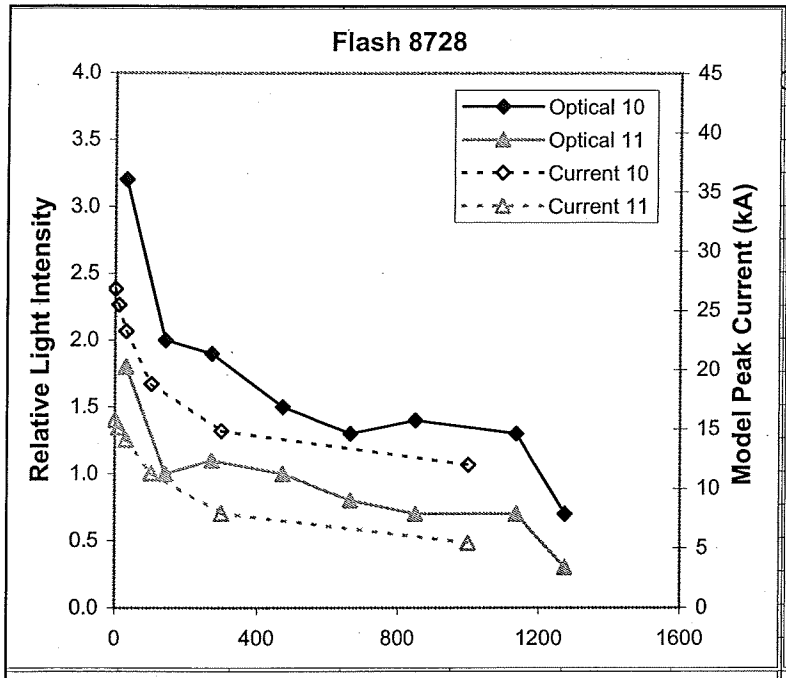
Flash 8728
Optical 10
Optical 11
Current 10
Current 11
Relative Light Intensity
Model Peak Current (kA)
4.0
3.5
3.0
2.5
2.0
1.5
1.0
0.5
0.0
45
40
35
30
25
20
15
10
5
0
0
400
800
1200
1600

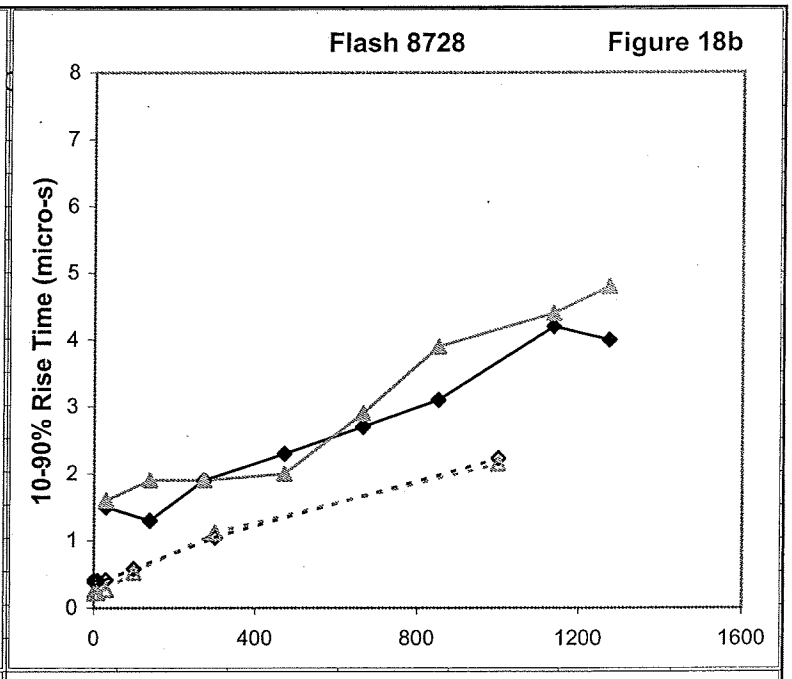
Flash 8728
Figure 18b
10-90% Rise Time (micro-s)
8
7
6
5
4
3
2
1
0
0
400
800
1200
1600

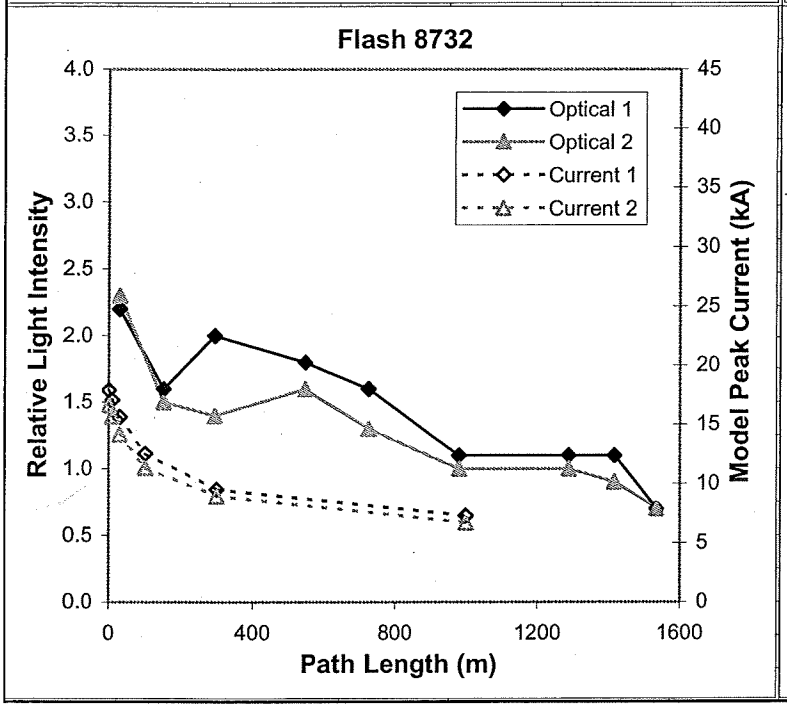
Flash 8732
Optical 1
Optical 2
Current 1
Current 2
Relative Light Intensity
Model Peak Current (kA)
4.0
3.5
3.0
2.5
2.0
1.5
1.0
0.5
0.0
45
40
35
30
25
20
15
10
5
0
0
400
800
1200
1600
Path Length (m)

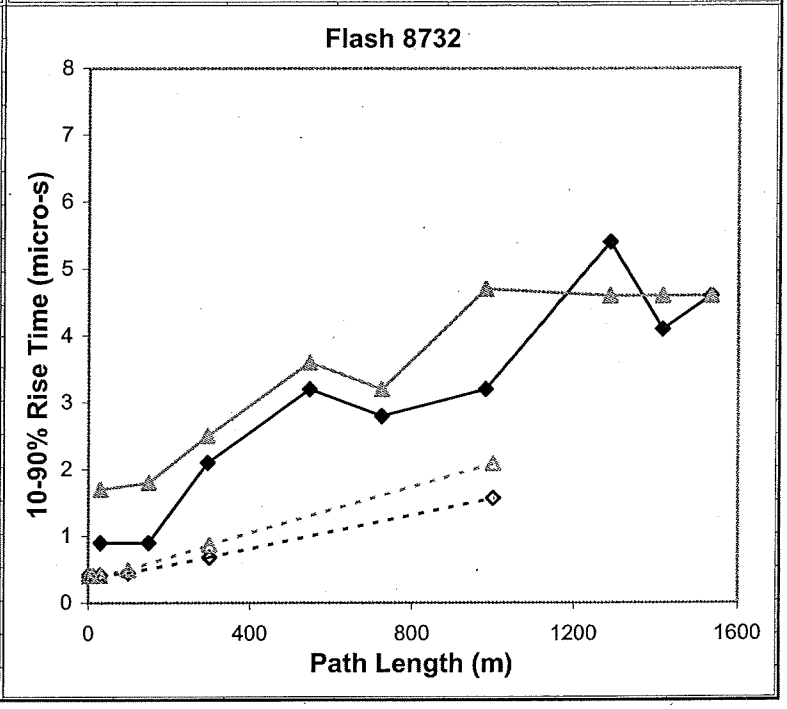
Flash 8732
10-90% Rise Time (micro-s)
8
7
6
5
4
3
2
1
0
0
400
800
1200
1600
Path Length (m)

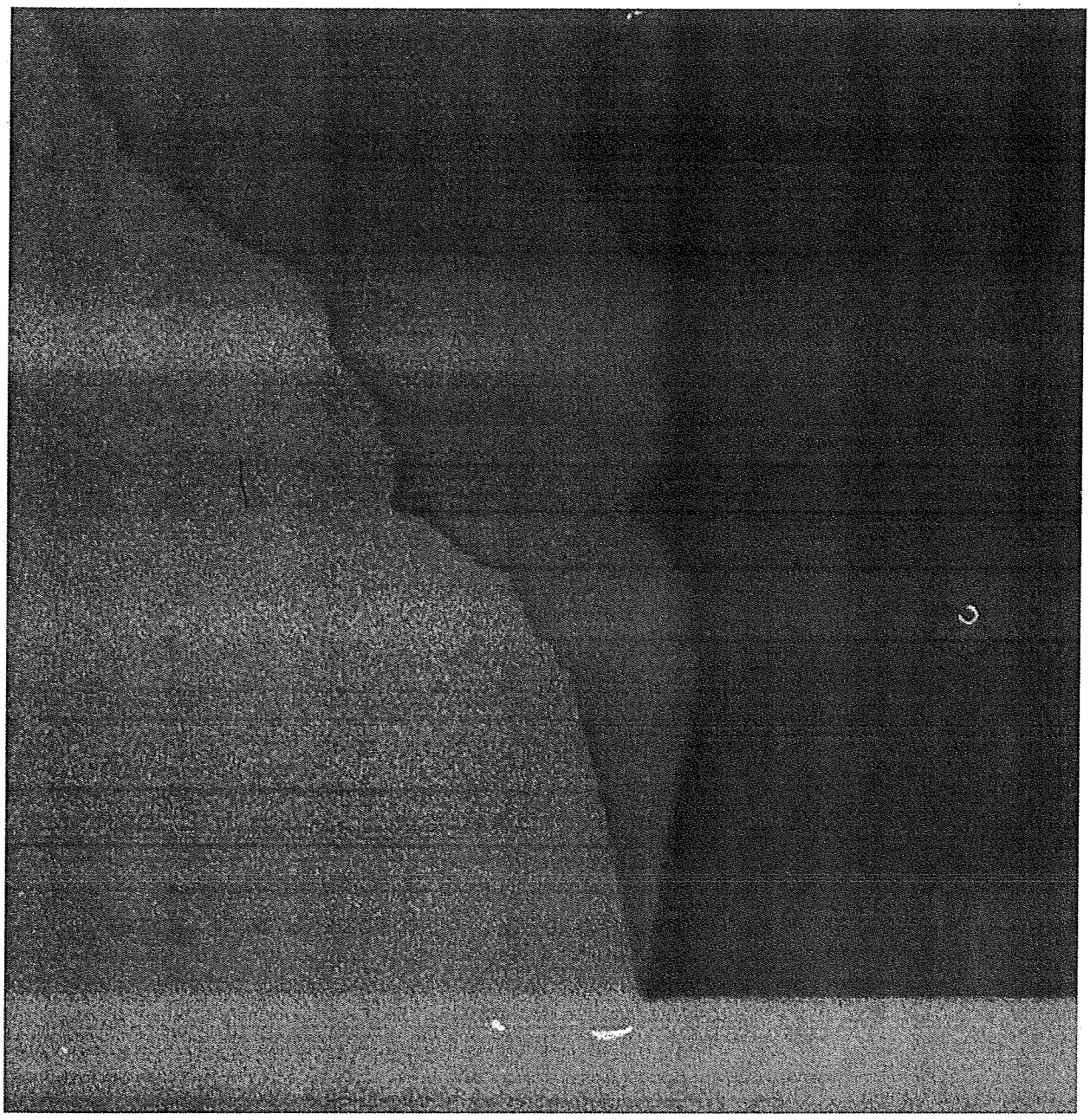

Figure 19

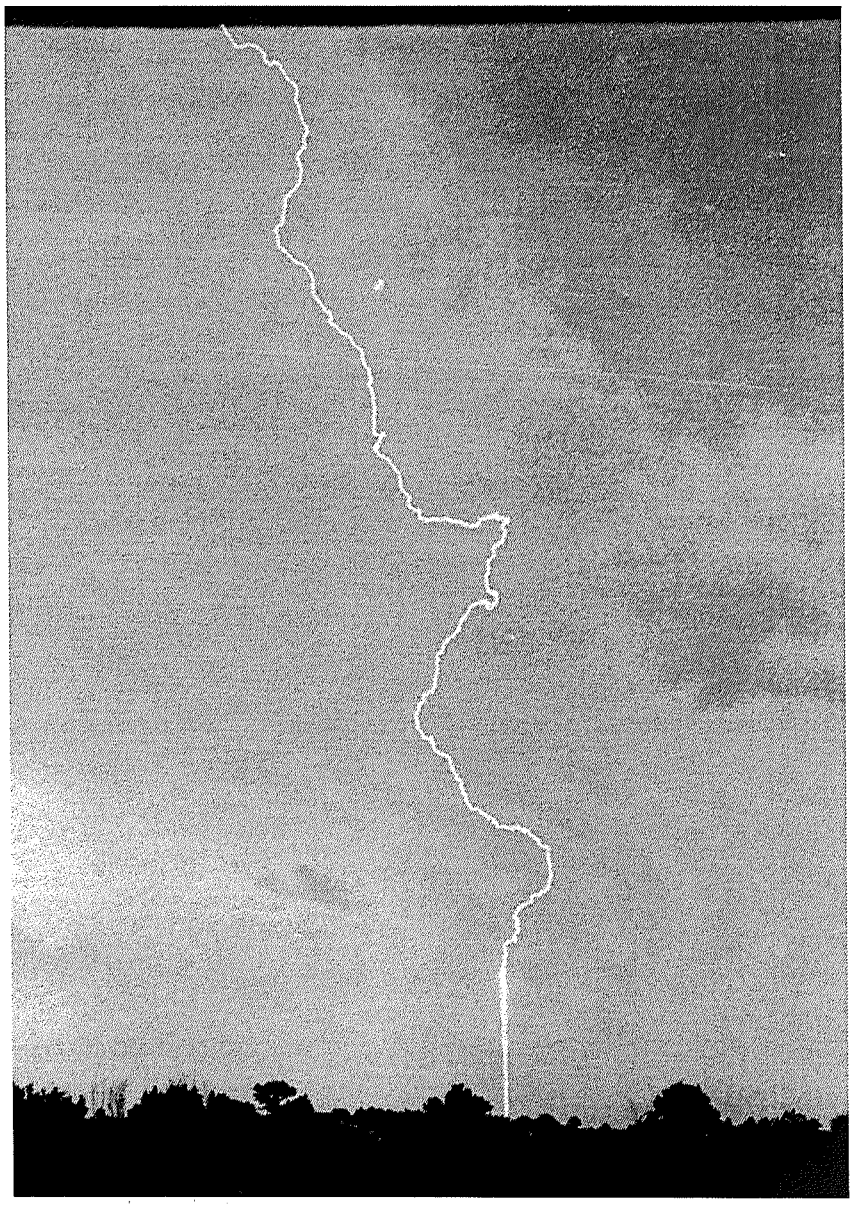

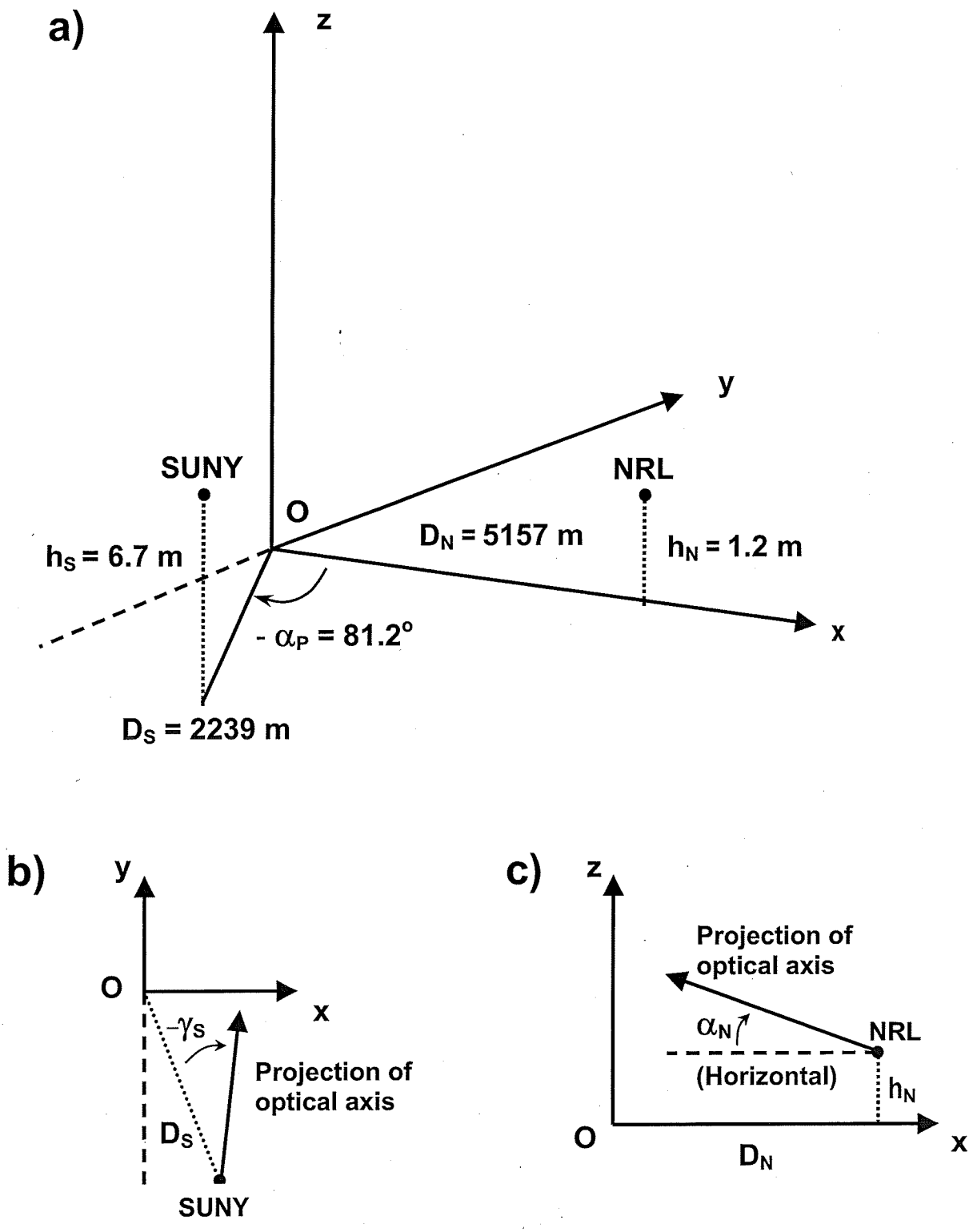
a)
z
y
SUNY
NRL
O
D_N = 5157 m
h_S = 6.7 m
h_N = 1.2 m
x
- α_P = 81.2°
D_S = 2239 m
b)
y
O
x
$-\gamma_S$
Projection of optical axis
D_S
SUNY
c)
z
Projection of optical axis
α_N
NRL
(Horizontal)
h_N
O
x
D_N

Figure A2

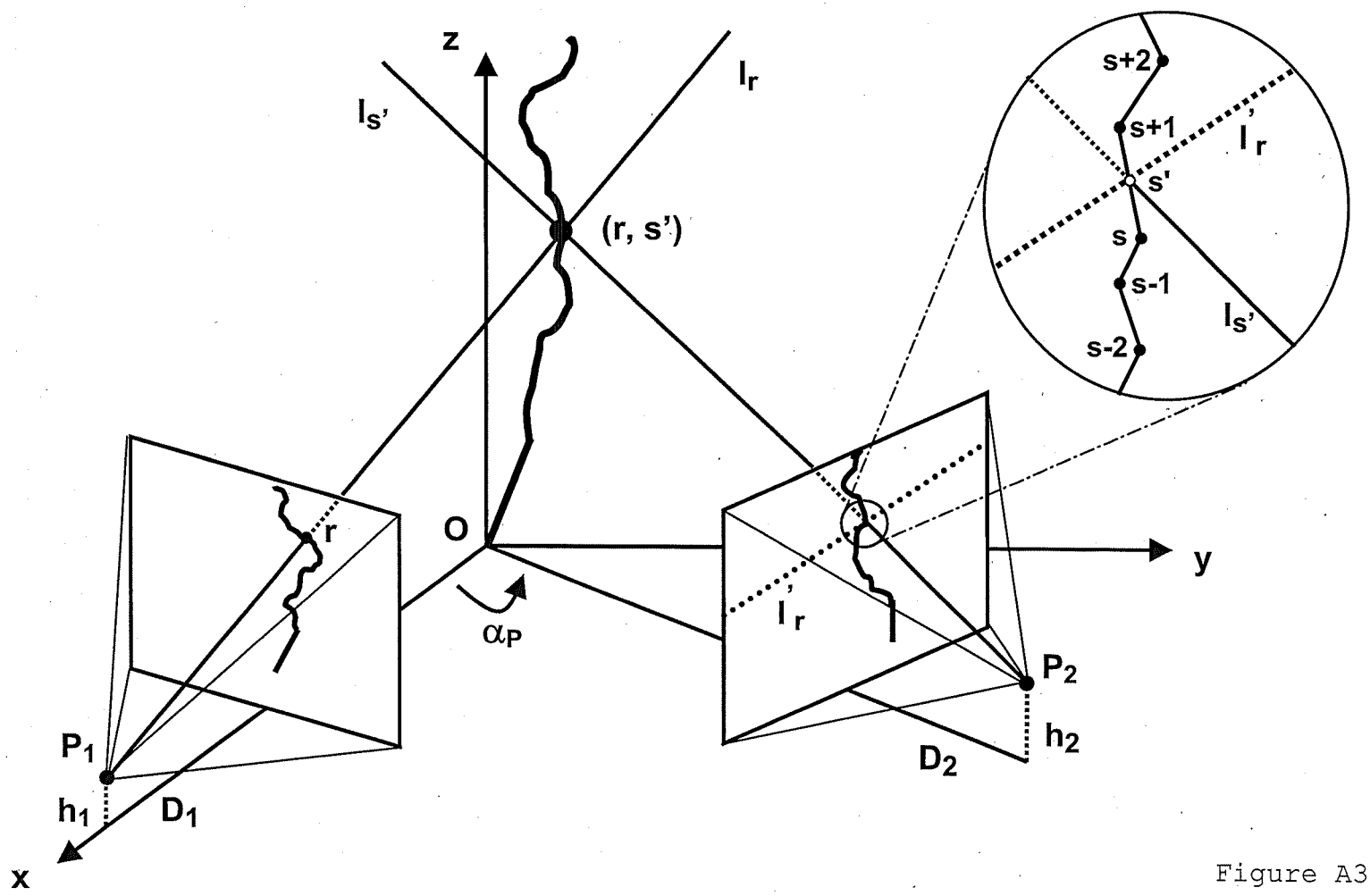

Figure A3

Figure A4a **8732 NRL Absolute Image Angles**

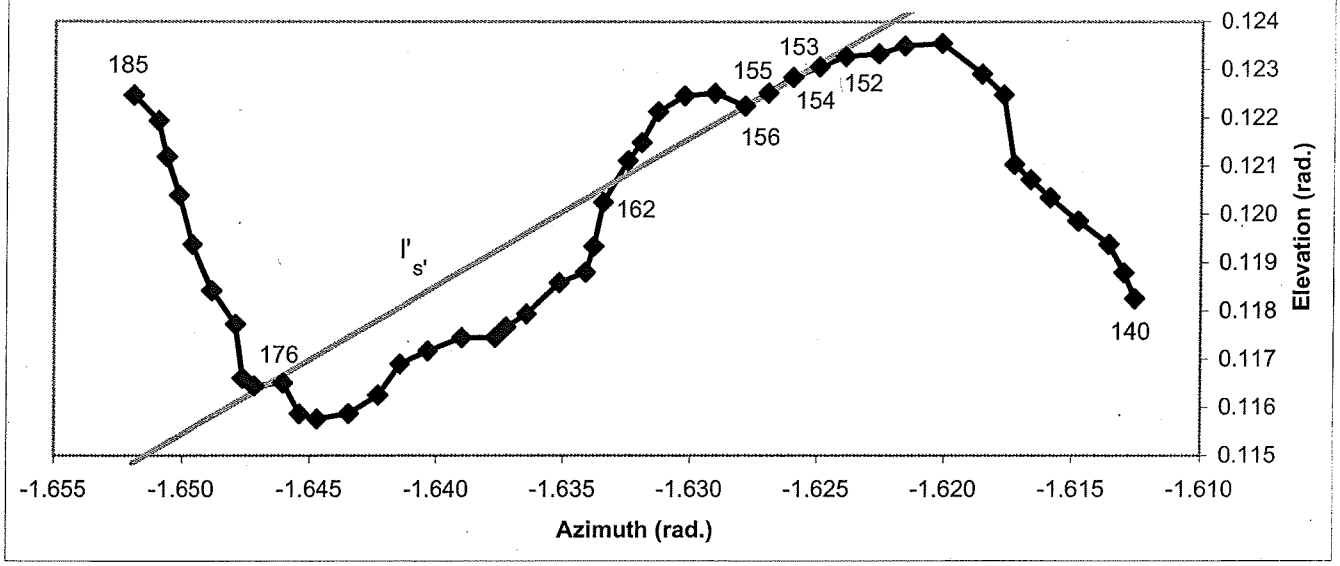

Figure A4b **8732 SUNY Absolute Image Angles**

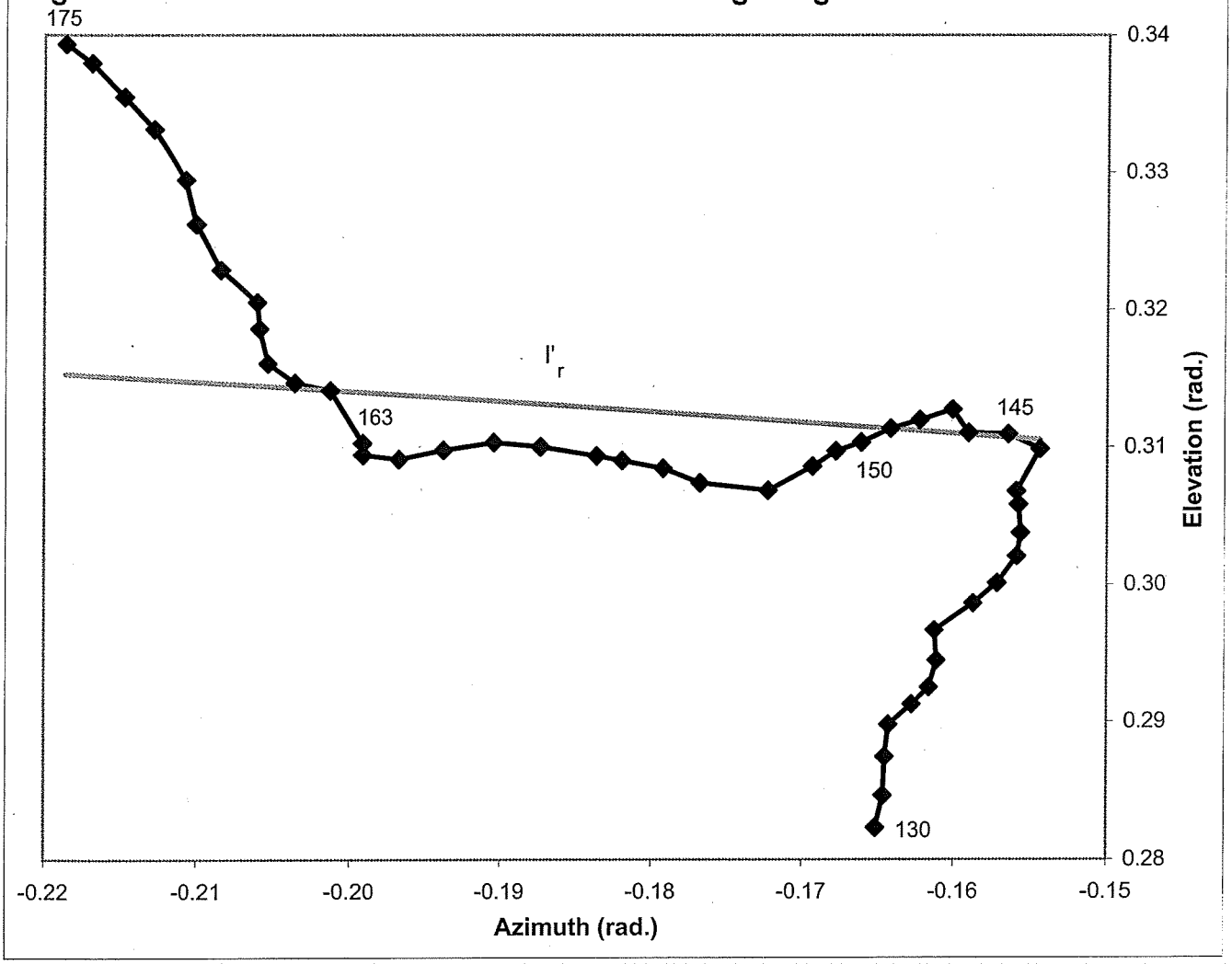

Figure A5a

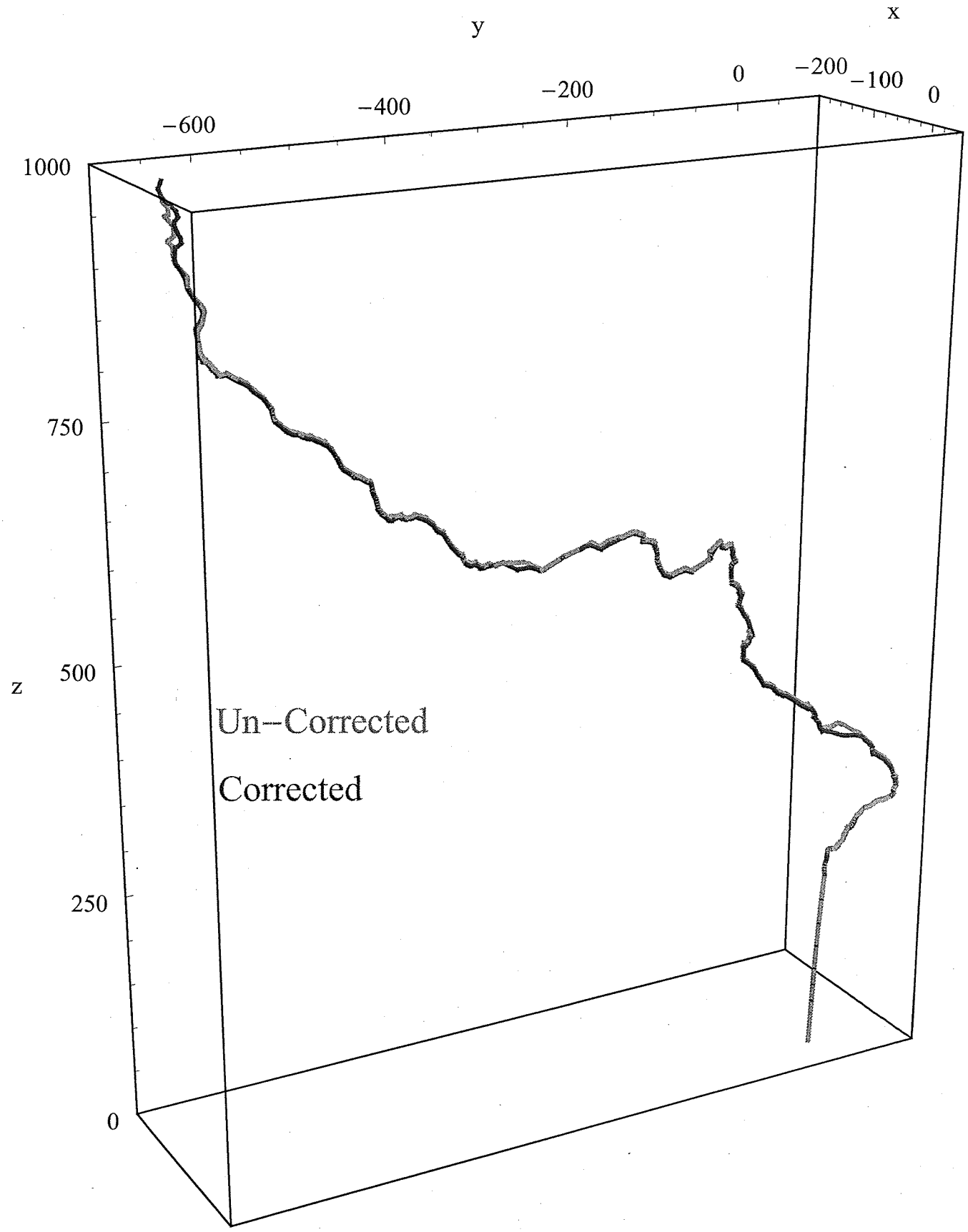
y
x
−600
−400
−200
0
−200
−100
0
1000
750
500
250
0
z
Un−Corrected
Corrected

Figure A5b

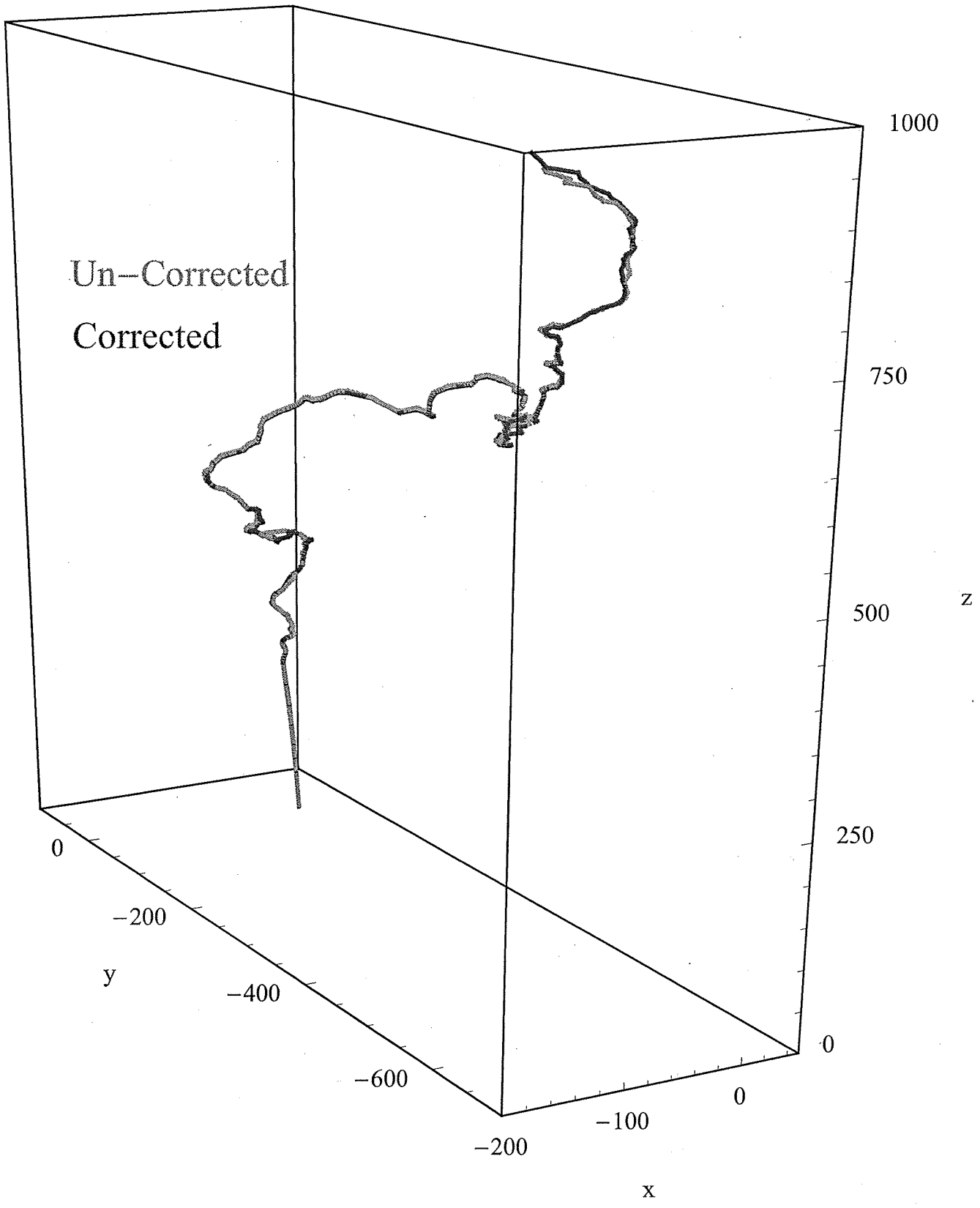
Un–Corrected
Corrected
1000
750
500
250
0
z
0
−200
−400
−600
y
−200
−100
0
x

Figure A6a

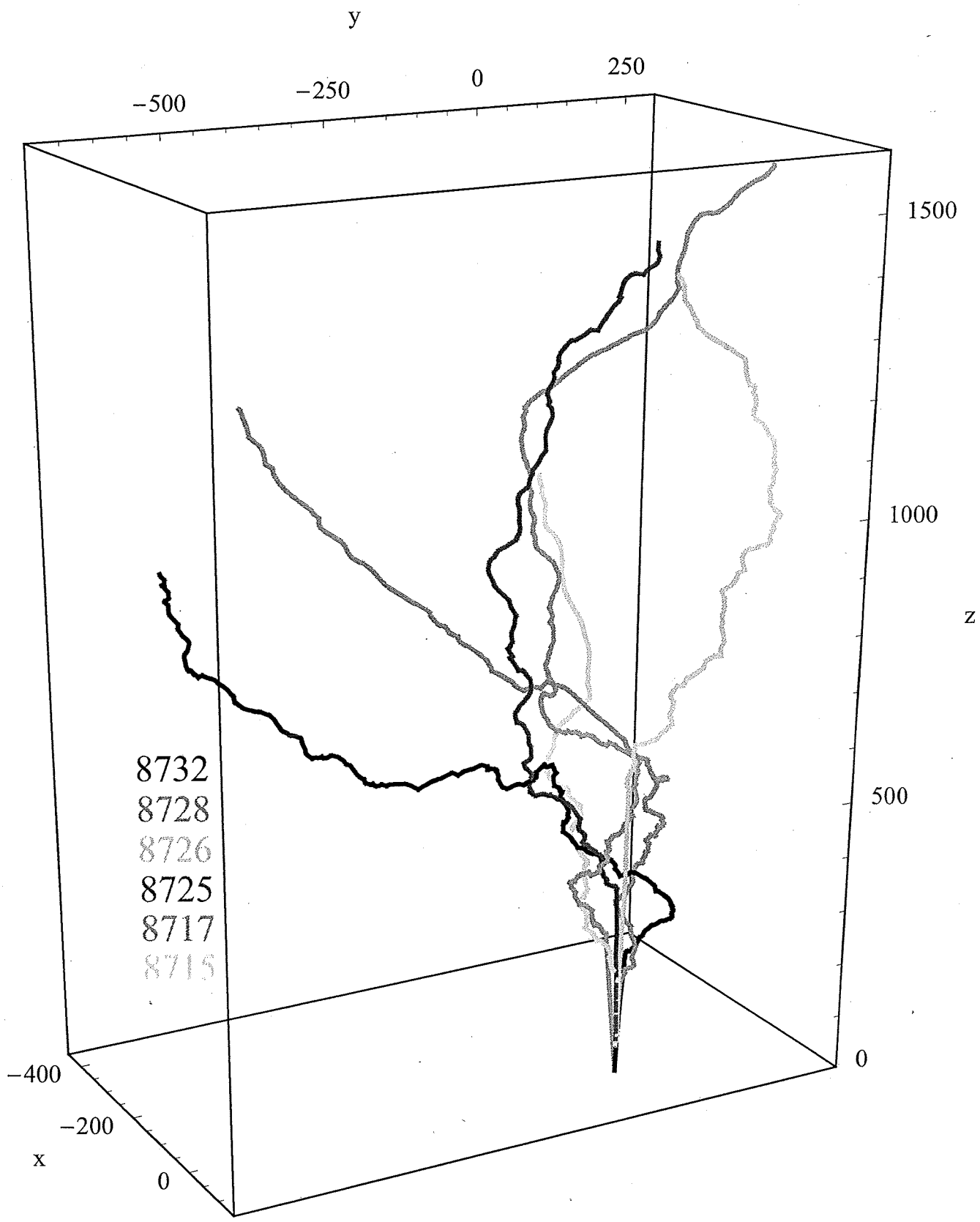
y
−500
−250
0
250
1500
1000
z
500
0
8732
8728
8726
8725
8717
8715
−400
−200
0
x

Figure A6b

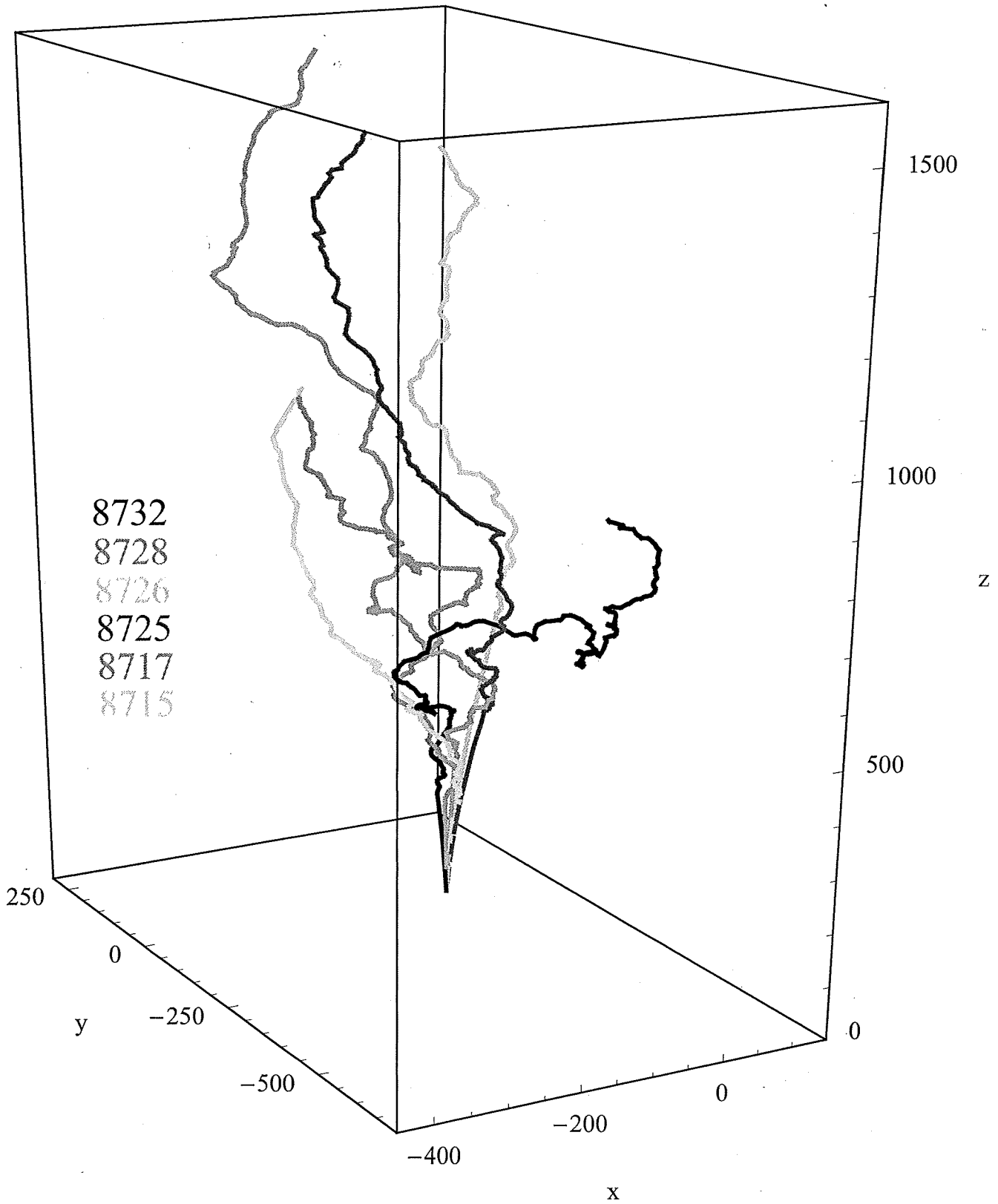
8732
8728
8726
8725
8717
8715
1500
1000
500
z
0
250
0
−250
−500
y
0
−200
−400
x

Figure A7

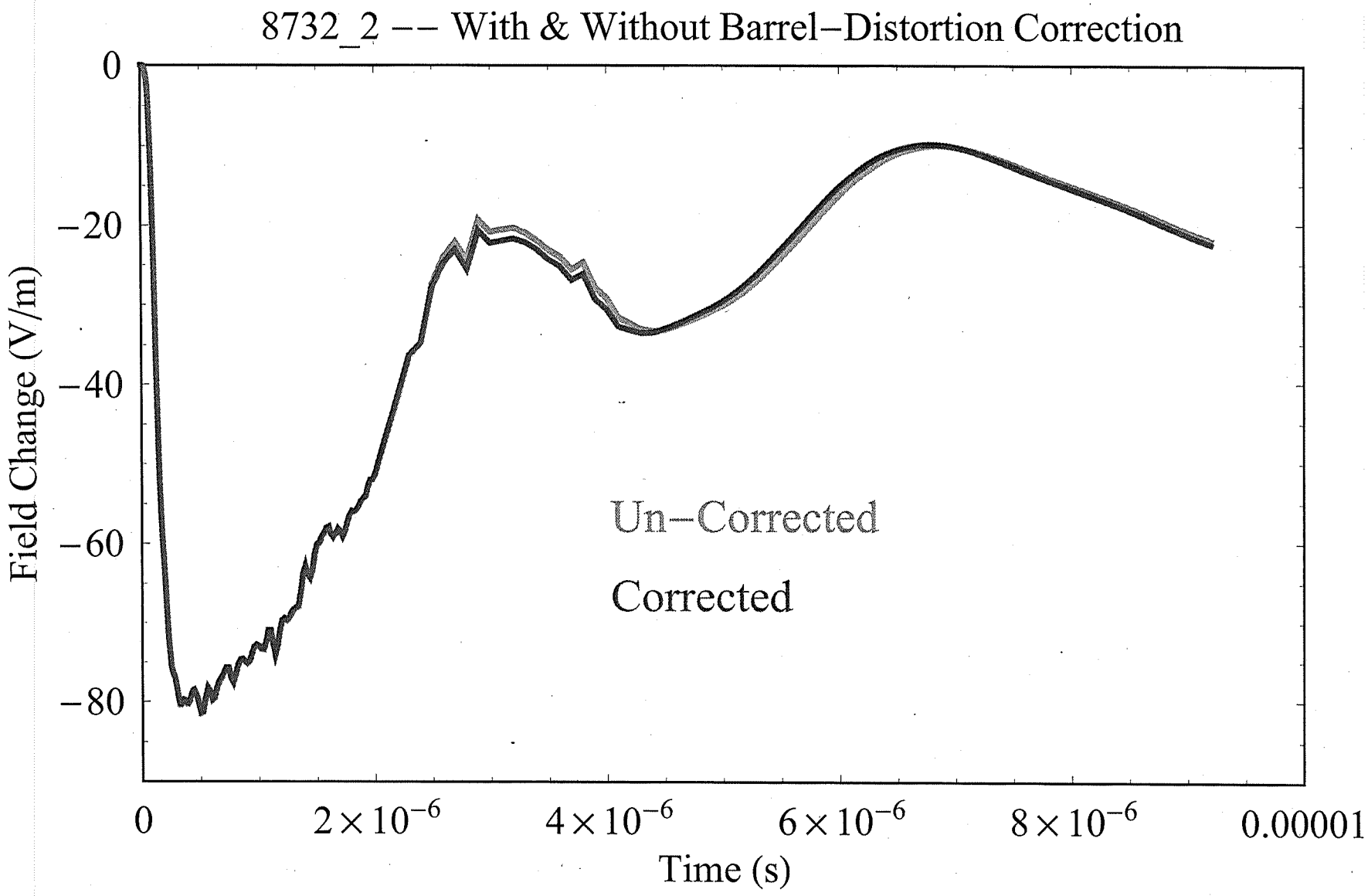
8732_2 -- With & Without Barrel-Distortion Correction
Field Change (V/m)
0
−20
−40
−60
−80
Un-Corrected
Corrected
0
2×10^−6
4×10^−6
6×10^−6
8×10^−6
0.00001
Time (s)

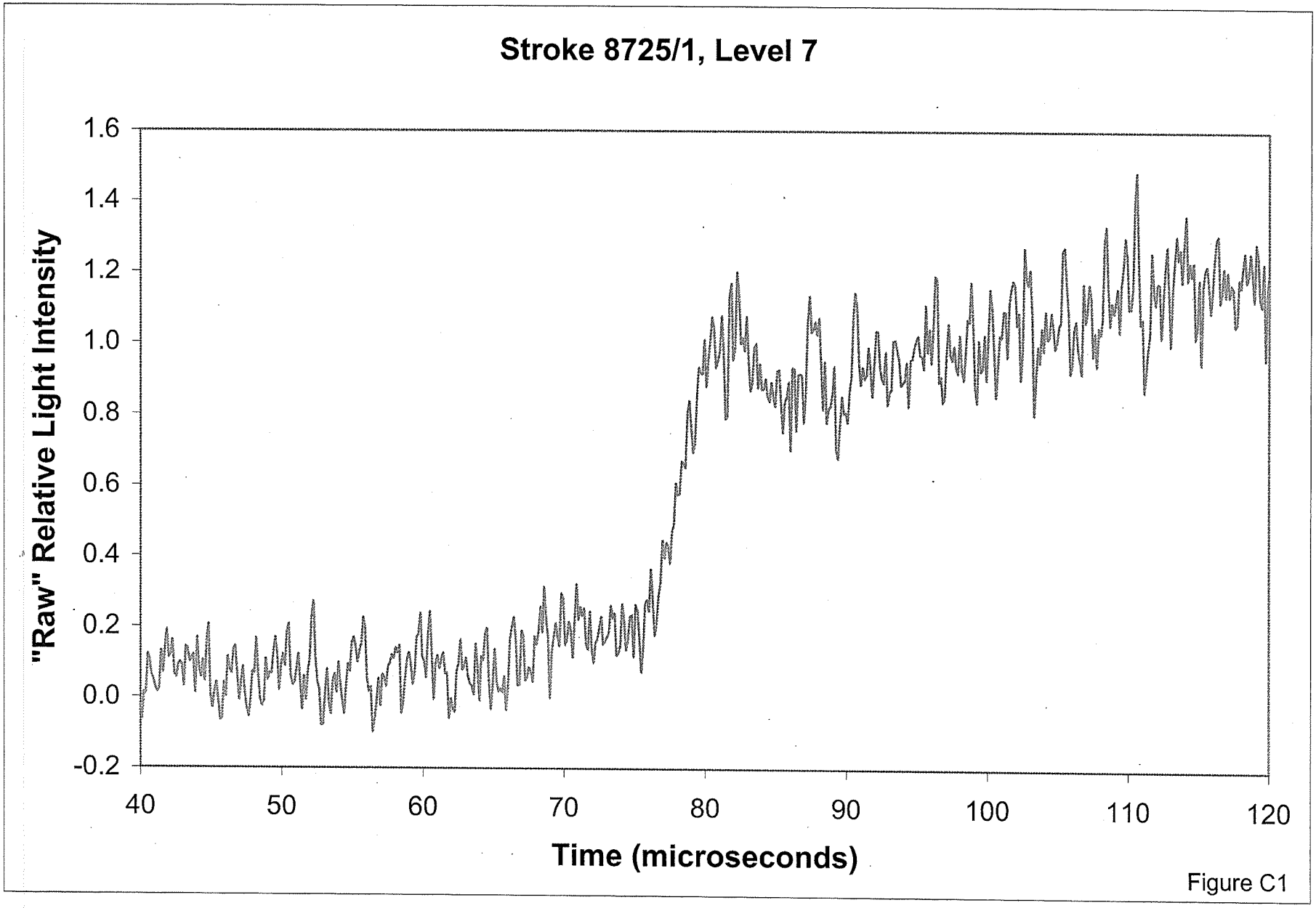
Stroke 8725/1, Level 7
"Raw" Relative Light Intensity
1.6
1.4
1.2
1.0
0.8
0.6
0.4
0.2
0.0
-0.2
40
50
60
70
80
90
100
110
120
Time (microseconds)

Figure C1

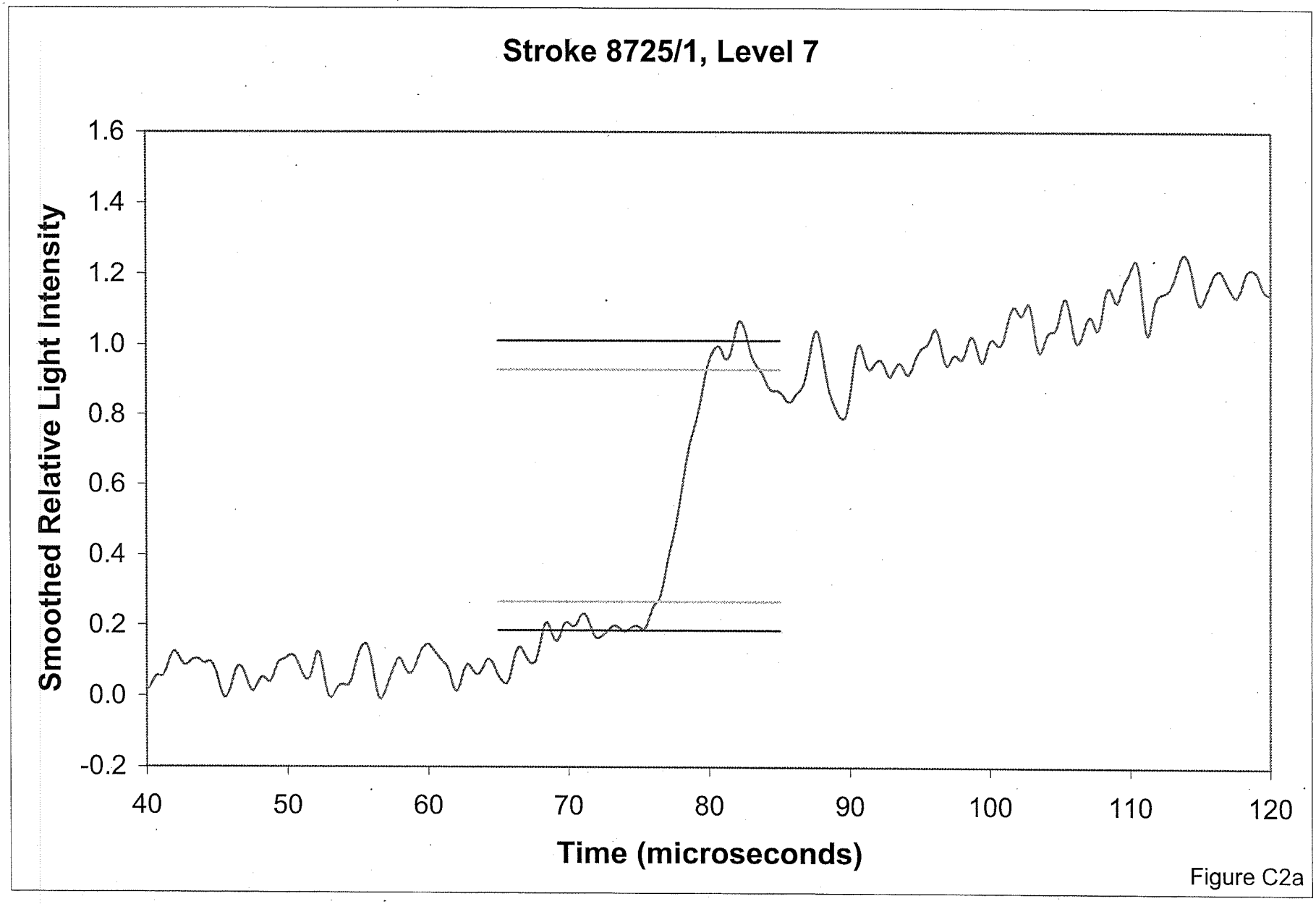
Stroke 8725/1, Level 7
Smoothed Relative Light Intensity
1.6
1.4
1.2
1.0
0.8
0.6
0.4
0.2
0.0
-0.2
40
50
60
70
80
90
100
110
120
Time (microseconds)

Figure C2a

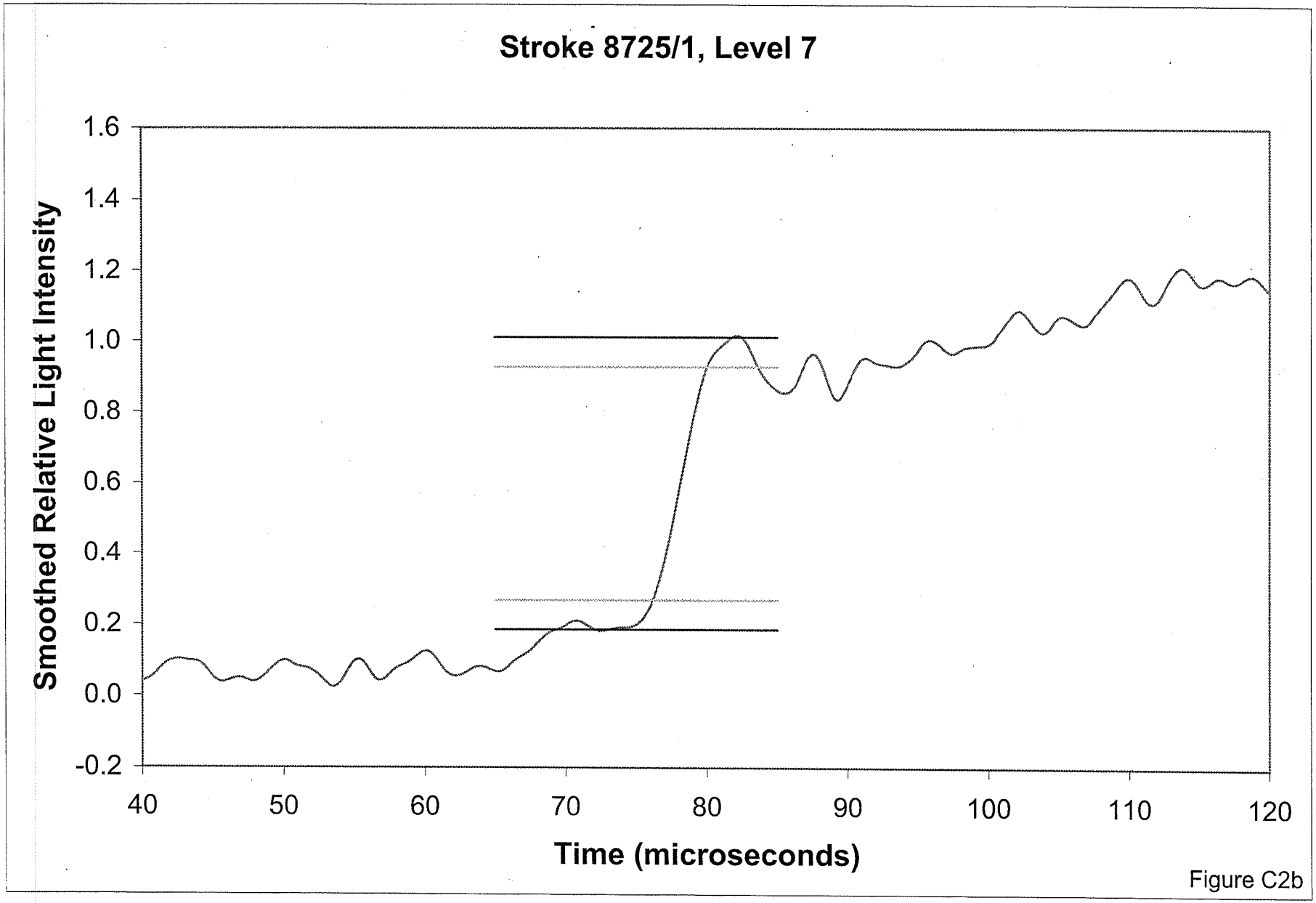
Stroke 8725/1, Level 7
Smoothed Relative Light Intensity
1.6
1.4
1.2
1.0
0.8
0.6
0.4
0.2
0.0
-0.2
40
50
60
70
80
90
100
110
120
Time (microseconds)

Figure C2b

LIGHTNING RETURN-STROKE CURRENT WAVEFORMS ALOFT, FROM MEASURED FIELD CHANGE, CURRENT, AND CHANNEL GEOMETRY

J.C. Willett, D.M. Le Vine and V.P. Idone

Return strokes (the bright channel associated with cloud-to-ground lightning) are the most powerful lightning processes. They are also responsible for most of the damage lightning does (to buildings, trees and aircraft) and for starting forest fires. Understanding the hazard associated with lightning requires information about the current in return strokes: The information available is largely limited to measurements at the base of the channel (where it touches the ground). Very little information is available about the current "aloft", which is important for understanding lightning process and for assessing the hazard to aircraft and space vehicles.

This paper describes remote sensing research that uses the electromagnetic fields radiated by return strokes to infer the magnitude and evolution of current as it propagates along the channel. It consists of two parts: (a) reconstruction of lightning channels from stereo photographs; and (b) using these channels to infer the behavior of the current above the ground from current waveforms measured at the channel base and the radiated electric field waveforms. Among the interesting results are the important role channel "tortuosity" plays in the shape of the radiated fields and an abrupt increase in rise-time and decrease in amplitude just above ground.

LIGHTNING RETURN-STROKE CURRENT WAVEFORMS ALOFT, FROM MEASURED FIELD CHANGE, CURRENT, AND CHANNEL GEOMETRY

J.C. Willett[1], D.M. Le Vine[2], and V.P. Idone[3]

[1]P.O. Box 41, Garrett Park, MD 20896
[2]Code 614.6, NASA/GSFC, Greenbelt, MD 20771
[3]ES-351, SUNY, 1400 Washington Ave., Albany, NY 12222

Abstract

Three-dimensional reconstructions of six rocket-triggered lightning channels are derived from stereo photographs. These reconstructed channels are used to infer the behavior of the current in return strokes above the ground from current waveforms measured at the channel base and electric-field-change waveforms measured at a range of 5.2 km for 24 return strokes in these channels. Streak photographs of 14 of the same strokes are analyzed to determine the rise times, propagation speeds, and amplitudes of relative light intensity for comparison with the electrical inferences. Results include the following: 1) The fine structure of the field-change waveforms that were radiated by subsequent return strokes can be explained, in large part, by channel geometry. 2) The average 10 - 90% rise time of the stroke current increased by about a factor of seven in our sample, from an observed 0.31 ± 0.17 μs at the surface to an inferred 2.2 ± 0.5 μs at 1 km path length above the surface. 3) The three-dimensional propagation speed of the current front averaged 1.80 ± 0.24 X 10^8 m/s over channel lengths typically greater than 1 km. 4) Assuming that the measured current was entirely due to the return stroke forced an unreasonably large and abrupt reduction in inferred current amplitude over the first few tens of meters above the surface, especially in cases when the leader was bright relative to its stroke. Therefore, a significant fraction of the current at the surface was probably due to the leader, at least in such cases. 5) Peak return-stroke currents decreased by approximately 37 ± 12% from 100 m to 1 km of path length above the surface. Because of uncertainty about how to partition the measured current between leader and return stroke, we are unable to infer the variation of current amplitude near the ground.